

Département de physique
Université de Fribourg (Suisse)



Inner-shell shake processes in light elements and 3s atomic-level widths of lanthanides

THESE

Présentée à la Faculté des Sciences de l'Université de Fribourg (Suisse)
pour l'obtention du grade de *Doctor rerum naturalium*

Olivier Mauron
d'Ependes (FR)

Thèse No 1399

Edition Mécanographie
2003

Acceptée par la Faculté des Sciences de l'Université de Fribourg (Suisse) sur proposition de :

Pof. Dr. P. Schurtenberger, Université de Fribourg, Président du Jury,

Prof. Dr. J.-Cl. Dousse, Université de Fribourg, Directeur de Thèse,

Prof. Dr. L. Schaller, Université de Fribourg, Rapporteur,

Prof. Dr. M. Pajek, University of Kielce (Poland), Rapporteur.

Fribourg, le 18 décembre 2002

Le directeur de thèse :



Prof. Dr. J.-Cl. Dousse

Le doyen :



Prof. Dr. D. Baeriswyl

Contents

| | |
|---|-----------|
| Résumé | 3 |
| Abstract | 7 |
| Part I: L-shell shake processes resulting from $1s$ photoionization in elements $11 \leq Z \leq 17$ | 13 |
| Part II: Double KL shell ionization in Al, Ca, and Co targets bombarded by low-energy electrons | 35 |
| Part III: Revisited L_3 and M_1 atomic-level widths of elements $54 \leq Z \leq 77$ | 61 |
| List of publications | 85 |
| Curriculum vitae | 89 |
| Remerciements | 91 |

Résumé

Ce travail de doctorat en physique atomique expérimentale contient trois parties distinctes ayant cependant comme point commun la spectroscopie X de haute résolution. Les mesures des trois projets ont été effectuées en effet au moyen d'un spectromètre à cristal incurvé de réflexion de type von Hamos. Les deux premiers sujets concernent l'étude des mécanismes conduisant à des états atomiques $K^{-1}L^{-1}$ doublement excités dans plusieurs éléments légers bombardés par des photons ou des électrons. Dans les deux projets, l'état doublement excité $K+L$ a été étudié en mesurant l'intensité relative des rayons X satellites $K\alpha L$ qui correspondent aux désexcitations radiatives $1s^1 2p^5 @ 1s^2 2p^4$ et $1s^1 2s^1 2p^6 @ 1s^2 2s^1 2p^5$. Dans la troisième partie qui se rattache au domaine de la métrologie des rayons X, des résultats précis et fiables concernant les énergies et largeurs naturelles des transitions L_3-M_1 et $L_3-M_{4,5}$ d'éléments mi-lourds et lourds ont été obtenus. Un nouvel ensemble de largeurs de la sous-couche atomique M_1 a pu être déduit de ces mesures.

Dans le premier projet l'étude a porté sur la double excitation KL de plusieurs éléments légers. La fluorescence des échantillons a été produite en irradiant les cibles avec le bremsstrahlung d'un tube de rayons X. Comme dans l'effet photoélectrique les photons incidents n'interagissent qu'avec un seul électron atomique, l'excitation multiple résultant d'une photoionisation $1s$ ne peut être expliquée qu'à partir d'un processus de la mécanique ondulatoire appelé «shake process». Si le changement du potentiel atomique faisant suite à la K est plus rapide que le temps de relaxation atomique, il peut y avoir en effet recouvrement partiel entre la fonction d'onde décrivant un électron lié dans le potentiel initial Ze et celle décrivant ce même électron dans une orbite plus extérieure ou dans le continu en présence du potentiel final $(Z+1)e$. A ce recouvrement des fonctions d'onde correspond une certaine probabilité pour l'électron d'être soit excité vers une orbitale plus extérieure incomplètement remplie (shakeoff).

Dans le premier projet la probabilité de «shake» pour la couche L faisant suite à une photoionisation $1s$ a été déterminée pour le Na, Mg, Al, Si, P, S et Cl. Les résultats obtenus ont été comparés à des prédictions (sudden approximation). Ce modèle s'applique à des excitations dites de .-à.-d. pour lesquelles le changement du potentiel atomique est beaucoup plus rapide que le temps de relaxation de l'atome. Il donne la probabilité de shake maximale. Au delà de cette valeur dite de saturation, la probabilité reste constante quelle que soit l'énergie des photons incidents. Dans nos mesures, l'énergie moyenne du bremsstrahlung utilisé pour irradier les échantillons était plus grande que l'énergie minimale à partir de laquelle le modèle SA est applicable. La comparaison de nos probabilités expérimentales avec les prédictions théoriques fournies par ce modèle était donc justifiée.

Bien qu'en principe les calculs du modèle SA ne s'appliquent qu'à des atomes libres et non pas à des atomes imbriqués dans un solide, un accord satisfaisant a été trouvé entre nos résultats expérimentaux et les prédictions théoriques, sauf pour l'élément le plus léger (Na). Pour des raisons de sécurité, les mesures concernant le chlore ont été effectuées en utilisant des cibles de NaCl et RbCl. Dans ce cas, il a été trouvé que

les résultats théoriques sous-estiment les valeurs expérimentales. Les écarts observés ont été expliqués par des effets chimiques et de corps solide. Il est bien connu en effet que les intensités des rayons X satellites dépendent de l'environnement chimique des atomes et qu'elles diminuent quasi-linéairement avec l'électronégativité de l'élément impliqué dans le composé. La probabilité de shake du sodium a été déterminée à partir des mesures effectuées avec la cible de Na pur et celle du composé entre les deux valeurs mais toutes deux étaient plus grandes, de façon significative, au résultat fourni par les calculs du modèle SA. Là aussi, la différence a été attribuée à l'influence de la matrice cristalline sur les atomes de sodium.

Le deuxième projet de cette thèse concerne l'ionisation double d'atomes neutres bombardés par des électrons. Dans ce cas, la double excitation résulte de plusieurs processus comme celui de shake déjà (wo-step-one) ou TS2 (two-step-two). Dans un δ émis par la première collision électron-électron percute un deuxième électron lié qui est à son tour éjecté, conduisant ainsi à la création d'une double lacune dans l'atome cible. Dans un processus TS2, la seconde lacune est produite par le même électron que la première. Dans ce cas l'électron incident interagit séquentiellement avec deux électrons liés appartenant au même atome-cible.

Dans cette étude, des échantillons d'aluminium, de calcium et de cobalt ont été bombardés au moyen de photons (tube de rayons X) et d'électrons de basse énergie. Pour chaque cible, l'énergie des électrons incidents a été variée entre l'énergie de seuil correspondant à l'ionisation double KL et l'énergie maximale du canon à électrons utilisé (20 keV). Les sections efficaces d'ionisation double S_{KL} ont été déduites des intensités relatives $I_{KL^{(1)}} : I_{KL^{(0)}}$ des raies X satellites et des sections efficaces d'ionisation S_K reportées dans la littérature. Comme en première approximation les processus de shake et TS1 ne dépendent pas du mécanisme ayant produit la première lacune profonde, il est légitime de supposer que les probabilités de shake et les sections efficaces du processus TS1 sont les mêmes dans les cas de la photoionisation et du bombardement électronique. Cette hypothèse de travail nous a permis d'évaluer l'importance du mécanisme TS2 dans la KL .

Le mécanisme TS1 qui est le plus important juste au-dessus du seuil d'excitation double diminue rapidement avec l'énergie. Le processus de shake se comporte exactement de façon inverse. Il croît avec l'énergie d'excitation jusqu'à sa valeur de saturation. A saturation, le changement de potentiel atomique est suffisamment rapide pour pouvoir appliquer le modèle SA au calcul des probabilités de shake. Les mesures de photoionisation ayant été effectuées avec un tube de rayons X ayant une réponse spectrale continue, la variation du processus combiné shake+TS1 en fonction de l'énergie des photons n'a pas pu cependant être mesurée directement. Cette variation a donc été calculée au moyen des modèles de Roy et de Thomas, en exigeant toutefois que les courbes théoriques passent par le point expérimental obtenu à partir des mesures avec le tube de rayons X. Pour chaque énergie d'excitation, la section efficace S_{TS2} a ensuite été déterminée en soustrayant la moyenne des probabilités de shake données par le modèle de Roy et celui de Thomas de la S_{KL} . Dans cette méthode, nous avons admis que l'amplitude des termes d'interférence entre les trois processus (shake, TS1 et TS2) était négligeable. Nous avons trouvé que la

contribution maximale du processus TS2 à l'ionisation KL s'élevait à 40% pour l'aluminium, 25% pour le calcium et 15% pour le cobalt. De plus, une variation en Z^{-1} a été observée pour cette contribution TS2.

L'objectif principal du troisième projet concernait la détermination de la largeur naturelle de l'état $3s$ (sous-couche M_1) des éléments compris entre le xénon ($Z=54$) et l'iridium ($Z=77$). Les largeurs de niveaux atomiques et celles des transitions radiatives présentent un intérêt aussi bien en physique théorique qu'en physique expérimentale. Pour le théoricien, ces largeurs représentent un outil précieux pour vérifier la qualité independent particle model) et MBT (many body theory).

Elles présentent en particulier un intérêt fort utile pour contrôler la qualité des prédictions théoriques concernant les durées de vie totales des lacunes, les probabilités de transitions radiatives, Auger et Coster-Kronig, ou encore les rapports de fluorescence. Pour l'expérimentateur, une bonne connaissance des largeurs des transitions radiatives est aussi nécessaire dans certaines méthodes d'analyse chimique comme les méthodes XRF (x-ray fluorescence) et PIXE (proton-induced x-ray emission). De façon similaire, dans un grand nombre d'expériences dans lesquelles des structures discrètes ou continues de faible intensité (transitions RAE par exemple) doivent être extraites des queues de transitions diagrammes voisines intenses, la forme spectrale de ces dernières doit être connue avec précision pour obtenir des résultats fiables. Enfin, en spectroscopie X de haute-résolution, une connaissance précise des largeurs des transitions permet d'améliorer l'analyse des données en diminuant le nombre de paramètres libres puisque les largeurs naturelles des transitions peuvent être fixées à des valeurs connues. Ceci est particulièrement important pour l'analyse de spectres complexes comprenant des rayons X satellites car ces derniers ne sont le plus souvent que faiblement séparés des lignes diagrammes parentes.

Il existe dans la littérature plusieurs articles présentant les largeurs des niveaux atomiques. La plupart de ces études présentent des résultats théoriques et seulement quelques unes d'entre elles sont basées sur des données expérimentales. Récemment, dans un article de synthèse, Campbell et nombre de données expérimentales dont ils ont déduit un ensemble auto-consistant de largeurs atomiques pour les couches K à N_7 de tous les éléments du tableau périodique. Pour la sous-couche M_1 des éléments $55 \leq Z \leq 77$, Campbell et Papp ont cependant relevé qu'il y avait une absence marquée de données expérimentales qu'il serait judicieux de combler en mesurant par exemple les transitions radiatives L_3-M_1 . Nous avons donc entrepris de déterminer la largeur naturelle de l'état atomique $3s$ de nombreux éléments mi-lourds et lourds ($_{54}\text{Xe}$, $_{56}\text{Ba}$, $_{57}\text{La}$, $_{59}\text{Pr}$, $_{60}\text{Nd}$, $_{63}\text{Sm}$, $_{64}\text{Gd}$, $_{65}\text{Tb}$, $_{66}\text{Dy}$, $_{67}\text{Ho}$, $_{70}\text{Yb}$, $_{74}\text{W}$ and $_{77}\text{Ir}$). Comme les largeurs des transitions radiatives sont données par la somme des largeurs des deux états atomiques participant à cette $d_{5/2}$ (sous-couche M_5) sont connues avec une précision de l'ordre de 0.1 eV, les largeurs L_3 ont tout d'abord été déterminées à partir des largeurs mesurées des transitions L_3-M_5 . Soustrayant ces largeurs L_3 de celles obtenues en mesurant les transitions L_3-M_1 , nous avons pu déterminer les largeurs M_1 avec une précision d'environ 5%.

A cause des transitions Coster-Kronig L_1L_3N et L_2L_3N , les raies L_3 sont en général élargies par des satellites N non résolus, ce qui complique l'analyse et rend les résultats obtenus peu fiables. Cette difficulté a pu être contournée en irradiant les échantillons avec des faisceaux monochromatiques de lumière synchrotrique

dont l'énergie, pour chaque cible, était plus grande que celle correspondant au bord d'absorption L_3 mais plus petite que celles correspondant aux bords L_2 et L_1 . Les mesures ont été réalisées auprès de la source de rayonnement synchrotronique européenne (ESRF) de Grenoble.

En dehors de la région des lanthanides, des différences d'environ -2 eV ont été observées entre nos résultats et les valeurs recommandées par Campbell et Papp. Dans la région des lanthanides, une tendance opposée a été observée, nos résultats étant plus grands que ceux de Campbell et Papp. De surcroît dans cette région nous avons trouvé que les largeurs M_1 augmentaient avec le spin total de l'orbitale $4f$. Des différences allant jusqu'à 3 eV par rapport aux valeurs obtenues en interpolant les largeurs trouvées à l'extérieur des terres-rares ont été observées. Ces écarts ont pu être expliqués qualitativement au moyen d'un modèle faisant intervenir le couplage de l'électron célibataire $3s$ dans l'état excité initial avec le spin total de l'orbitale incomplète $4f$.

De ce troisième projet, des résultats fiables concernant les largeurs de la sous-couche L_3 et les énergies des transitions $L_3-M_{4,5}$ et L_3-M_1 ont également été obtenues pour les treize éléments étudiés. Alors qu'un bon accord a été trouvé avec les valeurs de Campbell et Papp pour ce qui est des largeurs L_3 , des écarts parfois importants ont été observés pour les énergies des transitions $L_3-M_{4,5}$ et surtout L_3-M_1 par rapport aux données expérimentales existantes.

Abstract

Three different parts related to experimental Atomic Physics are contained in the present Ph. D. thesis. In the three projects the measurements were performed by means of high-resolution x-ray spectroscopy, using a reflecting von Hamos-type bent crystal spectrometer. This experimental technique represents thus the common denominator of the three projects. The two first parts of the thesis are devoted to the study of the mechanisms leading to the double $K+L$ excitation of light element atoms as a result of photon or electron bombardment. In both projects the probabilities for producing double $K^{-1}L^{-1}$ vacancy states were determined by measuring the relative yields of the $K\alpha L$ x-ray satellite lines associated to the $1s^1 2p^5 @ 1s^2 2p^4$ and $1s^1 2s^1 2p^6 @ 1s^2 2s^1 2p^5$ radiative decay channels. In the third part which is related to the field of x-ray transition metrology precise and reliable data concerning the energies and line widths of the L_3-M_1 and $L_3-M_{4,5}$ transitions of mid-heavy and heavy elements were obtained. From the observed transition widths, a new set of M_1 atomic-level widths could be determined.

The first project is a study of the double KL photoexcitation of several low- Z elements. The target fluorescence x-ray emission was produced by irradiating the samples with the bremsstrahlung from an x-ray tube. As in photoionization a single photon is assumed to interact with a single bound electron, double KL photoexcitation can only be produced via so-called shake processes. Actually, if the change in the atomic potential following the creation of the $1s$ vacancy is faster than the atomic relaxation, a second core-electron can be promoted into an unfilled upper level (shakeup) or ionized in the continuum (shakeoff) as a result of the overlap of the wave functions of the shaken electron in the initial and final states.

In this project the probability for observing L -shell shake processes as a result of $1s$ photoionization was determined for Na, Mg, Al, Si, P, S and Cl. Obtained results were compared to theoretical predictions based on the sudden approximation (SA) model. The sudden approximation picture is valid at high excitation energies where the change in the atomic potential is fast enough and leads to a saturation of the shake probability. The average energies of the bremsstrahlung used for the irradiation of the samples lay far above the break point of the sudden approximation. Thus, a comparison of our experimental results with sudden approximation predictions was meaningful.

Although SA calculations are based on the free atom model and are therefore not fully adequate for solid targets, except for the lightest element (Na) a quite satisfactory agreement was found between our results concerning pure elements and the SA predictions. For safety reasons, chlorine measurements were performed using NaCl and RbCl compound targets. In this case the SA predictions were found to somewhat underestimate the experimental values. The observed deviations were explained by solid state and chemical effects. Satellite intensities are indeed sensitive to the chemical environment of the atoms and decrease almost linearly with the electronegativity of the element involved in the compound. The experimental shake probability of sodium was determined from the measurements performed with the pure Na and compound NaCl targets. The two shake

probabilities were found to be consistent within the combined errors, both results being, however, significantly underestimated by theory. Here again the discrepancy was explained by solid state and chemical effects which are indeed expected to be more pronounced for lighter elements.

The second project concerns the double ionization of neutral atoms by electron bombardment. In this case the double excitation may result from several processes, namely the shake process and the so-called two-step-one (TS1) and two-step-two (TS2) mechanisms. In the TS1 process the δ -electron ejected as a result of the first interaction collides with another bound electron which in turn is kicked out so that a double vacancy state is created in the target atom. In the TS2 process the second vacancy is produced by the same electron as the first one. In this case the incoming electron is thus assumed to interact sequentially with two electrons pertaining to the same target atom.

Al, Ca and Co targets were bombarded with photons from an x-ray tube and low-energy electrons. For each target, the energy of the electron-beam was varied between the double KL excitation energy threshold and the maximum energy at which the electron-gun could be operated (20 keV). The cross sections S_{KL} for double KL shell ionization were derived from the measured intensity ratios $I_{KaL^{(1)}} : I_{KaL^{(0)}}$ of the satellite-to-parent diagram x-ray lines and the single K shell ionization cross section S_K reported in the literature. Because in first approximation shake and TS1 processes do not depend on the mechanism leading to the creation of the core vacancy, the L -shell shake probability and TS1 cross section can be assumed to be approximately the same in photoionization and electron bombardment. The magnitude of the TS2 process could thus be probed by comparing the KaL x-ray satellite yields induced in the samples by the photon and electron impact.

The TS1 process which predominates at near-threshold excitation energies decreases rapidly with growing photoelectron energy. The shake process has exactly the opposite behavior, ie. the probability increases with growing excitation energy until the so-called sudden approximation regime is reached. At saturation the change of the atomic potential is fast enough to permit the shake probability to be calculated within the SA model. As in our project the average energy of the x-ray tube bremsstrahlung lay in the saturation domain, the satellite yields determined in the photoionization measurements could not be compared directly to those obtained in the electron-induced measurements. To determine the variation of the shake plus TS1 probability as a function of the excitation energy, theoretical predictions computed within the models of Roy and Thomas were used. Both theoretical curves were anchored to the experimental probabilities determined in the x-ray tube measurements. The TS2 cross sections were finally obtained from the differences between the experimental ratios $S_{KL} : S_K$ fitted with a Grynski-like function and the average curve corresponding to the two theoretical models. In this method we assumed that the amplitude describing the interference between the three mechanisms (shake, TS1, TS2) may be neglected. The maximum contribution of the TS2 process to the double KL ionization was found to be about 40% for Al, 25% for Ca and 15% for Co. The TS2 contribution was further found to diminish approximately as Z^{-1} .

The main objective of the third project was to determine the 3s (M_I subshell) atomic-level width for a variety of elements comprised between xenon ($Z=54$) and iridium ($Z=77$). Atomic level widths and related x-

ray linewidths are of interest in both theoretical and experimental physics. In theory they provide sensitive tools to check the reliability and precision of models such as the independent-particle approximation or the many-body perturbation approach. In particular they are of interest to probe the goodness of theoretical predictions concerning total vacancy lifetimes, radiative and radiationless transition probabilities, or fluorescence yields. In experimental analysis methods based on sample x-ray emission such as x-ray fluorescence spectroscopy (XFS) and particle-induced x-ray emission (PIXE), a good knowledge of the transition widths is also crucial to get reliable results. Similarly, in a variety of experiments in which weak structures must be extracted from the tails of strong close-lying diagram transitions, the line shapes of the latter have to be known accurately to obtain precise results. Radiative Auger transitions are examples of such weak structures sitting on the low-energy tails of intense diagram lines. Furthermore for high-resolution x-ray spectroscopy a precise knowledge of x-ray line widths is very helpful because it permits one to improve data analysis by diminishing the number of free fitting parameters and anchoring the natural line widths of the observed transitions to known values. Satellite x-rays that originate from the radiative decay of multiple-vacancy states are often poorly separated from their parent diagram line. In this case the energy and yield of the satellite line can be fitted in a reliable way only if the width of the Lorentzian representing the natural line shape of the neighboring main line is known precisely.

Several review papers dealing with atomic-level widths can be found in the literature. Most rely on theory and only a few of them on experimental data. More recently Campbell and Papp assembled a large set of measured level widths and x-ray linewidths, and derived an internally consistent set of level widths for the K shell to the N_7 subshell for all elements across the periodic table. For the subshell M_1 , Campbell and Papp pointed out that in the region $55 \leq Z \leq 77$ there is a serious dearth of experimental data and that it would be of merit to perform modern XES measurements of the L_3 - M_1 transitions in that region of atomic number. Following this suggestion, we have determined the 3f atomic-level widths of several mid-heavy and heavy elements ($_{54}\text{Xe}$, $_{56}\text{Ba}$, $_{57}\text{La}$, $_{59}\text{Pr}$, $_{60}\text{Nd}$, $_{63}\text{Sm}$, $_{64}\text{Gd}$, $_{65}\text{Tb}$, $_{66}\text{Dy}$, $_{67}\text{Ho}$, $_{70}\text{Yb}$, $_{74}\text{W}$ and $_{77}\text{Ir}$). As the width of a x-ray transition is given by the sum of the widths of the two atomic levels involved in this transition and because M_5 level widths are known with a precision of about 0.1 eV, the L_3 atomic level widths were determined first from the measured line widths of the L_3 - M_5 transitions. Subtracting then the so-obtained L_3 widths from the line widths of the L_3 - M_1 transitions the M_1 level widths of interest could be determined with a precision of about 5%.

Due to L_1L_3N and L_2L_3N Coster-Kronig transitions, L_3 x-ray lines are generally broadened by unresolved N satellite structures. This broadening makes the data analysis more difficult and the obtained results less reliable. This difficulty, however, can be circumvented by irradiating the targets with monoenergetic synchrotron radiation, using excitation energies bigger than the L_3 edges of the investigated elements but smaller than their L_2 and L_1 edges. For this reason, the measurements were performed at the European Synchrotron Radiation Facility (ESRF) in Grenoble.

Outside the lanthanide region, differences of about -2 eV were found between the M_1 widths obtained in our work and the values recommended by Campbell and Papp. In the lanthanide region an opposite trend was

observed, our values being up to 1 eV bigger than those of Campbell and Papp. In this region, the M_1 widths were further found to grow with the total spin of the open $4f$ subshell. Deviations up to 3 eV relative to the values one would have expected from an interpolation of the widths found outside the rare-earth region were observed. The deviations could be explained qualitatively by a splitting effect resulting from the coupling of the $3s$ electron spin in the initial excited state with the total spin of the open $4f$ level.

Spin-off results of this third project were reliable experimental data concerning the L_3 level widths and L_3 - $M_{4,5}$ and L_3 - M_1 energies for the thirteen investigated elements. Whereas a good agreement with Campbell and Papp's values was found for the L_3 level widths, significant deviations with existing experimental information concerning the energies of the L_3 - $M_{4,5}$ and L_3 - M_1 transition were observed.

Part I

***L*-shell shake processes resulting from 1s photoionization in elements 11 $\leq Z \leq 17$**

O. Mauron, J.-Cl. Dousse, and J. Hozowska

Department of Physics, University of Fribourg, Chemin du Musée 3, CH-1700 Fribourg, Switzerland

J. P. Marques and F. Parente

*Centro de Física Atómica e Departamento de Física da Universidade de Lisboa,
Avenida Professor Gama Pinto 2, 1649-003 Lisboa, Portugal*

M. Polasik

Faculty of Chemistry, Nicholas Copernicus University, Gagarina 7, 87-100 Toruń, Poland

(Received 11 July 2000; published 10 November 2000)

The photoinduced $K\alpha$ x-ray spectra of elements between sodium and chlorine were measured by means of high-resolution crystal diffractometry. The $K\alpha_{1,2}L^{(1)}$ satellites were observed and resolved from the corresponding diagram lines. The probabilities for producing via shake processes $K^{(1)}L^{(1)}$ double-hole states were deduced from the satellite to parent diagram line yield ratios. The results are compared to theoretical sudden approximation predictions. A satisfactory agreement is found except for sodium and chlorine for which our experimental results are markedly underestimated by the calculations.

PACS number(s) : 32.30.Rj, 32.80.Fb, 34.50.Fa

I. INTRODUCTION

Atomic inner-shell photoionization is a process in which a single photon can be assumed to interact with a single bound electron. Direct multiple ionization caused by photoionization can be considered as negligibly small but excited atomic states with more than one inner-shell vacancy are, however, frequently observed as a result of photoionization [1]. The observation in K x-ray spectra of satellites emitted when the primary excited states decay proves that processes other

than radiationless transitions do contribute to the multiple excitation. In fact, when a sudden change in atomic potential occurs, there exists a probability of an atomic electron to be excited to an unoccupied bound state or to the continuum. These processes are called shake-up and shake-off, respectively. The atomic potential “seen” by an electron may change because of a fast removal of another innermost electron or because of a sudden change of nuclear charge due to nuclear decay (α -particle emission, β decay, or electron capture).

Experimental evidence of atomic excitation due to the production of an inner-shell vacancy, through photoionization, electron-impact ionization, and internal conversion, has been established a long time ago in the study of satellite lines or satellite continuum in x-rays and photoelectron spectra [2-4].

Satellite yields observed in photoinduced K x-ray spectra can be assumed to result quasi-exclusively from shake processes. Using this assumption we have determined the probabilities for L -shell shake processes following 1s photoionization in the elements comprised between $11 \leq Z \leq 17$. The L -shell shakeoff plus shakeup probabilities were determined from the measured intensity ratios of the $KL^{(1)}$ satellites to the $KL^{(0)}$ parent diagram lines. All measurements were performed with pure elements, except for chlorine for which two different compounds were employed (NaCl and RbCl). In order to probe the size of chemical effects on the shake probabilities, a pure Na target and a compound NaCl one were used for the measurements of the K x-ray emission spectrum of sodium.

II. EXPERIMENT

A. Experimental method

The L -shell shake probabilities were deduced from the observed $X_{KaL^{(1)}} : X_{KaL^{(0)}}$ relative satellite x-ray yields. For the yields $X_{KaL^{(0)}}$ of the diagram lines, we have summed the intensities of the $K\alpha_{1,2}$ transitions and unresolved M satellite structures. Depending on the elements, the complex L satellite structures were fitted with two or three components, the intensities of which were added to get the $X_{KaL^{(1)}}$ yields. From the so-determined relative x-ray yields $X_{KaL^{(1)}} : X_{KaL^{(0)}}$, the primary vacancy yield ratios $I_{KaL^{(1)}} : I_{KaL^{(0)}}$ were then computed, using simple statistical considerations to account for the L -vacancy rearrangement by intra-atomic electron transitions preceding the K x-ray emission. Finally, the L -shell shake probabilities were calculated from these $I_{KaL^{(1)}} : I_{KaL^{(0)}}$ ratios which represent the percentage of KL double-vacancy states relative to K single-vacancy states just after the 1s photoionization of the target atoms.

TABLE I. *Experimental settings.*

| Z | Target | X-ray Tube | Acquisition time (s) | Crystal | Reflection order | h_{KL}^a |
|----|--------|-------------|----------------------|---------|------------------|------------|
| 11 | Na | 40 kV 20 mA | 60000 | TIAP | 1 | 142 |
| 11 | NaCl | 40 kV 20 mA | 40000 | TIAP | 1 | 109 |
| 12 | Mg | 40 kV 20 mA | 12000 | TIAP | 2 | 80 |
| 13 | Al | 30 kV 10 mA | 8000 | ADP | 1 | 57 |
| 14 | Si | 30 kV 10 mA | 8000 | ADP | 1 | 49 |
| 15 | P | 25 kV 10 mA | 6000 | ADP | 1 | 37 |
| 16 | S | 40 kV 20 mA | 6000 | ADP | 1 | 34 |
| 17 | RbCl | 30 kV 15 mA | 20000 | ADP | 1 | 20 |
| 17 | NaCl | 30 kV 15 mA | 6000 | ADP | 1 | 23 |

^aParameter describing the photoelectron velocity (see text).

B. Instrumentation

The measurements of the photoinduced K x-ray spectra were performed at the University of Fribourg by means of a reflecting-type Von Hamos curved crystal spectrometer [5]. The main characteristics of this instrument were already presented in several previous papers [1,6,7]. Thus, in the following, only the features specific to the setup used for the present experiment will be discussed.

The principal elements of the spectrometer are an x-ray source defined by a rectangular slit, a cylindrically bent crystal, and a position-sensitive detector. The vertical rectangular slit consisted of two juxtaposed Ta pieces 0.3 mm thick and 10 mm high. For all measurements a slit width of 0.2 mm was used. The targets were irradiated with the bremsstrahlung of a Cr x-ray tube. Each target was aligned around a vertical axis so that the angles between the target plane and the irradiation and observation directions were the same. For the Al, Si, P, S, and Cl measurements, the spectrometer was equipped with a 5-cm-wide \times 10-cm-high \times 0.3-mm-thick (101) ADP crystal ($2d = 10.642 \text{ \AA}$). For Na and Mg a (001) TIAP crystal ($2d = 25.900 \text{ \AA}$) was employed. The Bragg-angle domain covered by the Von Hamos spectrometer extends from 24.4° to 61.1° . For the ADP and TIAP crystals the corresponding energy intervals are thus comprised for first-order reflections between 1.331 and 2.820 keV, and 0.547 and 1.158 keV, respectively. Both crystals were curved cylindrically to a nominal radius of 25.4 cm. The measurements, however, were performed at a focusing distance of 24.9 cm, for which the best

instrumental resolution was obtained. All elements were measured in first order of reflection except Mg which was measured in second order because the $K\alpha$ x-ray spectrum of this element falls exactly in the gap between the energy bandwidths covered by the two crystals.

In the Von Hamos slit geometry the instrumental broadening is determined by the slit aperture, precision of the crystal curvature, crystal mosaicity, and by the spatial resolution of the position-sensitive detector. For the measurements performed with the ADP crystal, the spectrometer resolution varied between 0.37 eV (Al spectrum) and 1.28 eV (Cl spectrum), the slit contribution being 0.23 eV and 0.85 eV, respectively. For the Na and Mg measurements which were performed with the TIAP crystal, the instrumental broadening amounted to 1.20 eV (slit contribution of 0.33 eV included) and 0.64 eV (slit : 0.21 eV), respectively. The better resolution of the Mg measurement is due to the fact that in this case, as mentioned above, the spectrum was observed in second order.

The x rays were recorded with a 27.65-mm-long and 6.9-mm-high charge-coupled-device (CCD) position-sensitive detector, having a depletion depth of 50 μm . The 27- μm pixel resolution of the CCD being many times better than the natural linewidth of the observed transitions, a software binning of four columns was performed in order to obtain higher count rates in the position spectra. Finally the position spectra were calibrated in energy by means of the formulas (3) and (4) given in [5], using the $K\alpha_i$ energies quoted in Ref. [8]. The experimental settings used in the measurements are summarized in Table I.

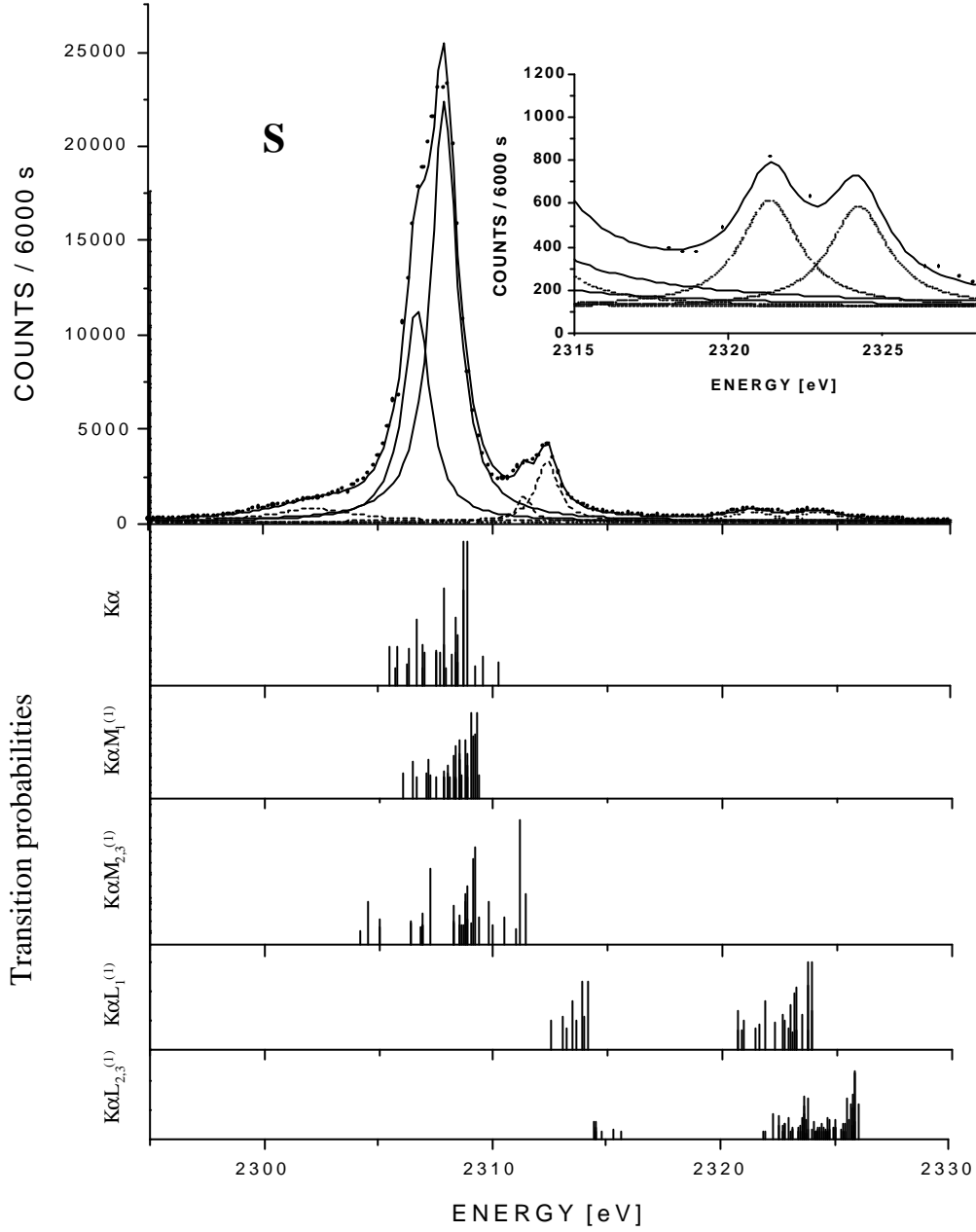


FIG. 1. High-resolution $K\alpha_{1,2}$ x-ray spectrum of sulfur. The L -satellite structure is shown enlarged in the inset. The dots correspond to the experimental data, the thick solid line to the total fit of the spectrum. The Lorentzians used to fit the diagram line and the L and M satellites are represented by thin solid lines, dotted lines, and dashed lines, respectively. The lower part of the figure shows the results of the MCDF calculations. The stick spectra represent the relative strengths of the components pertaining to the $2p$ - $1s$ transition with, respectively, no spectator vacancy or one spectator vacancy in the M_1 , $M_{2,3}$, L_1 or $L_{2,3}$ subshell. Each stick spectrum was normalized so that the sum of the transition probabilities is equal to one.

C. Targets

The elemental Na target was prepared by rolling carefully a lump of the soft and extremely reactive

metal until a foil with a thickness of about 0.2 mm was attained. The thin foil was then glued on an aluminum backing and brought promptly into the high-vacuum chamber of the spectrometer for the

measurements. The Mg and Al targets consisted of thin metallic foils, 0.01 mm and 0.006 mm thick, respectively. The Al foil was mounted on an aluminum frame whereas the Mg target was glued on a backing made of stainless steel, one of the rare metals with which magnesium does not react. The Si and S polycrystalline targets were prepared by dusting the powdered crystals onto an adhesive backing to form a continuous coating. For the P target, we crushed small high-purity phosphorus granules and dusted the obtained powder as before on an adhesive backing. For Cl, due to safety reasons, we employed only compounds, namely NaCl and RbCl. The latter were prepared with the same technique as the one used for Si and S. All targets had a 20-mm-high \times 5-mm-wide rectangular shape with thicknesses ranging from several μm to a few tenths of mm.

III. THEORY

A. Sudden approximation

In the incident particle (photons or electrons) high-energy limit, one may use the so-called sudden approximation [9], in which the atomic excitation is treated separately from the initial vacancy process. Experimental results of Carlson and Krause [3] and Carlson *et al.* [10], as well as theoretical predictions of Krause and Carlson [11], and Sachenko and Burtsev [12] indicate the validity of this approximation for atomic excitation following inner-shell vacancy production. Several calculations for rare-gas atoms in the sudden approximation are referred to in the paper of Mukoyama and Taniguchi [9], presenting results for the probabilities of atomic excitation as a result of

vacancy production in the $1s$, $2s$, and $2p$ shells for elements with Z between 2 and 36 in the sudden approximation. These authors used non relativistic Hartree-Fock-Slater wave functions.

B. The multiconfiguration Dirac-Fock method

The multiconfiguration Dirac-Fock (MCDF) code of Desclaux and Indelicato [13-15] was used in this work to generate the wave functions. The MCDF method starts from a no-pair Hamiltonian, written in the following form [14,16,17]:

$$\mathcal{H}^{\text{nopair}} = \sum_{i=1}^m \mathcal{H}_D(r_i) + \sum_{i<j} \mathbf{n} \left(\vec{r}_i - \vec{r}_j \right). \quad (1)$$

\mathcal{H}_D is an one-electron operator and \mathbf{n} is an operator representing the two-body interaction

$$\mathbf{n}_{ij} = \Lambda_{ij}^{++} \mathbf{n}_{ij} \Lambda_{ij}^{++}, \quad (2)$$

where, in the Coulomb gauge,

$$\mathbf{n}_{ij} = \frac{1}{r_{ij}} - \frac{\vec{\mathbf{a}}_i \cdot \vec{\mathbf{a}}_j}{r_{ij}} - \frac{\vec{\mathbf{a}}_i \cdot \vec{\mathbf{a}}_j}{r_{ij}} [\cos(\mathbf{w}_{ij} r_{ij}) - 1] + \left(\vec{\mathbf{a}}_i \cdot \vec{\nabla}_i \right) \left(\vec{\mathbf{a}}_j \cdot \vec{\nabla}_j \right) \frac{\cos(\mathbf{w}_{ij} r_{ij}) - 1}{\mathbf{w}_{ij}^2 r_{ij}}, \quad (3)$$

and $\Lambda_{ij}^{++} = \Lambda_i^+ \Lambda_j^+$ is an operator projecting onto the one-electron positive continuum which avoids coupling the positive- and negative-energy continuum. We define $r_{ij} = |\vec{r}_i - \vec{r}_j|$ for the interelectronic distance, \mathbf{w}_{ij} for the energy of the exchanged photon between the electrons and $\vec{\mathbf{a}}_i$ the Dirac matrices ($\vec{\nabla}$ acts only on the r_{ij} and not on the following wave function).

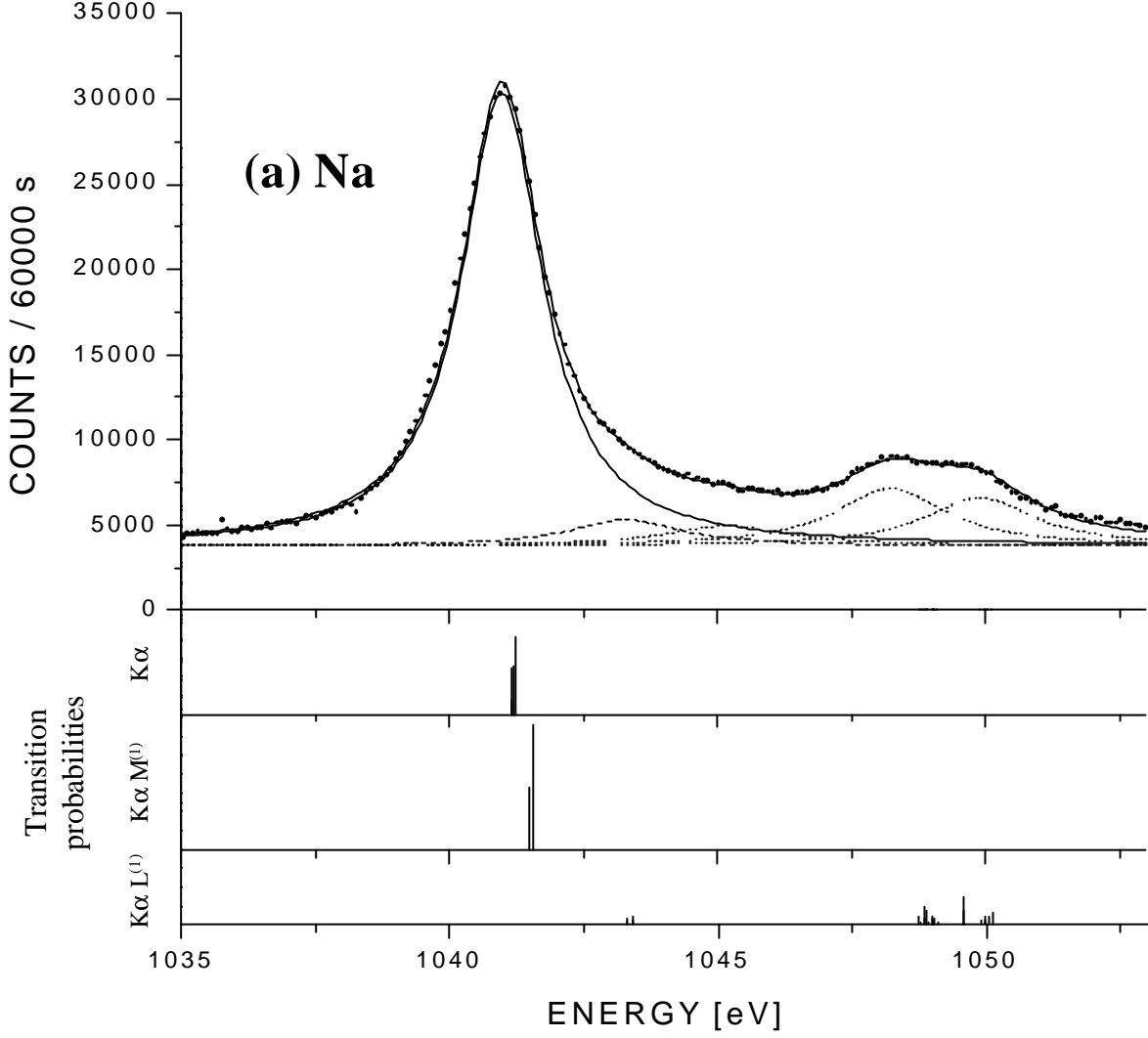


Fig. 2a. *High-resolution x-ray spectra of sodium (elemental Na target) with the corresponding MCDF stick spectra. For the fitted satellites, the same representation as in Fig. 1 is used.*

The total wave function is calculated with the help of the variational principle. The total energy is the eigenvalue of the equation

$$\mathcal{H}^{\text{nopair}} \Psi_{\Pi, J, M}(r_1, \dots, r_m) = E_{\Pi, J, M} \Psi_{\Pi, J, M}(r_1, \dots, r_m), \quad (4)$$

where $\bar{\Pi}$ is the parity, \bar{J} is the total angular momentum eigenvalue, and M is the eigenvalue of its projection on the z axis J_z . The MCDF method is defined by the particular choice of a trial function

to solve Eq. (4) as a linear combination of configuration state functions (CSF)

$$|\Psi_{\Pi, J, M}\rangle = \sum_{n=1}^n c_n |\mathbf{n}, \Pi, J, M\rangle. \quad (5)$$

The CSF are eigenfunctions of the parity $\bar{\Pi}$, the total angular momentum \bar{J} , and its projection J_z . The CSF are antisymmetric products of one-electron wave functions expressed as linear

combinations of Slater determinants of Dirac four-spinors

$$|n, \Pi, J, M\rangle = \sum_{i=1}^{N_n} d_i \begin{vmatrix} \mathbf{y}_1^j(r_1) & \cdots & \mathbf{y}^j(r_1) \\ \vdots & \ddots & \vdots \\ \mathbf{y}_1^j(r_m) & \cdots & \mathbf{y}_m^j(r_m) \end{vmatrix}. \quad (6)$$

The d_i coefficients are obtained by requiring that the CSF are eigenstates of \vec{J}^2 and J_z . A variational principle provides the integro-

differential equations to determine the radial wave functions and a Hamiltonian matrix that provides the mixing coefficients c_n by diagonalization. Exact one-electron radiative corrections (self-energy and vacuum polarization) are added afterwards.

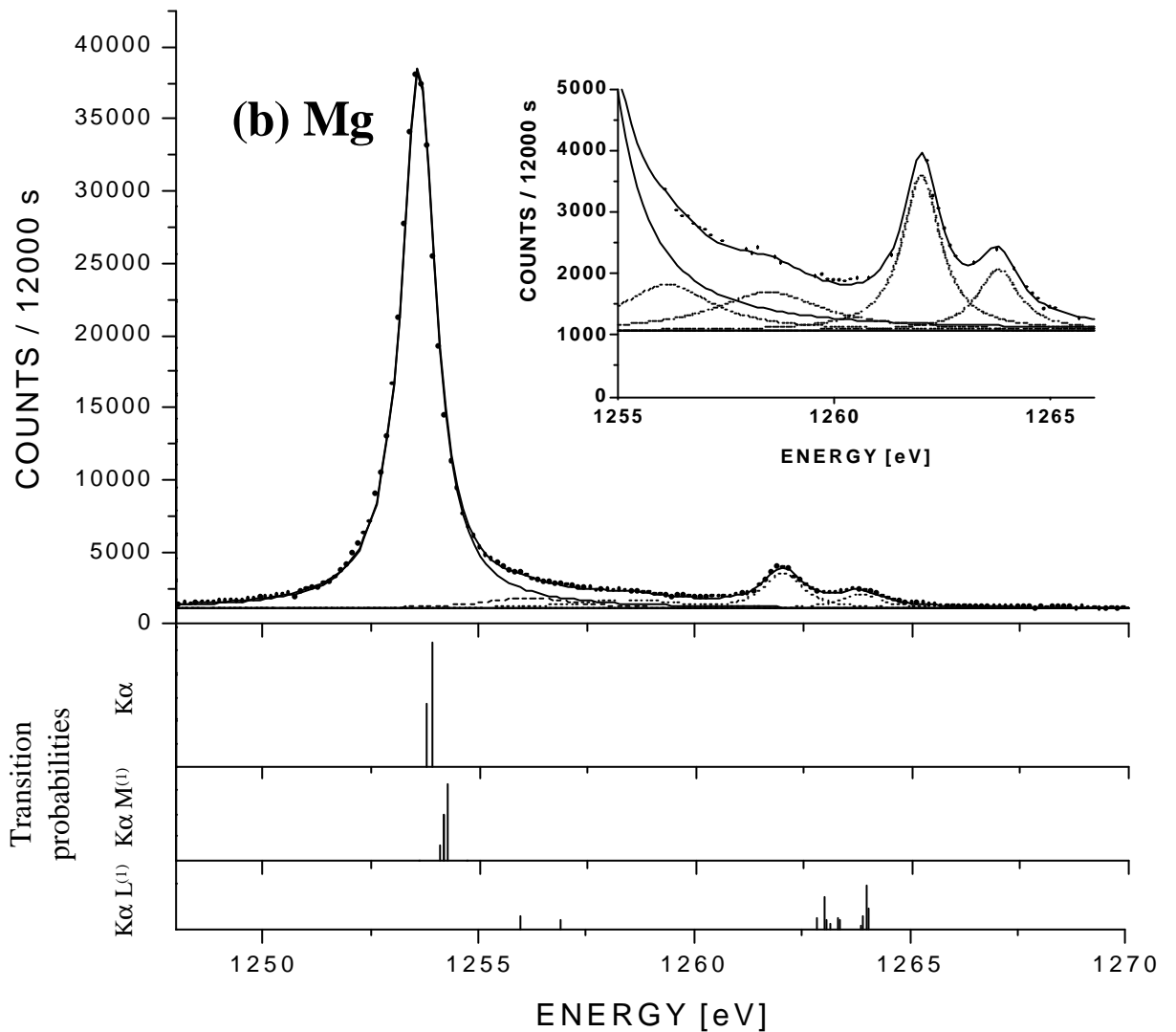


Fig. 2b. High-resolution x-ray spectra of magnesium with the corresponding MCDF stick spectra. For the fitted satellites, the same representation as in Fig. 1 is used.

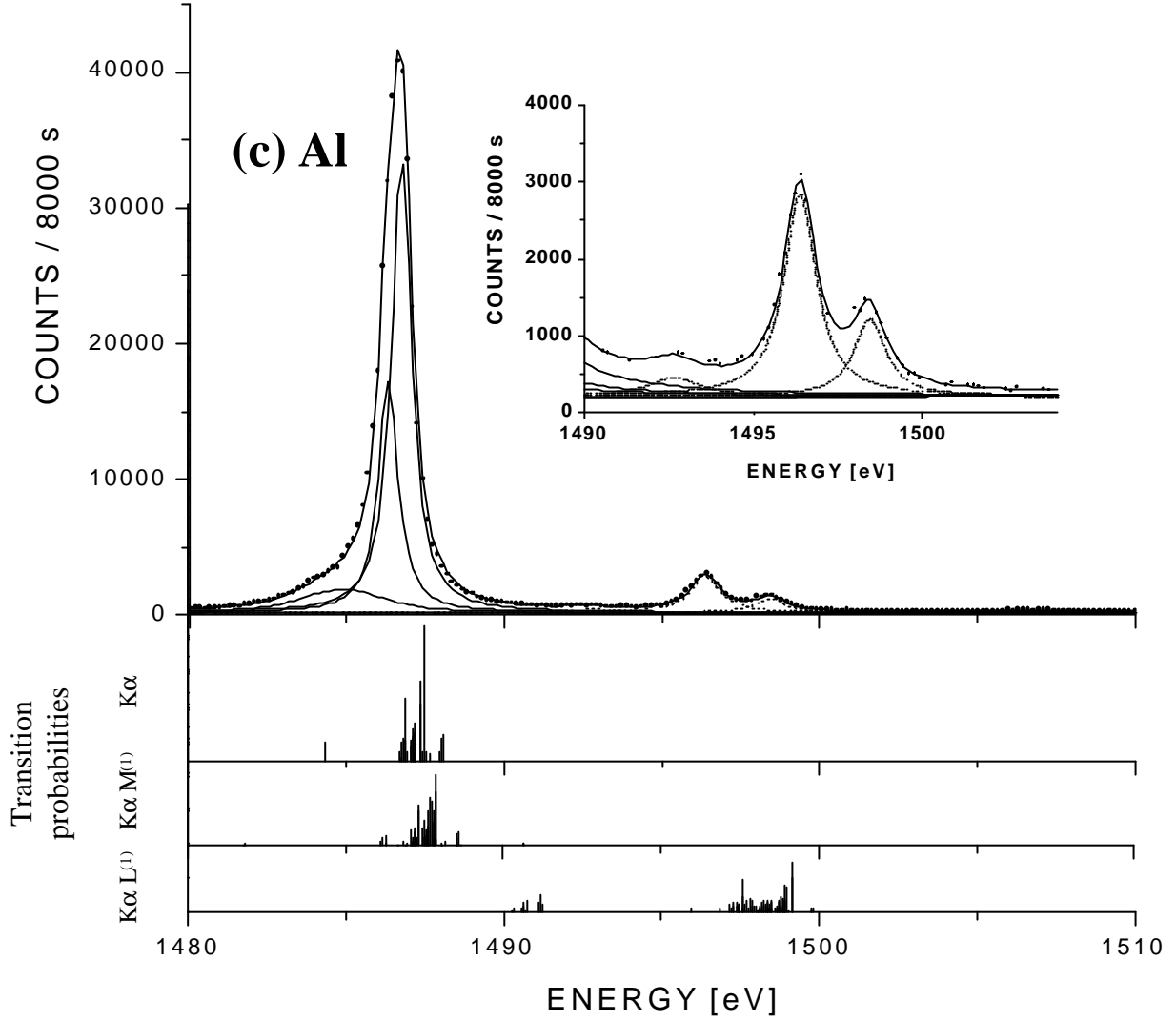


Fig. 2c. High-resolution x-ray spectra of aluminum with the corresponding MCDF stick spectra. For the fitted satellites, the same representation as in Fig. 1 is used.

C. Calculations

We used relativistic MCDF wave functions in monoconfiguration for the neutral atom (initial state) and for the ion with a single 1s hole (final state). In the sudden approximation, the overlap between the initial and final wave functions gives the electron transition probability between those two states due to a sudden change in the atomic potential.

According to Carlson *et al.* [3] the probability for removing an electron from an orbital nlj , is given by

$$P_{nlj} = 1 - \left[\left| \int \mathbf{y}_{nlj}^* \mathbf{y}_{nlj} d\mathbf{t} \right|^2 \right]^N - P_F, \quad (7)$$

where \mathbf{y}_{nlj} and \mathbf{y}_{nlj}' represent the electron wave functions of the orbital nlj in the neutral atom and the ion with a single 1s vacancy, respectively, N is the number of electrons in the nl shell, and

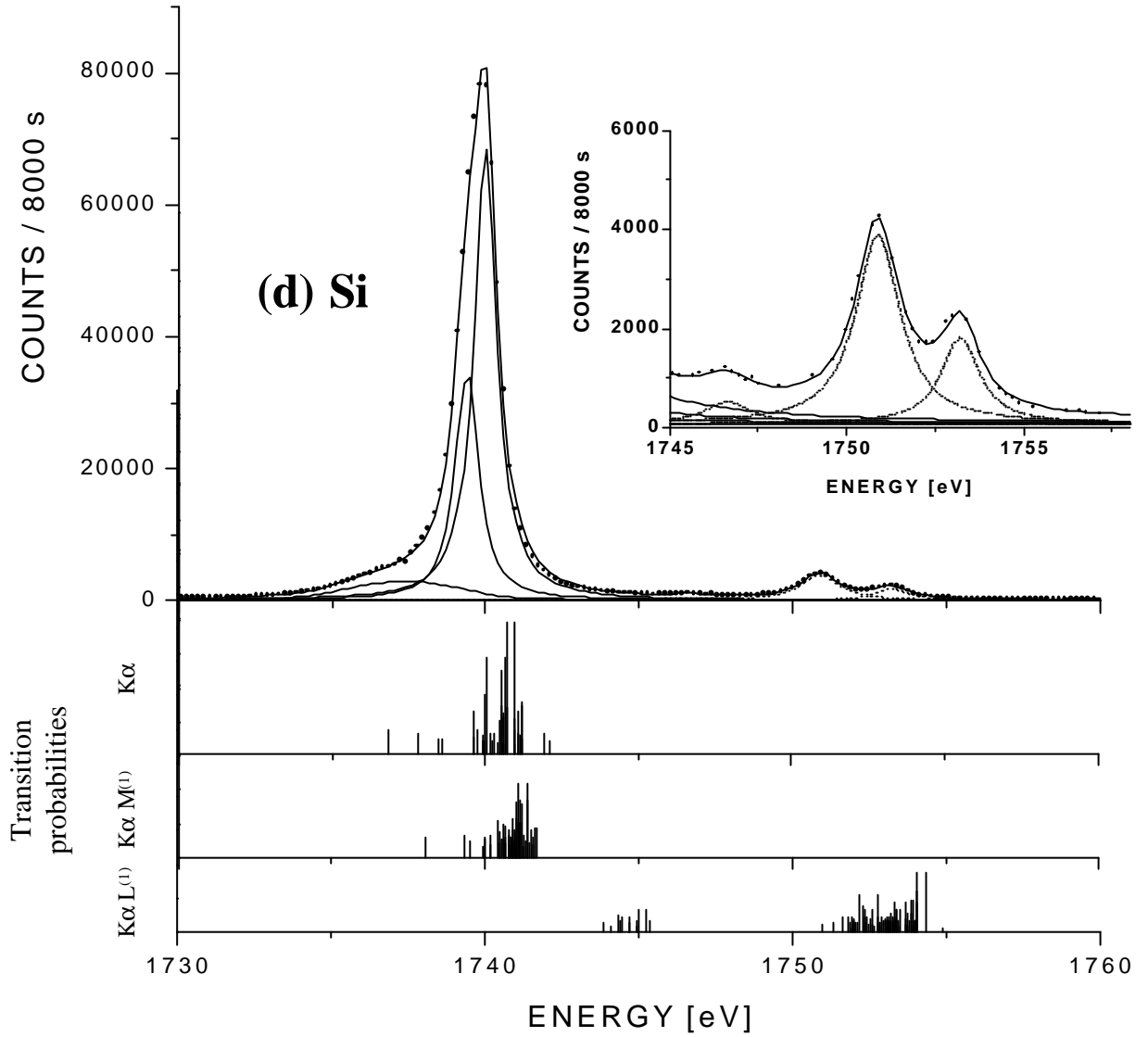


Fig. 2d. High-resolution x-ray spectra of silicon with the corresponding MCDF stick spectra. For the fitted satellites, the same representation as in Fig. 1 is used.

$$P_F = \sum_{n'=1}^x \frac{NN'}{2j+1} \left| \int \mathbf{y}_{n'l_i}^* \mathbf{y}_{nl_j} d\mathbf{t} \right|^2 \quad (8)$$

with $n \neq n'$, N' being the number of electrons in the $n'l$ shell, x is the principal quantum number of the highest occupied state and thus P_F represents a correction introduced by the condition that the electron shake-up transitions to occupied levels are not physically allowed. The second term of Eq. (7) gives the probability that an electron initially in

orbital nlj remains in an orbital with the same quantum numbers in the final state.

Many shake calculations are based on the relation (7). Depending on the scheme employed to compute the wave functions, the results vary somewhat. In the calculations performed with the code of Desclaux, the wave functions were calculated for all possible \bar{J} values and the shake probability was then obtained from the

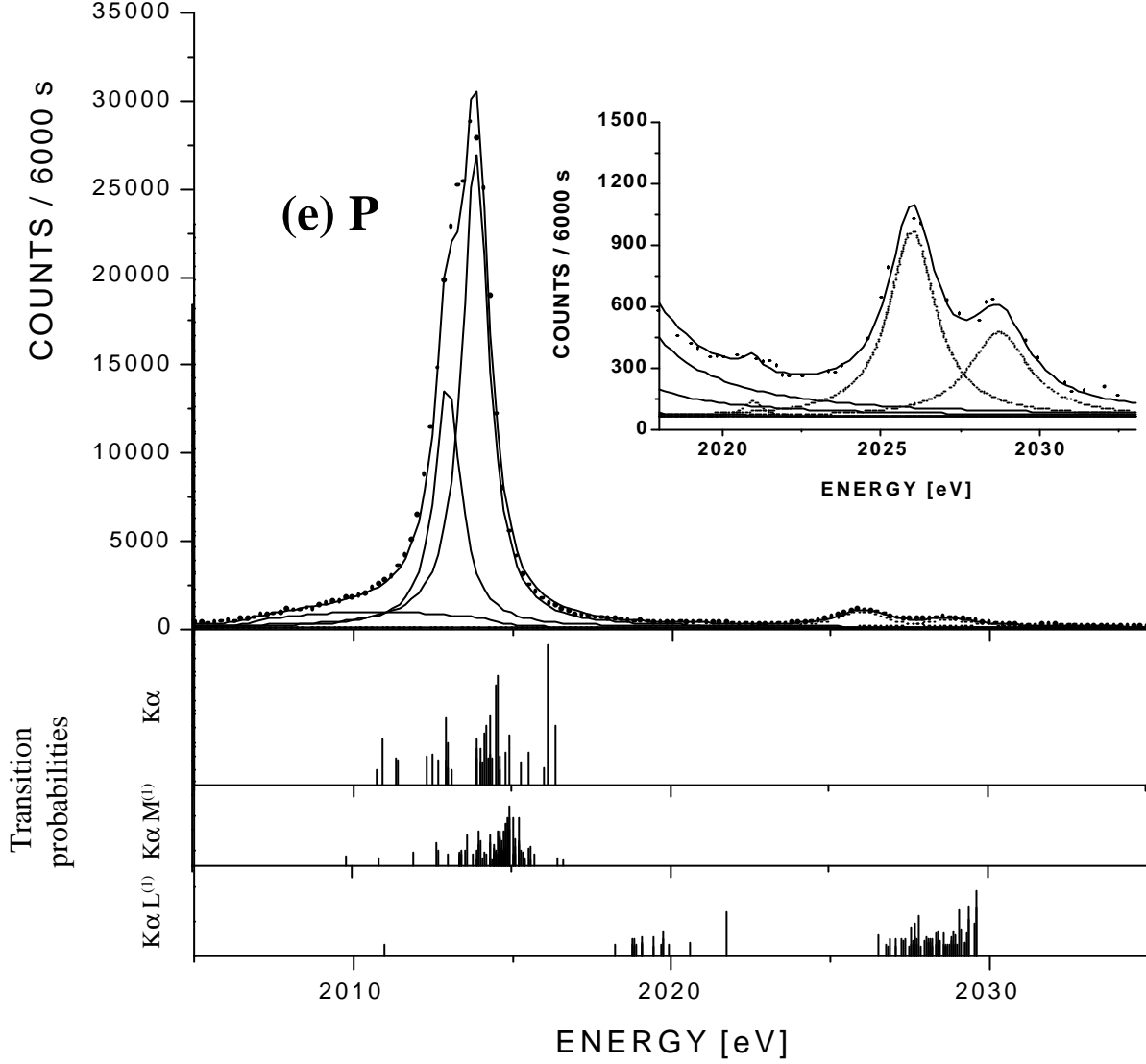


Fig. 2e. High-resolution x-ray spectra of phosphorous with the corresponding MCDF stick spectra. For the fitted satellites, the same representation as in Fig. 1 is used.

weighted sum of all overlap integrals. Complementary calculations were performed within the same approach but using self-consistent Dirac-Fock wave functions computed in the energy average level (EAL) scheme with the code of Dyll [18]. As expected, the results of the two MCDF calculations were found to differ slightly. They are presented in Fig. 3 together with theoretical predictions from [9] based on nonrelativistic HFS (Hartree-Fock-Slater) wave functions.

IV. DATA ANALYSIS

The observed K x-ray spectra were analyzed by means of the least-squares-fitting computer program MINUIT [19], employing Lorentzian profiles to fit the diagram and satellite lines. Lorentz functions were chosen because the instrumental response of the Von Hamos spectrometer operated in the slit geometry can be well reproduced by a Lorentz profile so that the convolution of the spectrometer response with the

natural line shape of the x-ray transitions remains a Lorentzian. As each satellite line consists of many overlapping components, their complex shape was reproduced by several juxtaposed Lorentzians, whose centroid position, amplitude, and width were used as free-fitting parameters. The same held for those diagram transitions for which an asymmetric shape was observed resulting from unresolved M satellite structures and, for certain elements, from open valence subshells in the ground state.

In order to better understand the structure of the measured spectra, and in particular to assign properly the fitted satellite yields, MCDF (multiconfiguration Dirac-Fock) calculations based on the MSAL (modified special average level) version [20] of the GRASP code [18] were performed for all investigated elements. In each "stick" spectrum resulting from the MCDF calculations, the transition probabilities were scaled so that their sum is equal to one. MCDF predictions reproduce quite well the general trends of the

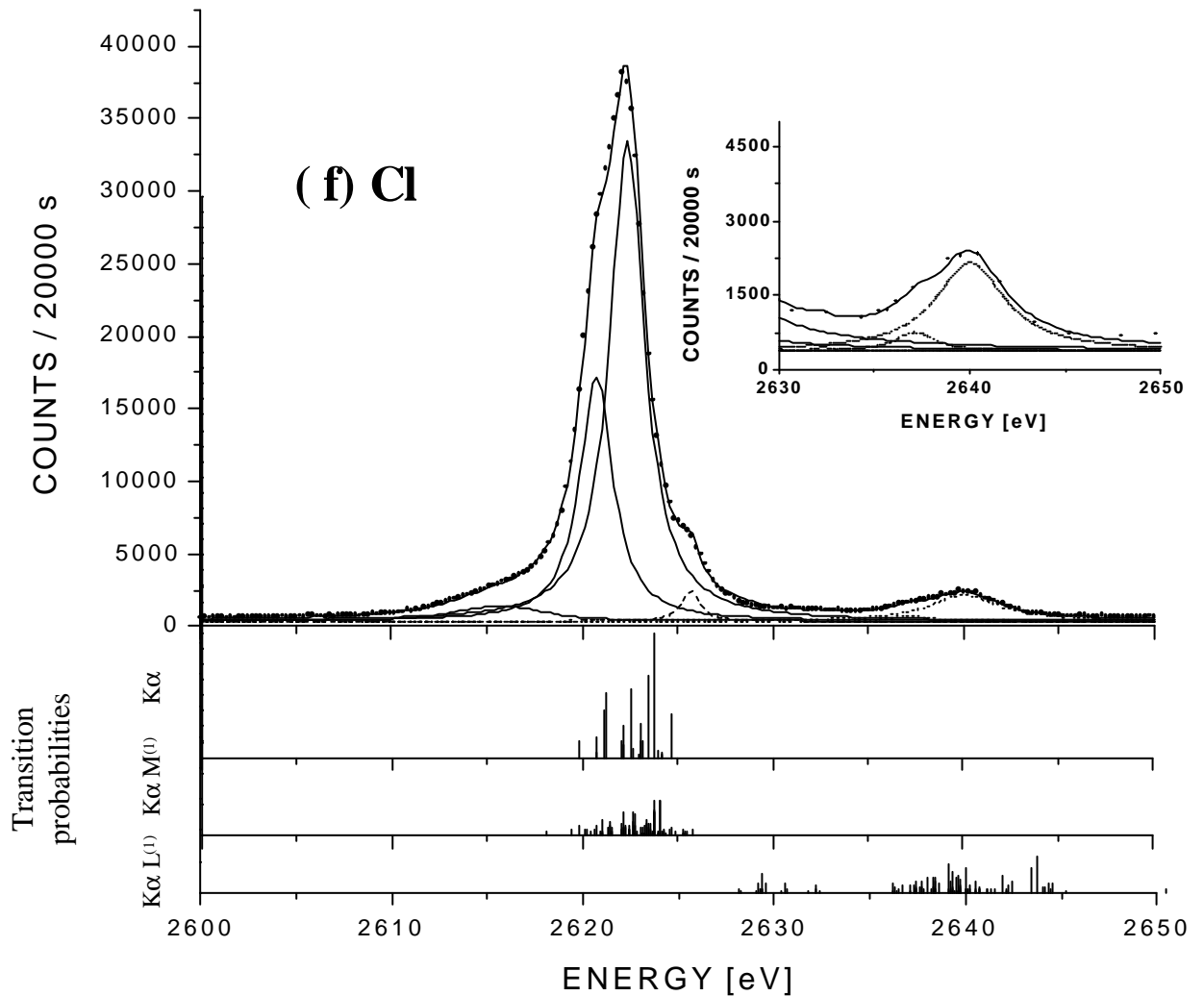


Fig. 2f. High-resolution x-ray spectra of chlorine (NaCl target) with the corresponding MCDF stick spectra. For the fitted satellites, the same representation as in Fig. 1 is used.

experimental x-ray spectra and were therefore very useful for the qualitative interpretation of the observed structures. However, deviations from the experimental energies and intensities of the satellite components were observed, making questionable quantitative detailed comparisons.

To illustrate the method used for the data analysis, the fitted $KaL^{(0,1)}$ x-ray spectrum of S is presented in Fig. 1. The first group of lines, centered around 2307 eV, corresponds principally to the Ka_1 and Ka_2 diagram transitions which were fitted with a single Lorentzian each. The intensity ratio $I(Ka_2) : I(Ka_1)$ and the energy difference $E(Ka_1) - E(Ka_2)$ were kept fixed in the fitting procedure at the values of 0.506 and 1.2 eV quoted in Refs. [21] and [8], respectively. As indicated by the MCDF calculations, a significant part of the fitted intensity is due to overlapping M satellite components.

The double bump structure above 2320 eV which was fitted with two Lorentzians (dotted lines) is clearly due to L satellites. The first peak (called Ka_3 in the literature) originates predominantly from $K-L_{2,3}$ transitions with one additional spectator hole

in the L_1 subshell while the second one (Ka_4) arises mainly from the radiative decay of $1s^{-1}2p^{-1}$ double-hole states. Furthermore, the $KaL_1^{(1)}$ and $KaL_{2,3}^{(1)}$ stick spectra show that there is a third group of L satellites below and around 2315 eV. However, these components could not be fitted because they are completely hidden by the overlapping M -satellite structure. Theory predicts that the probability to eject an electron from the $2s$ subshell as a result of the sudden production of a K hole is about 30 times smaller than the probability to eject an electron from the $3p$ subshell. As a consequence, the rather strong doublet occurring at 2312 eV cannot indeed be explained by the lower group of the $KaL_1^{(1)}$ satellites but is very certainly due to the higher-energy components of the $KaM_{2,3}^{(1)}$ satellite group. Similarly, the shoulder appearing on the left side of the diagram lines stems probably from the lower-energy components of the $KaM_{2,3}^{(1)}$ groupe. This excess of intensity around about 2302 eV cannot indeed be attributed to $K-LM$ radiative Auger (RAE) transitions [6,22], because the latter are expected to occur below 2287 eV (edge of the $K-L_3M_3^1P_1$ transition, the $K-LM$ RAE transition of highest energy as indicated by Larkins's table [23]).

TABLE II. *Correction factors and x-ray intensity ratios.*

| Z | Target | Correction factor | $X_{Ka_4} : X_{Ka_3}$ | $X_{KaL^{(1)}} : X_{KaL^{(0)}} (%)$ | |
|----|--------|-------------------|-----------------------|-------------------------------------|---|
| | | | | Present | Earlier |
| 11 | Na | 0.994 | 0.85 ± 0.02 | 27.1 ± 0.3 | 19.6^a [31] |
| 11 | NaCl | 0.992 | 1.00 ± 0.08 | 25.6 ± 0.5 | 18.9^a [31] |
| 12 | Mg | 1.018 | 0.39 ± 0.01 | 11.4 ± 0.1 | 13.9 ± 0.6^b [32] 16.1 ± 0.7^a [30] |
| 13 | Al | 1.015 | 0.382 ± 0.009 | 7.80 ± 0.08 | 10.2 ± 0.5^a [30] |
| 14 | Si | 0.994 | 0.452 ± 0.006 | 5.72 ± 0.03 | 11.4^a [33] |
| 15 | P | 0.990 | 0.47 ± 0.01 | 3.40 ± 0.06 | |
| 16 | S | 0.991 | 0.94 ± 0.02 | 2.57 ± 0.03 | |
| 17 | RbCl | 0.987 | 5.5 ± 0.6 | 4.9 ± 0.1 | |
| 17 | NaCl | 0.990 | 2.1 ± 0.1 | 4.5 ± 0.2 | |

^aExcitation mode : electrons.

^bExcitation mode : photons (Rh x-ray tube, 40 kV, 40 mA).

As it can be seen from Fig. 1, the diagram lines, which were fitted with two Lorentzians, consist in fact of many components whose energies spread over about 5 eV. This is related to the open $3p$ subshell of S in the ground state. Depending on the coupling between the two $3p$ vacancies with the $1s$ hole in the initial state and with the $2p$ hole in the final state, several different initial and final states do indeed exist which give rise to numerous transitions as shown in the stick spectrum labeled $K\alpha$.

MCDF calculations concerning $K\alpha L^{(1)}M^{(1)}$ transitions (i.e., $2p-1s$ transitions with one spectator vacancy in the L shell plus one in the M shell) were also performed. The results were found to be very similar to those corresponding to the $K\alpha L^{(1)}$ transitions. As a consequence, their contribution to the observed x-ray spectrum is implicitly included in the three Lorentzians employed to fit the L -satellite structures.

Finally, for sulfur the $X_{K\alpha L^{(1)}} : X_{K\alpha L^{(0)}}$ yield ratio was computed by taking for $X_{K\alpha L^{(0)}}$ the sum of the yields of the five Lorentzians represented by solid lines (diagram transitions) and dashed lines ($K\alpha M^{(1)}$ satellites) and for $X_{K\alpha L^{(1)}}$ the sum of the yields of the two Lorentzians depicted with dotted lines ($K\alpha M^{(1)}$ satellites) and for $X_{K\alpha L^{(1)}}$ the sum of the yields of the two Lorentzians depicted with dotted lines ($K\alpha L^{(1)}$ satellites, $K\alpha L^{(1)}M^{(1)}$ components included).

A similar analysis was performed for the other investigated elements, namely Na, Mg, Al, Si, P, and Cl. The corresponding fitted $K\alpha L^{(0,1)}$ x-ray spectra are presented in Fig. 2 with the associated $K\alpha$, $K\alpha L^{(1)}$, and $K\alpha M^{(1)}$ MCDF stick spectra. Note

TABLE III. Weighting factors of the L_i subshells used in the rearrangement calculations.

| Elements | w_{L_1} | w_{L_2} | w_{L_3} |
|----------|-----------|-----------|-----------|
| Na | 0.115 | 0.299 | 0.586 |
| Mg | 0.091 | 0.306 | 0.603 |
| Al | 0.098 | 0.269 | 0.633 |
| Si | 0.112 | 0.285 | 0.603 |
| P | 0.114 | 0.297 | 0.589 |
| S | 0.123 | 0.271 | 0.606 |
| Cl | 0.134 | 0.268 | 0.598 |

that for Na whose ground state is characterized by a single $3s$ vacancy and especially for Mg which has only closed subshells in the ground state, the numbers of components in the stick spectra are considerably smaller than for other elements. For Cl, the bump occurring on the high-energy flank of the diagram line originates from the upper group of M satellites as in the case of S.

Although the energy differences between the diagram and L -satellite lines are small (10-20 eV), the dependence on the photon energy of the x-ray absorption in the target, crystal reflectivity and solid angle of the spectrometer were probed and their effect on the $X_{K\alpha L^{(1)}} : X_{K\alpha L^{(0)}}$ x-ray yield ratios checked. The corrections were found to be small (1%-2%) and to partly cancel each other. The total correction factors, the intensity ratios $X(K\alpha_4) : X(K\alpha_3)$ and the corrected $X_{K\alpha L^{(1)}} : X_{K\alpha L^{(0)}}$ yield ratios are presented in Table II. For Na and Cl, which were measured with two different targets each, results of both measurements are given. Experimental data from other groups, if existing, are also quoted.

TABLE IV. Rearrangement factors R_L , partial fluorescence yield ratios \mathbf{w}_L , x-ray yield ratios x_L , and initial vacancy yield ratios i_L for the investigated targets

$$(\mathbf{w}_L = \mathbf{w}_{KaL^{(0)}} : \mathbf{w}_{KaL^{(1)}}, x_L = X_{KaL^{(1)}} : X_{KaL^{(0)}}, i_L = I_{K^{(1)}L^{(1)}} : I_{K^{(1)}L^{(0)}}).$$

| Z | Target | R_L | \mathbf{w}_L | x_L (%) | i_L (%) |
|----|--------|-------------------|----------------|-----------------|-----------------|
| 11 | Na | 0.059 ± 0.043 | 0.911 | 27.1 ± 0.3 | 26.6 ± 2.2 |
| 11 | NaCl | 0.059 ± 0.043 | 0.911 | 25.6 ± 0.5 | 25.2 ± 2.0 |
| 12 | Mg | 0.076 ± 0.036 | 0.902 | 11.4 ± 0.1 | 11.2 ± 0.9 |
| 13 | Al | 0.087 ± 0.033 | 0.897 | 7.80 ± 0.08 | 7.71 ± 0.49 |
| 14 | Si | 0.094 ± 0.030 | 0.898 | 5.72 ± 0.03 | 5.70 ± 0.35 |
| 15 | P | 0.117 ± 0.027 | 0.900 | 3.40 ± 0.06 | 3.48 ± 0.21 |
| 16 | S | 0.132 ± 0.026 | 0.897 | 2.57 ± 0.03 | 2.67 ± 0.16 |
| 17 | RbCl | 0.144 ± 0.025 | 0.892 | 4.9 ± 0.1 | 5.1 ± 0.3 |
| 17 | NaCl | 0.144 ± 0.025 | 0.892 | 4.5 ± 0.2 | 4.7 ± 0.4 |

V. RESULTS AND DISCUSSION

A. L-shell rearrangement

The measured L -satellite yields reflect the distribution of the spectator holes at the moment of the K x-ray emission and not the initial distribution following the 1s photoionization which has to be known for the determination of the shake probabilities. Processes such as LMM Auger and L radiative transitions occurring prior to the K x-ray emission can indeed modify the number of spectator holes created by the shake process. In order to deduce the primary vacancy distributions from the observed satellite intensities, we employed the statistical method described in the Appendix of Ref. [1].

The probability W_p for a process, modifying the number of holes in the subshell X_i , to occur before the $K^{(1)}X_i^{(1)}$ doubly ionized state decays is given by

$$W_p = \frac{\Gamma_p}{\Gamma_K + \Gamma_{X_i}}, \quad (9)$$

where Γ_p is the transition width of this particular process and Γ_K and Γ_{X_i} are the total widths of the K shell and the subshell X_i .

For $KL^{(1)}$ satellites of the studied elements the electron rearrangement is governed by LMM Auger transitions and L radiative transitions, which both decrease the number of L vacancies by one. If one neglects the triply ionized states $K^{(1)}L^{(2)}$ which are poorly populated by photoinduced shake processes, the diagram and satellite x-ray emission yields $X_{KaL^{(n)}}$ are related to the initial vacancy yields $I_{K^{(1)}L^{(n)}}$ by the following equations:

$$X_{KaL^{(0)}} = (I_{K^{(1)}L^{(0)}} + R_L I_{K^{(1)}L^{(1)}}) \cdot \mathbf{w}_{KaL^{(0)}}, \quad (10)$$

$$X_{KaL^{(1)}} = (I_{K^{(1)}L^{(1)}} - R_L I_{K^{(1)}L^{(1)}}) \cdot \mathbf{w}_{KaL^{(1)}}, \quad (11)$$

where R_L is a scaling factor describing the electron rearrangement and $\mathbf{w}_{KaL^{(n)}}$ the partial K -shell fluorescence yield of the transition Ka with n spectator holes in the L shell. The initial vacancy yield ratio can then be deduced from the system of equations (10) and (11),

$$\frac{I_{K^{(1)}K^{(1)}}}{I_{K^{(1)}L^{(0)}}} = \frac{\left(\frac{X_{KaL^{(1)}}}{X_{KaL^{(0)}}} \right) \left(\frac{W_{KaL^{(0)}}}{W_{KaL^{(1)}}} \right)}{1 - R_L \left[1 + \left(\frac{X_{KaL^{(1)}}}{X_{KaL^{(0)}}} \right) \left(\frac{W_{KaL^{(0)}}}{W_{KaL^{(1)}}} \right) \right]}. \quad (12)$$

Taking into consideration that $L_i L_j M$ Coster-Kronig transitions do not modify the number of L holes, one obtains from Eq. (9) the following expression for the rearrangement factor of the subshell L_i :

$$R_{L_i} = \frac{\Gamma_{L_i} - \sum_j \Gamma_{L_i L_j M}}{\Gamma_K + \Gamma_{L_i}}. \quad (13)$$

The total L -shell rearrangement factor R_L can be written as the weighted sum of the coefficients R_{L_i} ,

$$R_L = \sum_i w_{L_i} R_{L_i} = \sum_i w_{L_i} \frac{\Gamma_{L_i}}{\Gamma_K + \Gamma_{L_i}} \left(1 - \sum_j f_{ij} \right), \quad (14)$$

where f_{ij} represent the relative Coster-Kronig yields and w_{L_i} the weighting factors of the subshells L_i . As $L_2 L_3 M$ Coster-Kronig transitions are energetically forbidden for the investigated elements, only the coefficients f_{12} and f_{13} need to be considered. They were taken from Ref. [24]. The weighting factors w_i are proportional to the numbers of initial holes in the subshells L_i , i.e., to the subshell shake probabilities. The latter were computed within the sudden approximation model by means of the method described in Sec. III. The so-obtained weighting factors w_i are given in Table III. The natural widths Γ_K and Γ_{L_i} were taken

from Ref. [25] and the fluorescence yields $W_{KaL^{(0)}}$ from [26]. The fluorescence yields $W_{KaL^{(1)}}$ were deduced from a linear interpolation of the values quoted in [27]. The rearrangement factors, fluorescence yield ratios, and initial vacancy yield ratios obtained for the different targets are summarized in Table IV.

B. Shake probabilities

If we assume that there is no correlation between the ejected electrons, the primary vacancy yields $I_{K^{(1)}L^{(h)}}$ ($h = 0, 1$) can be written as follows :

$$I_{K^{(1)}L^{(h)}} \approx S_K^{photo} \binom{8}{h} p_L^h (1 - p_L)^{8-h} \quad (15)$$

where S_K^{photo} is the photoionization cross section, p_L the average L -shell shake probability per electron, and $\binom{8}{h}$ the binomial coefficient. Using Eq. (15), one can express p_L as a function of the initial vacancy yield ratio

$$i_L := \frac{I_{K^{(1)}L^{(1)}}}{I_{K^{(1)}L^{(0)}}} = \frac{8p_L}{1 - p_L}, \quad p_L = \frac{i_L}{8 + i_L}, \quad (16)$$

The probability for the ionization via shakeoff plus shakeup processes of at least one electron from the L shell is then given simply by

$$P_L = 8p_L. \quad (17)$$

Introducing in Eq. (16) the initial vacancy yield ratios quoted in Table IV, one obtains from Eq. (17)

TABLE V. *Experimental L-shell shake probabilities.*

| Target | Na | NaCl | Mg | Al | Si | P | S | RbCl | NaCl |
|-----------|-------|-------|---------|--------|--------|--------|--------|--------|--------|
| P_L (%) | 26(2) | 24(2) | 11.0(9) | 7.6(5) | 5.6(3) | 3.5(2) | 2.6(2) | 5.1(3) | 4.7(4) |

the experimental L -shell shake probabilities P_L listed in Table V. The latter are compared in Fig. 3 to the results of the calculations performed within the sudden approximation model with the above-mentioned wave functions.

If one considers at first the pure elemental targets, one can see from Fig. 3 that the theoretical sudden approximation calculations reproduce satisfactorily the experimental results, except for the lightest element (Na). Actually, the three calculations give very similar results and all of them underestimate by a factor of about 1.5 the experimental shake probability of Na. An explanation for the observed discrepancy may reside in the fact that the theoretical calculations are based on the free atom model and are thus not fully adequate for solid targets in which solid-state effects may affect the shake probabilities. In our opinion, however, solid state effects cannot explain solely the deviations found for Na since for Ne theory predicts a shake probability of 18% which is also markedly smaller than the experimental value of $29\% \pm 3\%$ deduced from the x-ray yield ratio ($32\% \pm 3\%$) quoted for this rare gas in Ref. [28].

In the sudden approximation approach, the atomic excitation is treated separately from the initial vacancy production to which no reference is required except that the resulting change in the atomic potential due to the alteration in electron screening must be fast enough. From a study of the double ionization induced in Ne and Ti targets bombarded by photons and electrons, Krause [29] found that the breakdown point of the sudden approximation appears to occur at

$$h_{KL} = \frac{E_{ph,e} - B_K - B_L}{B_L} \approx 10, \quad (18)$$

where the numerator represents the excess energy of the incident particle ($E_{ph,e}$) over the ionization energy of the K -shell electron (B_K) plus the ionization energy of the shaken L electron (B_L) which refers to an ion with a hole in the K shell. The values of the parameter h_{KL} corresponding to the photoionization processes studied in the present paper are presented in Table I. They are all much bigger than 10. A comparison of our experimental results with sudden approximation predictions is thus meaningful. In particular, the average bremsstrahlung energy used for the Na $K^{(1)}L^{(1)}$ double excitation lies far above the break point of the sudden approximation and cannot therefore account for the observed discrepancy.

The x-ray yield ratios $KaL^{(1)}:KaL^{(0)}$ quoted in the last column of Table II were obtained mainly from electron bombardment and thus cannot be compared directly to our results. In the electron case, there is indeed a significant contribution to the $K^{(1)}L^{(1)}$ double ionization which arises from the simultaneous direct Coulomb excitation of two electrons by the charged projectile. As shown in Table II for Mg, which was measured earlier by means of both photon [32] and electron bombardment [30], one can see that the photon excitation gives a result which is smaller than the one corresponding to the electron excitation. In this context it is intriguing to note that the result of an earlier measurement concerning sodium [31], which was performed with 6 keV electrons, is smaller than our result obtained by photoionization. No explanation was found for this observation. For Mg, there is a discrepancy between our result and the

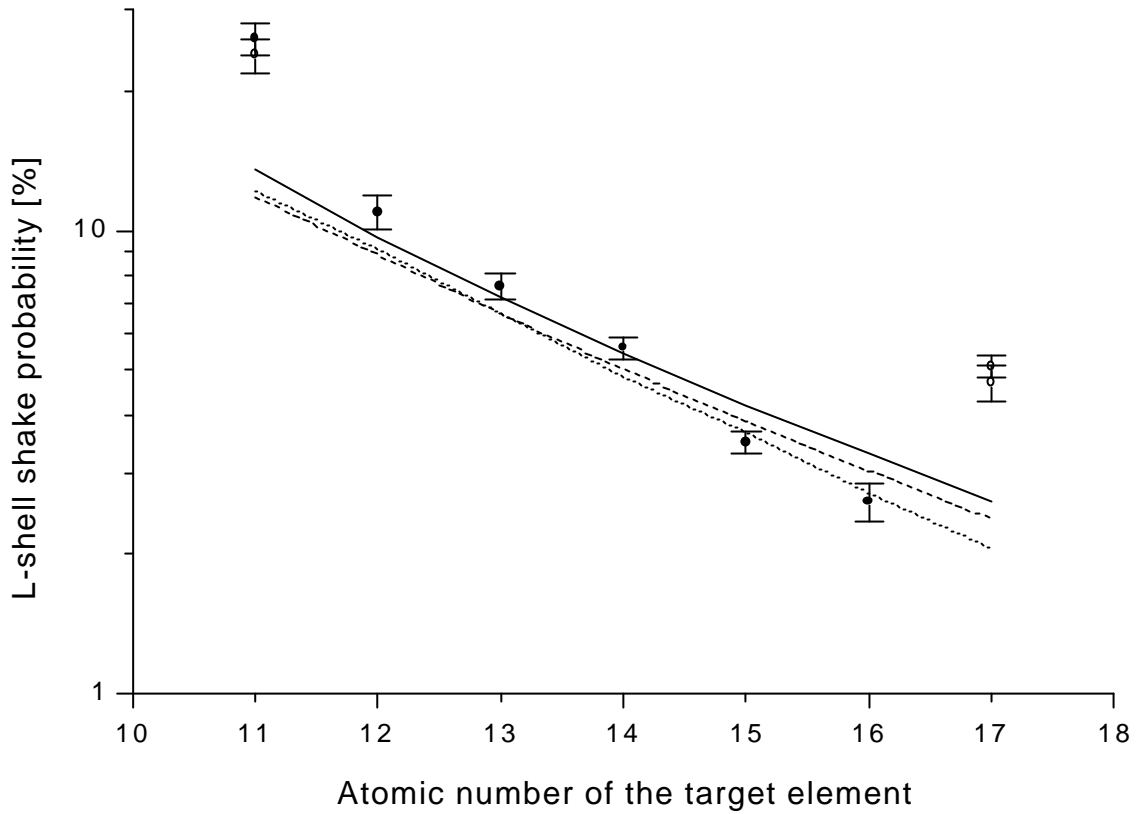


Fig 3. Total L -shell shake probabilities. Results corresponding to elemental targets are represented by full circles (), those obtained with compound targets by open circles (). The solid and dotted lines represent the results of our MCDF calculations performed with the Dyall's and Desclaux's codes, respectively, while the dashed line corresponds to theoretical predictions by Mukoyama [9].

one quoted in Ref. [32]. This discrepancy cannot be explained by the difference of the target thickness (0.01 mm in the present work, 4.0 mm in [32]) because in both experiments the x-ray yields were corrected for the self-absorption effect. Although there is no information about the data analysis in Ref. [32], we believe that the reason of the discrepancy resides in the interpretation of the observed satellite structures. We have indeed fitted the excess of intensity observed around 1256 eV with one Lorentzian (see Fig. 2, inset of the Mg spectrum) which was attributed to M satellites according to MCDF predictions. If this Lorentzian is included in the L -satellite components, our

$KaL^{(1)}$: $KaL^{(0)}$ yield ratio increases to a value which is consistent with the result quoted in [32].

As mentioned above, the satellite intensities are sensitive to the crystal environment of the atoms and ions. This statement is supported by numerous experimental results. For instance, Baun and Fisher [34] have shown that an important change in the Ka_4 to Ka_3 yield ratio and in the total peak intensity of the L satellites occurs in magnesium, aluminum, and silicon when these elements oxidize. Similar observations were done for the M satellites of heavier elements. For example, measurements of the Cl $Kb_{1,3}$ spectra in the chlorides [35] evinced fluctuations in the M satellite yields up to a factor

of 1.4. In addition, it was found by Kawai [36-38] that in chlorides the relative *M*-satellite intensity decreases almost linearly with the electronegativity of the element involved in the compound. Actually, a large electronegativity of the compound element indicates that the *3p* electrons of chlorine are partly delocalized or that the bonding in the chloride is predominantly covalent. This delocalization leads to a diminution of the electronic screening in the chlorine atoms, i.e., to an enhancement of the effective binding energy of the electrons, which in turn results in a decrease of the *M*- and *L*-shell shake probabilities. If the electronegativity is on the contrary small, the bonding character is predominantly ionic, i.e., the Cl *3p* electrons are more localized and, as a consequence, the shake probabilities are increased. Rubidium and sodium have an electronegativity of 0.8 and 0.9, respectively, which are both small with respect to that of chlorine (3.0). As expected the shake probabilities of Cl observed with the RbCl ($5.1\% \pm 0.3\%$) and NaCl ($4.7\% \pm 0.4\%$) targets are similar but both higher than the one predicted by theory for the pure element [the three theoretical predictions for chlorine are 2.6% (Dyall code), 2.1% (Desclaux code), and 2.4% (Mukoyama)]. The ionic character of NaCl which leads to an increase of the shake probability of Cl has the opposite influence on the shake probability of Na. Due to the delocalization of the *3s* electron of Na, the electronic screening in the sodium atoms embedded in the NaCl crystal diminishes, which leads to an increase of the binding energies of the *2s* and *2p* electrons, i.e., to the observed decrease of the *L*-shell shake

probability from $26\% \pm 2\%$ (Na) to $24\% \pm 2\%$ (NaCl).

Solid state and chemical effects are also expected to modify slightly the energies and transition probabilities of the components pertaining to the same satellite. As a consequence, the line shapes of the observed satellites and in particular the $K\alpha_4 : K\alpha_3$ yield ratios must reflect the influence of the neighbor atoms or ions. As shown in Table II, the $K\alpha_4$ to $K\alpha_3$ yield ratios found in the present study for pure elemental targets decrease first from 0.85 (Na) to 0.38 (Al) and then increase again up to 0.94 (S). A quadratic polynomial interpolation of the six ratios obtained for the elements Na to S results for pure Cl in a value of about 1.4 which is indeed quite different than the values obtained from the fits of the Cl spectrum corresponding to the NaCl target (value of 2.1) and RbCl target (value of 5.5). Similarly, the $K\alpha_4$ to $K\alpha_3$ yield ratio obtained from the analysis of the Na spectrum measured with the NaCl target is larger (1.0) than the one deduced from the measurement with the pure Na target (0.85). A qualitative interpretation of these findings is, however, far beyond the objectives of the present study and needs further and more detailed theoretical investigations.

ACKNOWLEDGMENTS

This work was partly supported by the Swiss National Science Foundation and the Polish Committee for Scientific Research (KBN), Grant No. PO3B 019 16.

- [1] J.-Cl. Dousse and J. Hozowska, Phys. Rev. A **56**, 4517 (1997).
- [2] T. Åberg, Phys. Rev. **156**, 35 (1967).
- [3] T.A. Carlson and M.O. Krause, Phys. Rev. A **140**, 1057 (1965).
- [4] T.A. Carlson and C.W. Nestor, Jr., Phys. Rev. A **8**, 2887 (1973).
- [5] J. Hozowska, J.-Cl. Dousse, J. Kern, and Ch. Rhême, Nucl. Instrum. Methods Phys. Res. A **376**, 129 (1996).
- [6] A. Mühleisen, M. Budnar, J.-Cl. Dousse, J. Hozowska, and Z.G. Zhao, X-Ray Spectrom. **27**, 337 (1998).
- [7] P.-A. Raboud, J.-Cl. Dousse, J. Hozowska, and I. Savoy, Phys. Rev. A **61**, 012507 (2000).
- [8] J.A. Bearden, Rev. Mod. Phys. **39**, 78 (1967).
- [9] T. Mukoyama and K. Taniguchi, Phys. Rev. A **36**, 693 (1987).
- [10] T.A. Carlson, W.E. Moddeman, and M.O. Krause, Phys. Rev. A **1**, 1406 (1970).
- [11] M.O. Krause and T.A. Carlson, Phys. Rev. **158**, 18 (1967).
- [12] V.P. Sachenko and E.V. Burtsev, Izv. Akad. Nauk SSSR, Ser. Fiz. 965 (1967) [Bull. Acad. Sci. USSR, Phys. Ser. **31**, 980 (1968)].
- [13] J.P. Desclaux, Comput. Phys. Commun. **9**, 31 (1975).
- [14] J.P. Desclaux, *Relativistic Multiconfiguration Dirac-Fock Package* (STEF, Cagliari, 1993), Vol. A.
- [15] P. Indelicato, Phys. Rev. Lett. **77**, 3323 (1996).
- [16] I.P. Grant, H.M. Quiney, Adv. At. Mol. Phys. **23**, 37 (1988).
- [17] P. Indelicato, Phys. Rev. A **51**, 1132 (1995).
- [18] K.G. Dyall *et al.*, Comput. Phys. Commun. **55**, 425 (1989).
- [19] F. James and M. Roos, Comput. Phys. Commun. **10**, 343 (1975).
- [20] M. Polasik, Phys. Rev. A **52**, 227 (1995).
- [21] E. Storm and H.I. Israel, Nucl. Data Tables **7**, 565 (1970).
- [22] Ch. Herren and J.-Cl. Dousse, Phys. Rev. A **56**, 2750 (1997) and references therein.
- [23] F.P. Larkins, At. Data Nucl. Data Tables **20**, 313 (1977).
- [24] E.J. McGuire, Phys. Rev. A **3**, 587 (1971).
- [25] J.L. Campbell, T. Papp, X-Ray Spectrom. **24**, 307 (1995).
- [26] M.O. Krause and J.H. Oliver, J. Phys. Chem. Ref. Data **8**, 307 (1979).
- [27] T.W. Tunnel and C.P. Bhalla, Phys. Lett. **86A**, 13 (1981).
- [28] R.E. LaVilla, Phys. Rev. A **4**, 476 (1971).
- [29] M.O. Krause, J. Phys. (Paris), Colloq. **10 32**, C4-67 (1971).
- [30] E. Mikkola, O. Keski-Rakkonen, J. Lahtinen, and K. Reinikainen, Phys. Scr. **28**, 188 (1983).
- [31] O. Keski-Rahkonen, K. Reinikainen, and E. Mikkola, Phys. Scr. **28**, 179 (1983).
- [32] K. Parthasaradhi *et al.* Nucl. Instrum. Methods Phys. Res. A **255**, 54 (1987).
- [33] S.N. Soni, J. Phys. B **31**, 1695 (1998).
- [34] W.L. Baun and D.W. Fisher, in *Advances in X-Ray Analysis*, edited by W.M. Mueller, G.R. Mallet, and M.J. Fay (Plenum Press, Inc., New York, 1965), Vol. 8, p. 371.
- [35] E.E. Vainshtein, L.N. Mazalov, and V.G. Zyryanov, Fiz. Tverd Tela (Leningrad) **7**, 1099 (1965) [Sov. Phys. Solid State **7**, 882 (1965)].
- [36] J. Kawai, C. Satoko, K. Fujisawa, and Y. Gohshi, Phys. Rev. Lett. **57**, 988 (1986).
- [37] J. Kawai, C. Satoko, K. Fujisawa, and Y. Gohshi, Spectrochim. Acta, Part B **42B**, 729 (1987).
- [38] J. Kawai, C. Satoko, and Y. Gohshi, Spectrochim. Acta, Part B **42B**, 745 (1987).

Part II

Double KL shell ionization in Al, Ca, and Co targets bombarded by low-energy electrons

O. Mauron and J.-Cl. Dousse

Department of Physics, University of Fribourg, Chemin du Musée 3, CH-1700 Fribourg, Switzerland

(Received 28 May 2002; published 22 October 2002)

The cross sections for the production of double KL vacancy states in Al, Ca, and Co as a result of electron bombardment were determined for impact energies ranging from the double excitation threshold up to 20 keV. The cross sections were derived from the measured intensity ratios $I_{KL^{(1)}} : I_{KL^{(0)}}$ of the satellite-to-parent-diagram x-ray lines. The specific contributions of the shake and two-step electron-electron processes could be probed by comparing the relative satellite yields observed in the electron-induced spectra to those obtained by photoionization. In particular the energy-dependent cross sections for double KL excitation resulting from two-step-two processes could be deduced. The measurements were performed by means of high-resolution x-ray spectroscopy, using a reflection-type bent crystal spectrometer.

PACS number(s): 32.80.Fb, 32.30.Rj, 34.50.Fa, 34.80.Dp

I. INTRODUCTION

Cross-section measurements of inner-shell ionization induced by electron impact have been performed during the last decade for a variety of atoms and ions [1-4], except in the case of multiple (double, triple,...) ionization, for which only a limited number of reports is available up to now. The double ionization of neutral atoms by electron bombardment may result from direct processes, consisting of the ejection of two electrons without any internal rearrangement of bound electrons, and indirect processes in which the ejection of a single inner-shell electron is followed by Auger decay. Only direct processes will be considered in this

paper, namely the shake process and the so-called two-step-one (TS1) and two-step-two (TS2) mechanisms [5].

The shake process is a one-step mechanism that results from a sudden change in the atomic potential [6,7]. The abrupt potential change may happen in inner-shell ionization where the electronic screening decreases suddenly, or in nuclear decay which leads to a quick change of the nuclear charge seen by the electrons. Shake probabilities do not depend, in first order, on the mechanism leading to the creation of the core vacancy. In a shake process an atomic electron can be ejected into the continuum

(shakeoff) or promoted to a higher unoccupied bound state (shakeup).

Direct double inner-shell ionization may also result from two-step electron-electron collisions. Depending on the origin of the incoming electron involved in the second collision, the mechanism is named TS1 or TS2 [8-12]. In the TS1 process the *d*-electron ejected as a result of the first interaction collides with another bound electron which in turn is kicked out so that a double vacancy state is created in the target atom. In the TS2 process the second vacancy is produced by the same electron as the first one. In this case the incoming electron is thus assumed to interact sequentially with two electrons pertaining to the same target atom.

In this paper we report on results concerning the double *KL* shell ionization induced in metallic Al, Ca, and Co by impact with low-energy electrons. The experimental method consisted in measuring the *K* x-ray emission of the targets with a high-resolution bent crystal spectrometer. The x-ray satellite lines $KaL^{(1)}$ (i.e., the $1s-2p$ transitions with one additional spectator vacancy in the *L* shell) could be resolved from the parent diagram lines $KaL^{(0)}$ and their intensities determined. The cross sections S_{KL} for double *KL* shell ionization were derived from the observed satellite-to-diagram line yield ratios $I_{KaL^{(1)}} : I_{KaL^{(0)}}$ and the single *K*-shell ionization cross sections S_K reported in the literature [2]. For each target, the *K* x-ray emission was measured for several impact energies ranging from the *KL* double excitation threshold up to 20 keV. Furthermore, as satellites observed in *K* x-ray spectra produced by photoionization can be assumed to result quasi-exclusively from shake and TS1 processes, we were able to determine the cross

section for the TS2 process as a function of the excitation energy by comparing the relative yields of the *L* satellites observed in the electron-induced and photoinduced x-ray spectra.

Many experiments concerning electron-induced double ionization were carried out using the (e,3e) coincidence technique [10-15]. This method in which all three final electrons are simultaneously analyzed, both in direction and energy, provides fivefold differential cross sections from which total double ionization cross sections are, however, difficult to extract. Results of the present study may thus be regarded as complementary to those obtained in (e,3e) measurements.



Fig 1. Photograph of the Von Hamos spectrometer. The three circular ports on the top part of the spectrometer chamber permit access to the target, crystal, and CCD detector. The vertical device on the target port is the 100 kV x-ray tube. Also visible at the bottom of the photograph, on the right, is the 20 kV electron gun mounted horizontally on one of the four beam ports.

II. EXPERIMENT

A. Experimental method

As the radiative decay of multivacancy states gives rise to satellite x-ray lines, multiple inner-shell ionization cross sections can be deduced from the measured intensities of the satellites provided the latter are well separated from neighboring spectral lines, which requires one to use high-resolution instruments. Similarly, multiple to single ionization cross section ratios and ionization probabilities concerning the shells in which the spectator vacancies are located can be determined from the observed ratios of the satellite-to-diagram line yields. This technique has been exploited intensively in the past years for studying the multiple inner-shell ionization induced in a variety of target elements by impact with photons [16-18], protons [19,20], α particles [21-23], heavy ions [24-27] and, to a smaller extent, electrons [28]. In most experiments performed with this method, K x-ray spectra were measured, more rarely L and M x-ray spectra [29,30]. Depending on the energy of the x-ray spectra, Laue-type or Bragg-type bent crystal spectrometers were employed. Finally, it can be mentioned that this satellite technique has been also used in high-resolution Auger [31] and photo-electron spectroscopy [32].

In the present study the double KL shell ionization was investigated by measuring the $KaL^{(1)}$ satellite x-ray emission of the targets. The central energies of the $KaL^{(1)}$ spectra of Al, Ca, and Co being 1490, 3700, and 6950 eV, respectively, a Bragg-type bent crystal spectrometer was employed. For each target, the full widths at half maximum of the satellite and diagram transitions were found to

be several times smaller than the energy separation between the two lines so that the satellite structures could be well resolved and their intensities accurately determined. As intra-atomic rearrangement processes such as L Auger and L radiative transitions occurring prior to the K x-ray emission diminish significantly the number of L spectator vacancies, the measured relative yields x_L of the satellites were corrected by a simple statistical procedure (see Sec. III). The corrected yields i_L represent the relative number of two-hole states KL with respect to single-hole states KL^0 as originally induced by the electron bombardment. The ratio of the double to single ionization cross section is thus equal to the initial L vacancy yield i_L :

$$\frac{\mathbf{S}_{KL}}{\mathbf{S}_{KL^{(0)}}} = i_L \quad (1)$$

The electron-induced K -shell ionization cross sections \mathbf{S}_K reported in the literature [1,2] were determined using low-resolution semiconductor detectors. The yields of the unresolved satellites are thus included in the measured x-ray yields used to derive the quoted cross sections, so that

$$\mathbf{S}_K = \mathbf{S}_{KL^{(0)}} + \mathbf{S}_{KL}. \quad (2)$$

In Eq. (2) it was implicitly assumed that higher-order $KL^{(2)}$, $KL^{(3)}$, ... satellites have negligibly small intensities, which is a reasonable assumption in the case of electron impact induced ionization. Using the two above relations, the double ionization cross sections \mathbf{S}_{KL} can be determined from the measured vacancy yields i_L and the known single ionization cross sections \mathbf{S}_K :

$$\mathbf{S}_{KL} = \frac{i_L}{1 + a \cdot i_L} \mathbf{S}_K, \quad (3)$$

where \mathbf{a} is a correction factor accounting for the differences in the average energies of the electrons producing the single and double ionization (see Sec. II B).

Furthermore, assuming that the amplitudes describing the interference between the three mechanisms discussed in Sec. I may be neglected, the electron-induced *KL* double ionization cross section can be written as:

$$\mathbf{S}_{KL} = \mathbf{S}_{KL^{(0)}} \cdot (P_L^{shake} + P_L^{TS1}) + \mathbf{S}_{TS2} + \mathbf{S}_{K^{(0)}L} \cdot (P_K^{shake} + P_K^{TS1}) \quad (4)$$

where $P_{K,L}^{shake,TS1}$ are the probabilities to produce a *K* or *L* shell spectator vacancy by a shake or TS1 process.

Although the cross section $\mathbf{S}_{K^{(0)}L}$ is about two orders of magnitude bigger than $\mathbf{S}_{KL^{(0)}}$, the third term in Eq. (4) can be neglected because the probability of creating via shake and TS1 processes 1s vacancies as a result of *L*-shell ionization is extremely small. Assuming in addition that for equal excitation energies the probabilities for *L*-shell ionization via shake and TS1 processes are approximately the same in the electron and photon target bombardments, one can write

$$P_L^{shake} + P_L^{TS1} = P_L^{photo}, \quad (5)$$

where P_L^{photo} stands for the total shake + TS1 probability to ionize one *L* electron from the target atom as a result of 1s photoionization.

Using above assumptions and relations (1), (2), and (4), the following expression is found for the cross section \mathbf{S}_{TS2} :

$$\mathbf{S}_{TS2} = \frac{i_L - \frac{P_L^{photo}}{a}}{1 + a \cdot i_L} \mathbf{S}_K. \quad (6)$$

The probabilities P_L^{photo} were derived from the corrected satellite yields i_L^{photo} observed in the photoinduced *Ka* x-ray spectra, using the formula given in [33]:

$$P_L^{photo} = \frac{8^8 \cdot i_L^{photo}}{(8 + i_L^{photo})^8}. \quad (7)$$

B. Measurements with electrons

For the electron bombardment of the targets, an energy tunable (500 eV-20 keV) electron gun with electrostatic focusing and deflection was used. The gun was equipped with a standard cathode firing unit allowing beam intensities up to 100 μ A. It was mounted horizontally and fixed to the 30° beam port of the spectrometer with a rotatable 2¾-in. flange (see Fig. 1), so that the angle between the direction of the electron beam and the normal to the target surface was $\pi/6$. In the Von Hamos slit geometry the shape of the measured spectra can be altered by the beam intensity profile if the latter is inhomogeneous. For this reason, the profile of the electron beam intensity at the target position was determined for each measurement and the spectra, if necessary, were corrected off-line to account for the measured inhomogeneities. Furthermore, in order to make these corrections as small as possible, broad beam profiles were employed.

Ten different electron energies, ranging from the double *KL* excitation threshold up to 20 keV, were chosen for each target. The precision of the set voltages was 5 V and the energy spread of the electron beams smaller than 0.5 eV. Depending on

the target and beam energy, intensities comprised between 50 and 100 **mA** were used. As the range of low-energy electrons in solids is extremely small, all beams were stopped in the targets. The cross sections determined in our experiment correspond thus to average electron energies. The latter were determined using the following relation:

$$E_{K,KL} = \frac{\int_0^{h_{K,KL}} E \cdot \mathbf{s}_{K,KL}(E(x)) \cdot \exp\left[-\mathbf{m} \frac{x}{\sin(\mathbf{q})}\right] dx}{\int_0^{h_{K,KL}} \mathbf{s}_{K,KL}(E(x)) \cdot \exp\left[-\mathbf{m} \frac{x}{\sin(\mathbf{q})}\right] dx}, \quad (8)$$

where E_K and E_{KL} represent the average energies of the electrons that produce in the target single K -vacancies and double KL -vacancies, respectively, \mathbf{s}_K and \mathbf{s}_{KL} the corresponding cross sections, \mathbf{m} and \mathbf{q} the mass attenuation coefficient and Bragg angle for the considered x-ray transition and target, and x the projectile penetration depth projected on the axis perpendicular to the target surface. The coefficients \mathbf{m} were taken from [34].

The stopping power can be written as

$$\begin{aligned} \frac{dE}{ds} &= -c \cdot E^{-n} \\ \Rightarrow E^n \cdot dE &= -c \cdot ds = -c \cdot \frac{dx}{\cos(\mathbf{p}/6)} \end{aligned} \quad (9)$$

The coefficients c and \mathbf{n} were derived from the stopping power values quoted in [35]. The function $E(x)$ was found from the integration of Eq. (9):

$$E(x) = \left[E_e^{n+1} - (\mathbf{n}+1) \cdot c \cdot \frac{x}{\cos(\mathbf{p}/6)} \right]^{\frac{1}{n+1}}. \quad (10)$$

In Eq. (10) E_e stands for the initial energy of the incoming electrons. The distances h_K and h_{KL}

occurring in Eq. (8) represent the penetration depths at which the electron energy is equal to the single ionization threshold energy $E_{thr,K}$ and the double ionization threshold energy $E_{thr,KL}$, respectively. These distances can be deduced from Eq. (10):

$$h_{K,KL} = \frac{(E_e^{n+1} - E_{thr,K,KL}^{n+1}) \cdot \cos(\mathbf{p}/6)}{(\mathbf{n}+1) \cdot c}. \quad (11)$$

For each target, the function $\mathbf{s}_K(E)$ was determined by means of a least-squares-fit method, employing a function similar to the one proposed by Gryzinski [36] to fit the experimental cross sections reported in [2]. The so-determined function $\mathbf{s}_K(E)$ permitted us to compute then the average energies E_K .

For a given target and electron-beam energy E_e the correction factor \mathbf{a} appearing in formulas (3) and (6) is defined by

$$\mathbf{a} = \frac{\mathbf{s}_K(E_{KL})}{\mathbf{s}_K(E_K)}. \quad (12)$$

According to Eq. (3), the computation of the experimental cross sections \mathbf{s}_{KL} needed for the determination of the function $\mathbf{s}_{KL}(E)$ requires the knowledge of the coefficients \mathbf{a} , whose determination, as indicated by Eq. (12), is not possible without the knowledge of the average energies E_{KL} . As the calculation of the latter, in turn, requires the function $\mathbf{s}_{KL}(E)$ to be known, the least-squares-fit approach employed to determine $\mathbf{s}_K(E)$ could not be applied directly to the determination of the function $\mathbf{s}_{KL}(E)$. The difficulty was circumvented by applying the least-squares-fit method iteratively, using in the first iteration the approximations $E_{KL}^{(1)} \cong E_K$ and $\mathbf{a}^{(1)} \cong 1$. The function $\mathbf{s}_{KL}^{(n)}(E)$ corresponding to the

n th-iteration was obtained by fitting the Gryzinski-like function to the cross sections $\mathbf{s}_{KL}^{(n-1)}(E_{KL}^{(n-1)})$ computed in the preceding iteration. The function $\mathbf{s}_{KL}(E)$ resulting from the fit served then to compute the values $E_{KL}^{(n)}$, $\mathbf{a}^{(n)}$ and $\mathbf{s}_{KL}^{(n)}(E_{KL}^{(n)})$ employed in the next iteration. The method was found to be self-consistent. In other words, after a certain number of iterations (5-10, depending on the target and electron-beam energy) the energies E_{KL} were found to remain unchanged. The iterations were stopped when the change in E_{KL} became smaller than 1 eV.

C. Photoionization measurements

The fluorescence x-ray spectra were produced by irradiating the targets with the bremsstrahlung of a Coolidge x-ray tube with a Cr anode and a 0.5-mm-thick Be window. The x-ray lamp was mounted so that the ionizing radiation was perpendicular to the surface of the targets. The tube was supplied with a 100 kV/3 kW high voltage (HV) generator equipped with a dedicated system for the stabilization of the current and high voltage. The experimental settings employed for the photoionization measurements are summarized for each target in Table I.

The average energy of the bremsstrahlung was determined using the following formula:

$$E_{photo} = \frac{\int_0^{E_{max}} \int_0^h E \cdot I(E) \cdot \exp[-\mathbf{m}(E) \cdot x] \cdot \mathbf{s}_{photo}(E) \cdot \exp\left[-\mathbf{m}(E_{Ka}) \cdot \frac{x}{\sin(q)}\right] dx dE}{\int_0^{E_{max}} \int_0^h I(E) \cdot \exp[-\mathbf{m}(E) \cdot x] \cdot \mathbf{s}_{photo}(E) \cdot \exp\left[-\mathbf{m}(E_{Ka}) \cdot \frac{x}{\sin(q)}\right] dx dE} \quad (13)$$

where \mathbf{m} is the mass absorption coefficient of the target, \mathbf{s}_{photo} the photoelectric cross section for the K -shell of the target element, q the Bragg angle, h the target thickness and $E_{max} = e \cdot HV_{tube} \cdot I(E)$ represents the spectral response of the x-ray tube. The latter was measured with a Si(Li) detector. The functions $\mathbf{m}(E)$ and $\mathbf{s}_{photo}(E)$ were derived from the values quoted in [34]. The calculated average energies are presented in Table I.

D. Crystal spectrometer

The measurements were performed at the University of Fribourg by means of a reflecting type Von Hamos curved crystal spectrometer [37]. The main characteristics of this instrument were already presented in several previous articles [17,38,39]. Thus, in the following, only the features specific to the setup used for the present experiment will be discussed.

The principal elements of the spectrometer are an x-ray source defined by a rectangular slit, a

Table I. *Experimental settings employed in the photoionization measurements.*

| Element | X-ray tube | Crystal | Reflection order | E_{photo} [keV] |
|---------|-------------|----------------------------------|------------------|-------------------|
| Al | 30 kV 10 mA | ADP (101) | 1 | 6.5 |
| Ca | 60 kV 10 mA | ADP (101) | 2 | 11.3 |
| Co | 90 kV 10 mA | SiO ₂ ($2\bar{2}3$) | 1 | 16.5 |

cylindrically bent crystal, and a position sensitive detector. The vertical rectangular slit consisted of two juxtaposed Ta pieces 0.3 mm thick and 10 mm high. For all measurements a slit width of 0.2 mm was used. For the Al and Ca measurements, the spectrometer was equipped with a 5-cm-wide x 10-cm-high x 0.3-mm-thick (101) ADP crystal ($2d=10.642 \text{ \AA}$). For Co a $(\bar{2}\bar{2}3)$ SiO_2 crystal ($2d=2.7500 \text{ \AA}$) was employed. Both crystals were curved cylindrically to a radius of 25.4 cm. The Al and Co spectra were measured in first order of reflection, the Ca spectrum in second order. The diffracted x-rays were recorded with a 27.65-mm-long and 6.9-mm-high charge coupled device (CCD) position sensitive detector, having a depletion depth of 50 μm . The 27 μm pixel resolution of the CCD being many times better than the natural linewidth of the observed transitions, a software binning of four columns was performed in order to obtain higher count rates in the position spectra. The position spectra were calibrated in energy by means of the formulas (3) and (4) given in [37], using the $K\alpha_1$ energies quoted by Bearden [40].

E. Targets

The Al and Co targets consisted of thin metallic foils, 0.01 and 0.02 mm thick, respectively. The Ca targets were prepared by rolling carefully granules until foils with a thickness of about 0.1 mm were attained. The chemical purity of the targets was 99.9% for Co and 99.0% for Al and Ca. Since with the Von Hamos spectrometer the installation of the samples on the target holder cannot be made in vacuum, no treatment of the target surfaces was performed before irradiation. The 20-mm-high x 5-mm-wide rectangular foils were mounted on Al

frames. During the electron and photon irradiation, the pressure in the vacuum chamber of the spectrometer was about 10^{-6} - 10^{-7} mbar.

Despite this high-vacuum, chemical reactions in the targets were observed as a result of the electron irradiation. Black dots coinciding in position with the beam spot could be indeed seen on the surface of the targets already after a few hours of irradiation. It was found that the change in the surface appearance was growing with the time during which the target was exposed to the electron beam. The effect was particularly pronounced in the case of Al. In contrast to that, no surface damage could be observed when irradiating the targets with the x-ray tube bremsstrahlung.

The time dependent modification of the target surface had a double effect on the electron measurements. First, it was found that for the lower energy electron beams the total intensity of the target x-ray emission was decreasing with time as if the damaged surface were acting as a dead layer. The second effect concerns the satellite shape which was found to slightly change with time. In particular we noticed some variation in the yield ratio of the $K\alpha_4$ to $K\alpha_3$ satellite components. Actually a similar observation was done for Al and Mg in former studies [41,42]. For these reasons, the targets were replaced frequently and periodic tests of the x-ray spectrum intensity and satellite shape were performed. As soon as a statistically significant change was detected, a new target was installed so that, in our opinion, the reliability of the obtained results was not really affected by these radiation damages.

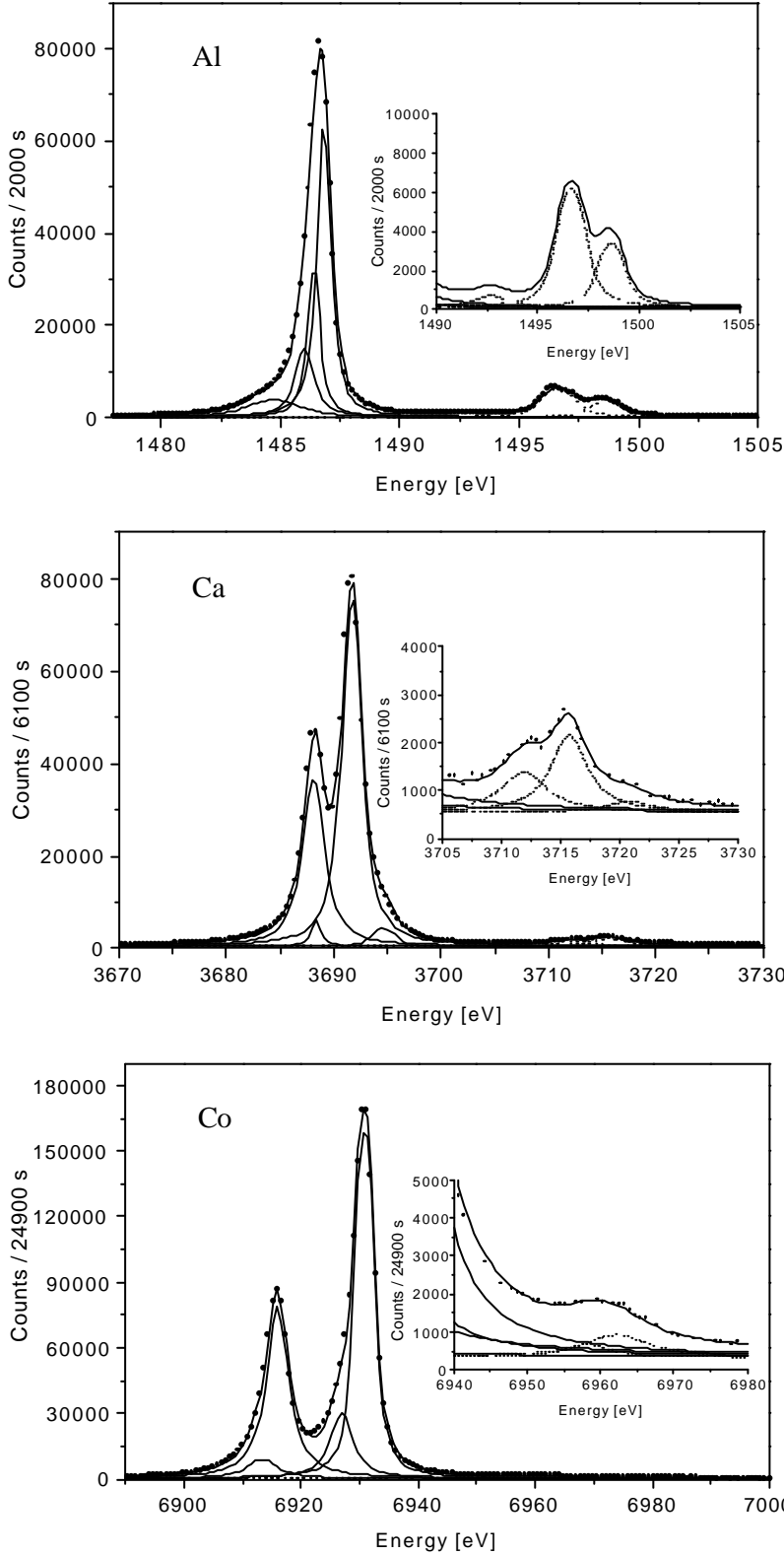


Fig 2. High-resolution $K\alpha$ x-ray spectra of Al, Ca, and Co resulting from 15 keV electron bombardment. The $K\alpha L^{(i)}$ satellite structures of interest are shown enlarged in the insets. The thin solid lines represent the components employed to fit the $K\alpha_{1,2}$ diagram lines and unresolved M satellites, the dotted ones correspond to the Lorentzians used to fit the L satellites and the thick solid lines stand for the total fits.

III. DATA ANALYSIS

The method of data analysis applied in the present study is essentially the same as that used in

[18]. Therefore fitting procedure and corrections for electron rearrangement will be only briefly described here. The observed K x-ray spectra were analyzed by means of the least-squares fitting

computer program MINUIT [43], employing Voigt and Lorentz functions to fit the diagram and satellite lines. In order to reproduce as well as possible the shape of the complex structures corresponding to the satellite and diagram lines, most parameters were let free in the fitting procedure. As satellite lines consist of many overlapping components, their complex shape was reproduced by several juxtaposed Lorentzians. The same held for the diagram transitions for which asymmetric shapes were observed resulting from unresolved M -satellite structures and, especially for aluminum, from open valence subshells in the ground state [18]. Voigt functions, however, were preferred to fit the diagram lines because the tails of the latter were found to be better reproduced by Voigt functions.

To illustrate the method used for the data analysis, the fitted $KaL^{(0,1)}$ x-ray spectra of Al, Ca, and Co resulting from 15 keV electron bombardment are presented in Fig. 2. For Co the first group of lines centered around 6920 eV corresponds to the Ka_1 and Ka_2 diagram transitions which were fitted with a single Voigt function each. The intensity ratio $I(Ka_2):I(Ka_1)$ and the energy difference $E(Ka_1) - E(Ka_2)$ were kept fixed in the fitting procedure at the values of 0.51 and 15.02 eV quoted in

Refs. [34] and [40], respectively. In order to fit correctly the observed asymmetries two additional Voigt functions of lower intensity were included in the fit of the diagram lines. These asymmetries originate probably from low energy components of the $Ka_{1,2}M^{(1)}$ satellites. They cannot indeed be attributed to $K-LM$ radiative Auger (RAE) transitions [38,44] because the latter are expected to occur below 6862 eV (edge of the $K-L_3M_3^1P_1$ transition, the $K-LM$ RAE transition of highest energy as indicated by Larkin's tables [45]). All parameters of the two additional Voigt functions were let free in the fit. The L -satellite structure around 6960 eV, shown enlarged in the inset, was fitted with two Lorentz functions. Here again, all fitting parameters were let free. The $X_{KaL^{(1)}} : X_{KaL^{(0)}}$ yield ratio was computed by taking for $X_{KaL^{(0)}}$ the sum of the yields of the four Voigt functions represented by solid lines (diagram transitions and $KaM^{(1)}$) and for $X_{KaL^{(1)}}$ the sum of the yields of the two Lorentzians depicted with dotted lines ($KaL^{(1)}$ satellites, $KaL^{(1)}M^{(1)}$ components included). A quite similar analysis was performed for the two other investigated elements, Al and Ca.

Although the energy differences between the diagram and L -satellite lines are small (10-30 eV), the dependence on the photon energy of the x-ray absorption in the target, crystal reflectivity and solid

TABLE II: Weighting factors w_{L_i} , partial fluorescence yields $\mathbf{w}_{KaL^{(n)}}$, and rearrangement factors R_L .

| Element | w_{L_1} | w_{L_2} | w_{L_3} | $\mathbf{w}_{KaL^{(0)}}$ | $\mathbf{w}_{KaL^{(1)}}$ | R_L |
|---------|-----------|-----------|-----------|--------------------------|--------------------------|-------------|
| Al | 0.263 | 0.244 | 0.493 | 0.038 | 0.044 | 0.075 0.037 |
| Ca | 0.311 | 0.231 | 0.458 | 0.150 | 0.164 | 0.158 0.060 |
| Co | 0.308 | 0.230 | 0.462 | 0.343 | 0.362 | 0.245 0.065 |

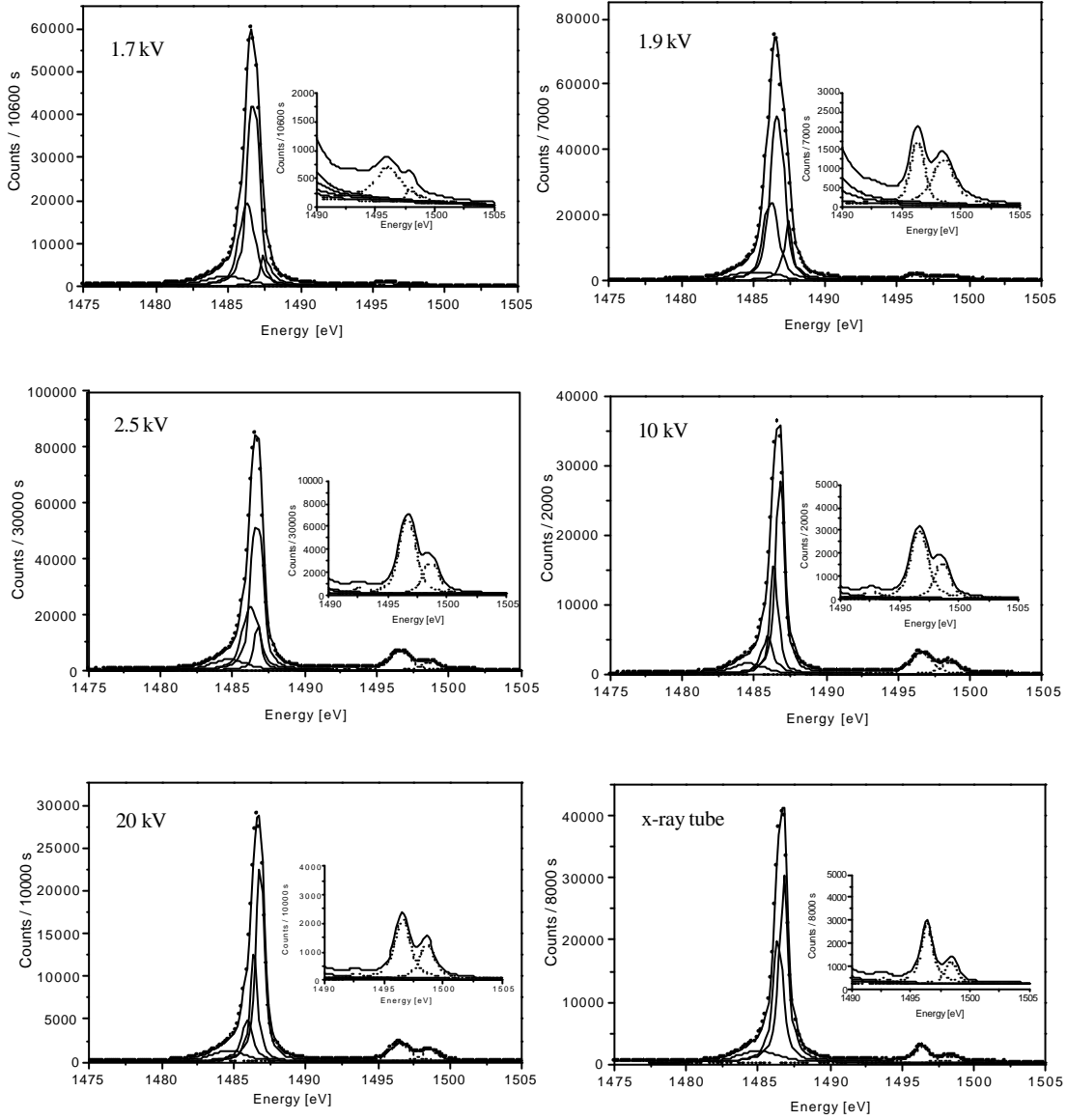


Fig 3: Evolution of the Al $KaL^{(1)}$ satellite yield and line shape as a function of the high-voltage of the electron gun. The corresponding spectrum produced by photoionization with the bremsstrahlung from a Cr x-ray tube (30 kV) is also shown for comparison.

angle of the spectrometer were probed and their effect on the $X_{KaL^{(1)}} : X_{KaL^{(0)}}$ x-ray yield ratios checked. No significant change was found.

As discussed in Sec. II A, the quantities that are relevant for the determination of the double ionization cross sections S_{KL} are not the satellite to diagram line x-ray yield ratios x_L extracted from the fitting procedure but the relative initial vacancy

yields i_L . As shown in the Appendix of Ref. [17], the vacancy yields i_L can, however, be derived from the x-ray yields x_L , using the following relation:

$$i_L = \frac{x_L \cdot \frac{W_{KaL^{(0)}}}{W_{KaL^{(1)}}}}{1 - R_L \left[1 + x_L \cdot \frac{W_{KaL^{(0)}}}{W_{KaL^{(1)}}} \right]}, \quad (14)$$

where $x_L = X_{KaL^{(1)}} : X_{KaL^{(0)}}$, $w_{KaL^{(n)}}$ corresponds to the partial fluorescence yield of the transition Ka with n spectator vacancies in the L -shell and R_L represents the total L -shell rearrangement factor. The latter was obtained from the weighted sum of the subshell rearrangement factors R_{Li} :

$$R_L = \sum_i R_{Li} = \sum_i w_{Li} \frac{\Gamma_{Li} - \sum_j \Gamma_{LiLjM}}{\Gamma_K + \Gamma_{Li}} \quad (15)$$

$$= \sum_i w_{Li} \frac{\Gamma_{Li}}{\Gamma_K + \Gamma_{Li}} \left(1 - \sum_j f_{ij} \right)$$

In Eq. (15), the coefficients w_{Li} represent the weighting factors of the subshells Li and the coefficients f_{ij} the relative Coster-Kronig yields. For the three elements investigated in this paper, L_2L_3M Coster-Kronig transitions are energetically forbidden so that only the coefficients f_{12} and f_{13} had to be considered. They were taken from Ref. [46]. For the level widths Γ_K and Γ_{Li} , the values reported recently by Campbell and Papp [47] were

employed. The weighting factors and partial fluorescence yields were determined using the same methods and the same references as those reported in [18]. The obtained results are presented in Table II together with the total L -shell rearrangement factors.

IV. RESULTS AND DISCUSSION

A. Satellite line shape

The evolution of the strength and the shape of the Al $KaL^{(1)}$ satellite spectrum is illustrated in Fig. 3 for five increasing bombarding energies. For comparison, the corresponding photoinduced spectrum is also presented. The satellite structures could be well reproduced with three juxtaposed Lorentzians. From the fits of the electron-induced spectra average centroid energies of 1492.8, 1496.5, and 1498.5 eV, respectively, were obtained for the three Lorentzians. Small deviations of about 0.5 eV

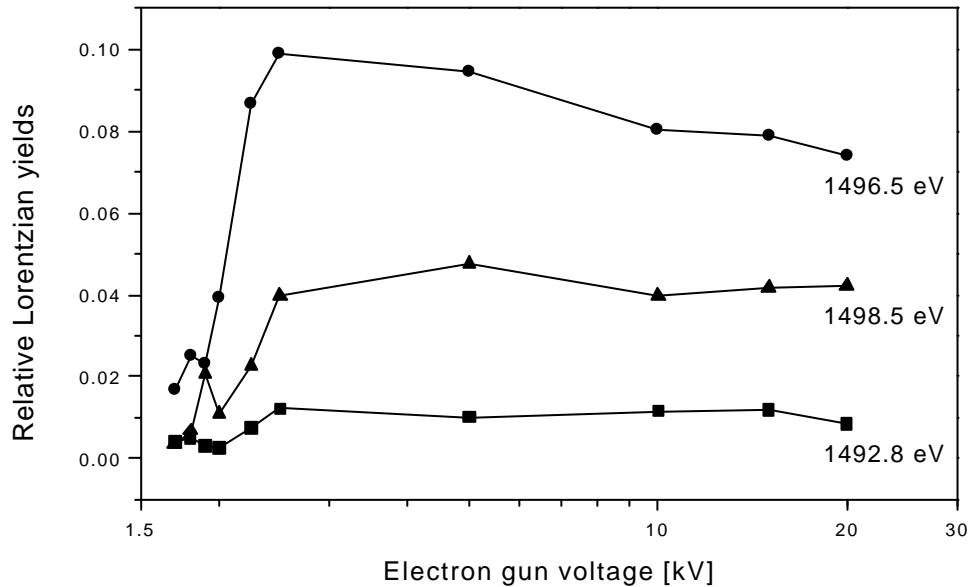


Fig 4: Relative intensities of the three Lorentzians employed to fit the $KaL^{(1)}$ satellite structure of Al for growing electron gun voltages. The three satellite components are labeled with their centroid energy.

were, however, observed for excitation energies close to the double ionization threshold. For the photoinduced spectrum, the fitted centroid energies were found to be approximately the same (1492.6, 1496.4, and 1498.4 eV). As shown in Fig. 3, the total satellite yield grows rapidly between 1.7 and 2.5 kV and remains almost constant between 2.5 and 20 kV. Similarly, the most pronounced changes in the satellite shape are observed below 2.5 kV. The visible diminution of the diagram line width with growing bombarding energy originates probably from the decrease of the simultaneous *M*-shell ionization. For the employed electron energies, the *M*-shell ionization due to shake processes is indeed nearly constant but the contribution to the *M*-shell ionization of TS2 processes decreases rapidly, the velocity of the incident electrons being large in the *M*-shell scale.

Since the *L* spectator vacancy can be located in three different subshells and because many different couplings between the *K* and *L* holes in the initial state and the two *L* holes in the final state are possible, $KaL^{(i)}$ x-ray satellite structures consist of numerous overlapping transitions that vary in energy and strength. As a result, the spectrum shape is in general complex, showing asymmetries and fine structures that cannot be reproduced by a single Lorentzian or Voigt function. Theoretical profiles can be constructed by computing by means of multiconfiguration Dirac-Fock (MCDF) calculations the energies and transition probabilities of all allowed transitions decaying the double-hole states, and subsequently attributing a Lorentzian shape to each component and finally adding together the so-obtained Lorentzians. In these simulations, the natural widths of the individual components can be determined from the total widths of the initial and

final states and the intensities of the components are given by the calculated transition probabilities. Examples of such simulations can be found in Ref. [18] and [33]. For Al the simulations show that the Lorentzian at 1492.6 eV is due predominantly to transitions decaying $1s^{-1}2s^{-1}$ states, the one at 1498.6 eV to transitions decaying $1s^{-1}2p^{-1}$ states whereas the strongest Lorentzian at 1496.6 eV corresponds to the radiative decay of both $1s^{-1}2s^{-1}$ and $1s^{-1}2p^{-1}$ states. The MCDF simulations indicate also that the shape of the satellite x-ray spectrum corresponding to the radiative decay of double-vacancy states populated by shakeup is approximately the same as the shape of the spectrum resulting from shakeoff. Thus the satellite technique employed in the present study does not allow one to distinguish clearly the shakeup process from the shakeoff and the TS1 and TS2 processes.

The dependence of the satellite line shape on the excitation energy is reflected in the relative intensities of the three Lorentzians employed to reproduce the satellite structure. The fitted relative yields of the three Lorentzians are presented in Fig. 4 as a function of the bombarding energy. One sees that the intensity of the first component is more or less constant at the beginning and starts to increase at slightly higher excitation energies than the two other components. This can be explained by the fact that, as mentioned above, the lowest energy Lorentzian consists predominantly of transitions decaying $1s^{-1}2s^{-1}$ double-hole states that are produced at higher excitation energies than $1s^{-1}2p^{-1}$ states. Due to the thickness of the employed Al target and the resulting energy spread of the electrons active in the double ionization, resonant-like excitation features are not expected to occur in the diagrams represented in Fig. 4. This statement is,

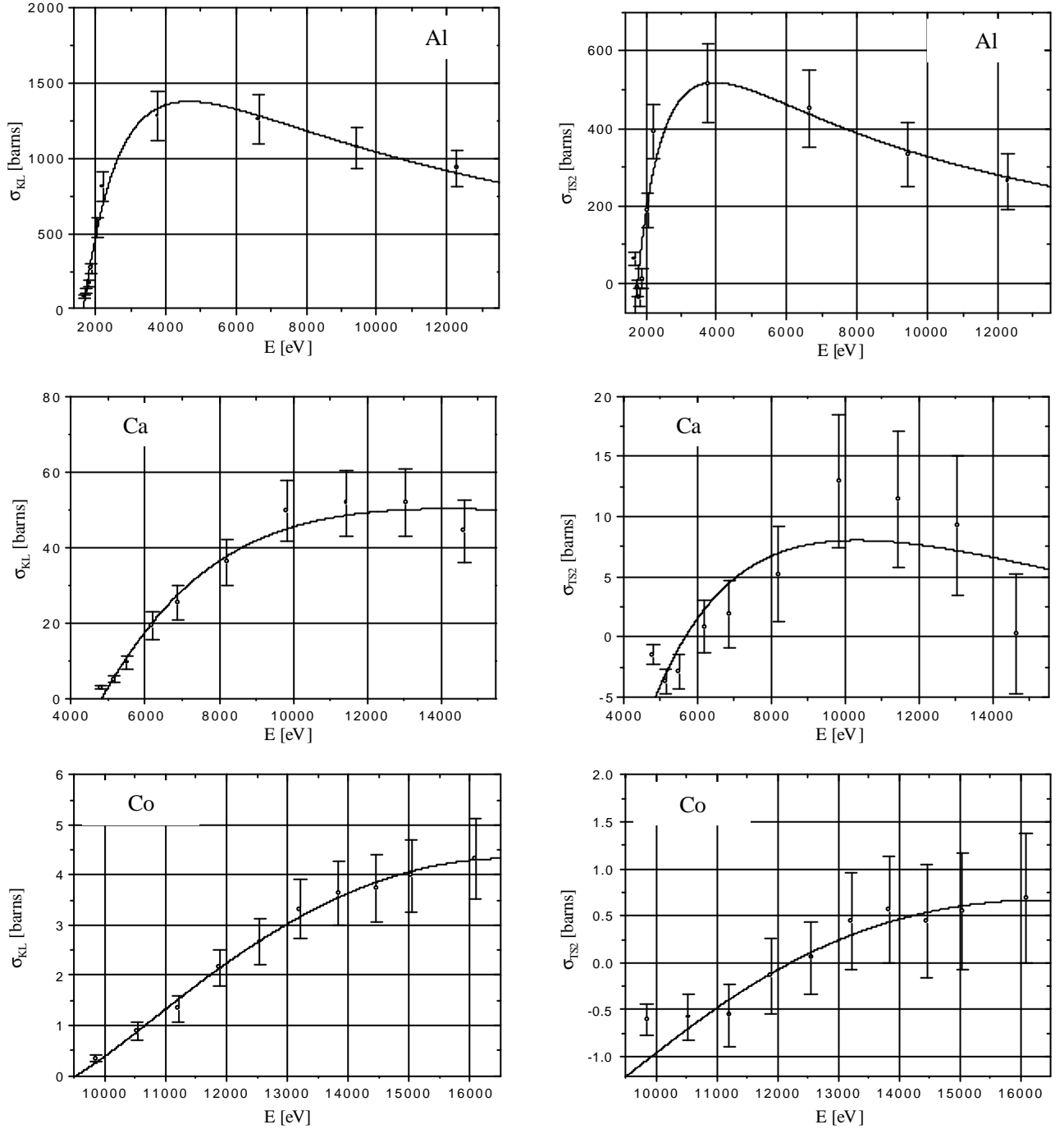


FIG. 5: Experimental cross sections corresponding to the electron-induced double KL excitation and TS2 process as a function of the electron energy. The negative values of σ_{TS2} close to the threshold are related to the method employed to determine the cross sections (more details are given in the text). The solid lines serve to guide the eye.

however, in contradiction with the sharp peak observed at 1.9 kV for the highest energy Lorentzian. As shown in Fig. 3, this sudden intensity increase of the third Lorentzian modifies

substantially the shape of the satellite spectrum. We are tempted to explain this peak by the $1s^1 2p^6 3p^1 \rightarrow 1s^1 2p^5 3p^2$ shakeup excitation which is strong for Al, but this explanation does not agree with the

MCDF calculations which suggest that a similar increase should then also exist for the second Lorentzian for which, however, an opposite trend is observed at 1.9 kV (small decrease of the intensity). The origin of this peak remains thus somewhat unclear. For Ca and Co, similar variations of the satellite line shapes as a function of the bombarding energy were observed. As for Al, the most spectacular changes were found for near threshold excitation energies. Here again, however, difficulties were encountered in the interpretation of the satellite profiles and no really reliable conclusions could be drawn from the observed evolution of the satellite line shapes.

B. Double KL shell ionization cross sections

The double ionization cross sections σ_{KL} obtained in the present work are presented in Tables III-V. They were derived from Eq. (3) and from the experimental single ionization cross sections σ_K reported in [2]. The values σ_K and σ_{KL} given in these tables correspond to the average electron-beam energies E_K , respectively E_{KL} , that were determined with the method described in Sec. II B. Also quoted in these tables are the satellite to diagram line yield ratios x_L , primary vacancy yield ratios i_L , and correction coefficients α . The errors on σ_{KL} include the statistical errors from the fitting procedure, the errors on the single ionization cross sections σ_K , and the uncertainties related to the rearrangement calculations. The statistical errors are reflected in the error values listed for the yields x_L , whereas the increased uncertainties observed for the yields i_L with respect to those of x_L originate from the rearrangement calculations. The errors on the cross sections σ_K were derived from the values

reported in [2]. The variation of the cross sections σ_{KL} as a function of the electron energy is depicted for the three targets in the left part of Fig. 5. For Al, one sees that, as in the case of single ionization, the double ionization cross section increases rapidly with the excitation energy, reaches a maximum value at an energy which is equal to ~ 3 times the threshold energy and then decreases smoothly with growing electron energies. For Ca and Co, similar shapes are expected but due to the maximum voltage of 20 kV at which the electron gun could be operated, the decreasing part of the curve is hardly visible (Ca) or even not visible (Co).

The solid lines of Fig. 5 which were obtained by fitting Gryzinski-like functions to the experimental data serve only to guide the eye and should thus not be regarded as theoretical predictions. Actually, the problem of electron-impact induced double ionization of atoms is very difficult to treat theoretically because the interaction of the incident electron with the atomic electrons during the process has a collective character. As a result, most theoretical works were devoted to the simplest collision $e + \text{He} \rightarrow 3e + \text{He}^{2+}$. However, even in this case, four charged particles (one ion and three electrons) interact via Coulomb forces in the final channel, making the correct treatment of this many-body problem extremely difficult. Actually, by now, no general theory based on quantum physics is available for the description of direct double ionization processes. The classical approach based on the binary encounter approximation (BEA) employed by Gryzinski [36] to study the electron-impact ionization of atoms and ions provides useful predictions in the case of single ionization cross sections (BEA1), whereas for double ionization cross sections (BEA2) the calculated cross sections

have to be scaled by 10^{-1} - 10^{-2} [48,49]. A more recent study by Gryzinski and Kunc [50] in which the original BEA2 approach was modified seems to provide theoretical double ionization cross sections that are in better agreement with the experimental results. These predictions, however, apply only to the double ionization of valence ns and nd electrons and are not applicable to the core-levels investigated in the present study. No theoretical values are thus available to make a comparison with our experimental double ionization cross sections s_{KL} .

As shown in Fig. 5, above the threshold energy the cross sections s_{KL} increase almost linearly with the electron energy. The straight line obtained for Al from the linear fit of the first five low-energy experimental points intercepts the $s_{KL} = 0$ axis at 1650(28) eV. This value is in good agreement with the double ionization threshold energy of 1659 eV deduced from the sum of the $1s$ binding energy of Al and the $2p$ binding energy of Si which are equal to 1559.6 and 99.4 eV, respectively [51]. For Ca and Co, threshold energies of 4638(75) and 9520(105) eV are found from Tables IV and V, that are both significantly higher than the values of 4437 and 8562 eV one would expect from [51], using the approximation $B_K(Z) + B_{L_3}(Z+1)$. For Co, a measurement was performed with the electron gun set at 9 kV. No satellite structure could be seen in the x-ray spectrum, indicating that the threshold energy lies above 9 keV or that the double ionization below 9 keV is extremely small. Actually, for each element the experimental point corresponding to the lowest measured energy is found to lie slightly above the fitted Gryzinski-like functions (see Fig. 5). This suggests that the slope of the curve diminishes when approaching the threshold so that the latter cannot be determined accurately from the

intersection with the $s_{KL} = 0$ axis of the straight line approximating the initial increase. This assumption is confirmed by the classical threshold law introduced many years ago by Wannier [52] and developed later by Grujic [53]. According to this law, close to the threshold the slope of the curve $s_{KL}(E)$ can be written in the following form:

$$\frac{ds_{KL}}{dE} = A \cdot (E_e - E_{thr,KL})^{2k-1}, \quad (16)$$

where $(E_e - E_{thr,KL})$ represents the excess electron energy, A an undetermined constant and k is a parameter which is close to unity but bigger. Relation (16) shows that, as anticipated, the slope is diminishing with decreasing excitation energies.

For Al and Ca, the cross sections $s_{KL}(E)$ are maximum at 4650 eV (1380 barns) and 14200 eV (50.3 barns), respectively, i.e. at energies somewhat smaller than the single ionization cross sections $s_K(E)$ whose maxima are found at 4880 eV (14.1 kbarns) and 16460 eV (1.67 kbarns). For Co, the energy for which $s_{KL}(E)$ is maximum lies above the point of highest energy that could be measured (16090 eV). However, from the fit of the Gryzinski-like function to the data, a value of 16650 eV (4.33 barns) is obtained which is also smaller than the energy of 19380 eV corresponding to the maximum value of s_K (562 barns). In the region $13 \leq Z \leq 27$ covered by our experiment, one finds from the above cross sections that the maximum values s_{KL}^{\max} scale as $Z^{7.9}$ whereas the ratios $s_{KL}^{\max} : s_K^{\max}$ which vary from 9.8% for Al down to 0.8% for Co scale as $Z^{-3.4}$.

C. TS2 cross sections

Double ionization resulting from photon impact is due to TS1 and shake processes. The contribution of the TS1 process which predominates at near-threshold excitation energies decreases rapidly with growing photon energy because the probability for the photoelectrons to collide with inner-shell electrons diminishes very fast with the velocity of the photoelectrons. Shake processes have exactly the opposite behavior. At low excitation energies, the photoelectrons which have low velocities need a relatively long time to escape from the atom core so that the change of the atomic potential due to the alteration in electronic screening is slow and, as a result, shakeup and shakeoff processes are rather improbable. At high excitation energies, the change in the atomic potential is fast and shake probabilities

are greater. If the change of the atomic potential is fast enough, the shake probability can be calculated within the so-called sudden approximation model [6,7,54,55]. In this model, the shake probability is given by the matrix element describing the overlap of the initial and final state wave functions of the electron undergoing the shake transition [7,56]. In other words, at excitation energies that are high enough to satisfy the criterion of applicability [5,57-59] of the sudden approximation, shake probabilities are expected to be constant. Due the combined influence of TS1 and shake processes, the photoinduced double ionization increases monotonically with the excitation energy. The increase which is rapid at the beginning becomes less and less steep as the excess energy relative to the threshold grows. At high energies, the double ionization tends asymptotically to a saturation limit

TABLE III: Al target. High voltage of the electron gun, average energies E_K and E_{KL} of the electrons producing the single K and double KL ionization, correction factor \mathbf{a} , satellite-to-diagram x-ray line yield ratio x_L , vacancy yield ratio i_L , average L-shell photoexcitation probability P_L^{photo} , and cross sections for single K-shell ionization, double KL ionization, and TS2 process. The single ionization cross sections were derived from the experimental values reported in [2].

| HV [kV] | E_K [keV] | E_{KL} [keV] | \mathbf{a} | x_L [%] | i_L [%] | P_L^{photo} [%] | $\mathbf{s}_K(E_K)$ [kbarns] | $\mathbf{s}_{KL}(E_{KL})$ [barns] | $\mathbf{s}_{TS2}(E_{KL})$ [barns] |
|-------------------|----------------|-------------------|--------------|--------------|--------------|----------------------|---------------------------------|--------------------------------------|---------------------------------------|
| 1.7 | 1.63 | 1.68 | 0.903 | 2.05(6) | 1.94(14) | 0.41(26) | 4.39(47) | 84(11) | 64(15) |
| 1.8 | 1.69 | 1.75 | 0.900 | 2.65(7) | 2.52(17) | 2.49(41) | 4.93(53) | 121(15) | -12(20) ^a |
| 1.9 | 1.75 | 1.82 | 0.902 | 3.37(5) | 3.20(21) | 3.49(36) | 5.47(59) | 170(21) | -35(22) ^a |
| 2.0 | 1.81 | 1.88 | 0.907 | 4.94(7) | 4.69(31) | 4.06(32) | 6.00(65) | 270(34) | 12(25) |
| 2.25 | 1.97 | 2.05 | 0.923 | 8.39(4) | 7.99(53) | 4.80(28) | 7.27(79) | 541(67) | 189(44) |
| 2.5 | 2.12 | 2.21 | 0.937 | 11.16(13) | 10.65(72) | 5.19(27) | 8.40(91) | 814(101) | 391(70) |
| 5.0 | 3.68 | 3.76 | 0.993 | 10.96(11) | 10.46(70) | 6.21(25) | 13.5(1.5) | 1282(162) | 516(102) |
| 10.0 | 6.66 | 6.64 | 0.999 | 10.70(11) | 10.21(69) | 6.55(29) | 13.6(1.5) | 1258(161) | 451(99) |
| 15.0 | 9.65 | 9.44 | 0.992 | 10.20(10) | 9.73(65) | 6.67(30) | 12.1(1.3) | 1074(136) | 332(83) |
| 20.0 | 12.77 | 12.28 | 0.983 | 9.99(3) | 9.53(63) | 6.73(30) | 10.7(1.2) | 936(118) | 263(70) |
| 30.0 ^b | 6.50 | | | 7.39(9) | 6.94(47) | 6.48(40) | | | |

^aThe negative sign originates from the method employed to determine \mathbf{s}_{TS2} (see text)

^bX-ray tube measurements.

that coincides with the shake probability corresponding to the sudden approximation.

In a recent experiment performed with mono-energetic photons of variable energy from a synchrotron radiation source [33] it was found that the variation of the double KL shell ionization of Ar from the adiabatic to the sudden regime could be well reproduced by the model of Thomas [60]. In another experiment concerning the double KM photoexcitation of Ge [61], a similar good agreement between experimental data and predictions from the Thomas model was obtained. In the approach of Thomas the probability for creation of a second inner-shell hole via a shake or TS1 process is given by

$$P_{\text{Thomas}}(E) = P_{\infty} \exp\left(-\frac{r^2 E_s^2}{15.32 \cdot (E - E_{thr})}\right), \quad (17)$$

where E stands for the x-ray beam energy, E_{thr} is the threshold energy for double KL excitation, E_s the shake energy, P_{∞} the excitation probability at saturation, and r the distance covered by the photoelectron during the time the atomic potential changes. In the above formula, the energies are expressed in eV and r in Å. In [33], the parameters P_{∞} , E_{thr} , and r were determined from a least-squares fit of the Thomas formula to the experimental probabilities, whereas the shake energy E_s was determined according to the $(Z+1)$ potential approximation. The value obtained from the fit for the distance r was found to be very close to the radius r_{\max} of the $3p$ orbital in ionic Ar^{1+} (r_{\max} is the radius for which the squared $3p$ wave function peaks), whereas the value obtained for E_{thr} was found to agree reasonably well with results of MCDF calculations concerning the lowest energy excitation, namely the $1s^1 3p^6 \rightarrow 1s^1 3p^5 4p^1$ shakeup transition. Applying these findings to the present

TABLE IV: Same as in Table III but for Ca.

| HV [keV] | E_K [keV] | E_{KL} [keV] | a | x_L [%] | i_L [%] | P_L^{photo} [%] | $s_K(E_K)$ [barns] | $s_{KL}(E_{KL})$ [barns] | $s_{TS2}(E_{KL})$ [barns] |
|-------------------|----------------|-------------------|-------|--------------|--------------|-----------------------------|-----------------------|-----------------------------|------------------------------|
| 5.0 | 4.60 | 4.81 | 0.840 | 0.70(3) | 0.76(7) | 0.99(19) | 374(57) | 2.8(5) | -1.5(8) ^a |
| 5.5 | 4.93 | 5.16 | 0.860 | 0.96(4) | 1.03(10) | 1.55(17) | 488(72) | 5.0(9) | -3.7(1.0) ^a |
| 6.0 | 5.27 | 5.51 | 0.882 | 1.47(8) | 1.58(17) | 1.83(16) | 601(87) | 9.4(1.7) | -2.9(1.4) ^a |
| 7.0 | 5.94 | 6.20 | 0.917 | 2.23(2) | 2.41(22) | 2.12(15) | 810(137) | 19.1(3.8) | 0.8(2.2) |
| 8.0 | 6.60 | 6.88 | 0.939 | 2.44(3) | 2.63(24) | 2.28(15) | 986(163) | 25.3(4.6) | 1.9(2.8) |
| 10.0 | 7.92 | 8.21 | 0.965 | 2.76(5) | 2.98(27) | 2.46(16) | 1246(185) | 36.1(6.2) | 5.2(4.0) |
| 12.5 | 9.54 | 9.84 | 0.982 | 3.28(1) | 3.55(32) | 2.58(16) | 1446(204) | 49.6(8.1) | 12.9(5.5) |
| 15.0 | 11.14 | 11.45 | 0.990 | 3.17(6) | 3.43(31) | 2.65(16) | 1561(234) | 51.8(8.6) | 11.4(5.7) |
| 17.5 | 12.73 | 13.04 | 0.995 | 3.05(5) | 3.30(30) | 2.70(17) | 1623(242) | 51.9(8.9) | 9.2(5.8) |
| 20.0 | 14.32 | 14.63 | 0.998 | 2.56(2) | 2.76(25) | 2.74(17) | 1654(273) | 44.4(8.3) | 0.2(5.0) |
| 60.0 ^b | 11.30 | | | 2.48(3) | 2.71(24) | 2.64(22) | | | |

^aThe negative sign originates from the method employed to determine s_{TS2} (see text)

^bX-ray tube measurements.

study, we have determined with the model of Thomas the variation of the double *KL* photoexcitation of Al, Ca, and Co from threshold to saturation. The radii r_{\max} were taken from [62], the shake energies E_s were computed within the (Z+1) potential approximation, using the binding energies quoted in [35], and the threshold energies were determined from MCDF calculations [63]. The probabilities P_{∞} were determined from the x-ray tube measurements, using the following relation:

$$P_{\text{Thomas}}(E_{\text{photo}}) = P_{\text{exp}}^{\text{photo}}, \quad (18)$$

where E_{photo} stands for the target dependent average energies of the x-ray tube bremsstrahlung (see Table II) and $P_{\text{exp}}^{\text{photo}}$ are the experimental shake probabilities. The latter were deduced from relation (7), using the yield ratios i_L^{photo} quoted in Tables III-V.

Another simple generic model permitting one to calculate the probability of photoinduced multiple electron excitation from threshold to saturation was published recently by Roy *et al.* [64]. In this model the double *KL* excitation probability can be written as [33]

$$P_{\text{Roy}}(E) = P_{\infty} \frac{2^4}{\pi} \int_1^{(E-B_K)/B_L} \frac{(X-1)^{1/2}}{X^4 \left(1 + \frac{1}{4} \frac{B_L}{E-B_K} X^2 \right)} dX. \quad (19)$$

Here, B_K represents the binding energy of the *K* shell in the neutral atom, B_L the binding energy of the *L* shell in the $1s^{-1}$ ion, and X is a dimensionless parameter defined by $X := 1 + E/B_L$. The energy dependent photoexcitation probabilities based on the model of Roy were computed for the three target elements, employing the (Z+1) potential approximation for B_L and the binding energies reported in [35]. As in the preceding case, the Roy

TABLE V: Same as in Table III but for Co.

| HV [keV] | E_K [keV] | E_{KL} [keV] | a | x_L [%] | i_L [%] | P_L^{photo} [%] | $s_K(E_K)$ [barns] | $s_{KL}(E_{KL})$ [barns] | $s_{TS2}(E_{KL})$ [barns] |
|-------------------|----------------|-------------------|-------|--------------|--------------|-----------------------------|-----------------------|-----------------------------|------------------------------|
| 10.0 | 9.27 | 9.85 | 0.754 | 0.15(1) | 0.19(2) | 0.40(6) | 180(22) | 0.34(6) | -0.61(17) ^a |
| 11.0 | 9.93 | 10.53 | 0.823 | 0.30(2) | 0.36(5) | 0.49(7) | 247(31) | 0.89(17) | -0.58(25) ^a |
| 12.0 | 10.58 | 11.21 | 0.865 | 0.35(2) | 0.44(5) | 0.54(8) | 304(41) | 1.33(26) | -0.56(33) ^a |
| 13.0 | 11.24 | 11.89 | 0.894 | 0.488(4) | 0.61(6) | 0.58(8) | 354(46) | 2.15(37) | -0.14(40) ^a |
| 14.0 | 11.88 | 12.55 | 0.915 | 0.540(7) | 0.68(7) | 0.61(8) | 395(51) | 2.67(46) | 0.05(38) |
| 15.0 | 12.52 | 13.21 | 0.932 | 0.619(6) | 0.78(8) | 0.63(8) | 429(56) | 3.32(60) | 0.44(51) |
| 16.0 | 13.15 | 13.84 | 0.946 | 0.64(1) | 0.80(8) | 0.64(9) | 458(60) | 3.64(64) | 0.56(57) |
| 17.0 | 13.78 | 14.46 | 0.958 | 0.623(7) | 0.78(8) | 0.66(9) | 482(63) | 3.73(68) | 0.44(60) |
| 18.0 | 14.40 | 15.04 | 0.968 | 0.64(1) | 0.80(8) | 0.67(9) | 502(66) | 3.99(72) | 0.54(62) |
| 20.0 | 15.63 | 16.09 | 0.985 | 0.65(3) | 0.82(9) | 0.68(9) | 531(68) | 4.32(79) | 0.68(69) |
| 90.0 ^b | 16.50 | | | 0.55(3) | 0.69(10) | 0.69(10) | | | |

^aThe negative sign originates from the method employed to determine s_{TS2} (see text)

^bX-ray tube measurements.

function was anchored to the experimental probabilities $P_{\text{exp}}^{\text{photo}}$ deduced from the x-ray tube measurements.

The curves corresponding to the two models are presented for Al in Fig. 6, where they are compared to the experimental ratios $\sigma_{KL}:\sigma_K$ of the double-to-single ionization cross sections. One sees that the ratios of the electron-induced cross sections are bigger than the photoexcitation probabilities. According to Eq. (4), the differences originate from the TS2 process which does not exist in the case of photon bombardment. From Fig. 6 one also sees that the two models do not provide exactly the same probabilities. In particular, the initial increase is steeper for the Thomas curve and the saturation

value P_{∞} derived from Roy's model is slightly bigger. As in [33] both models were found to reproduce satisfactorily the experimental data, average values derived from the two models were adopted for the photoexcitation probabilities P_L^{photo} . The cross sections σ_{TS2} were then computed using Eq. (6). The results are presented in Tables III (Al), IV (Ca) and V (Co) together with the probabilities P_L^{photo} . The uncertainties on the parameters entering the Thomas and Roy models and the errors on the cross sections σ_K are included in the errors quoted in Tables III-V for the cross sections σ_{TS2} . However, the crude approximations made to extract the cross sections σ_{TS2} , in particular the non-consideration of the interference terms, are not reflected in the quoted errors. Thus the cross

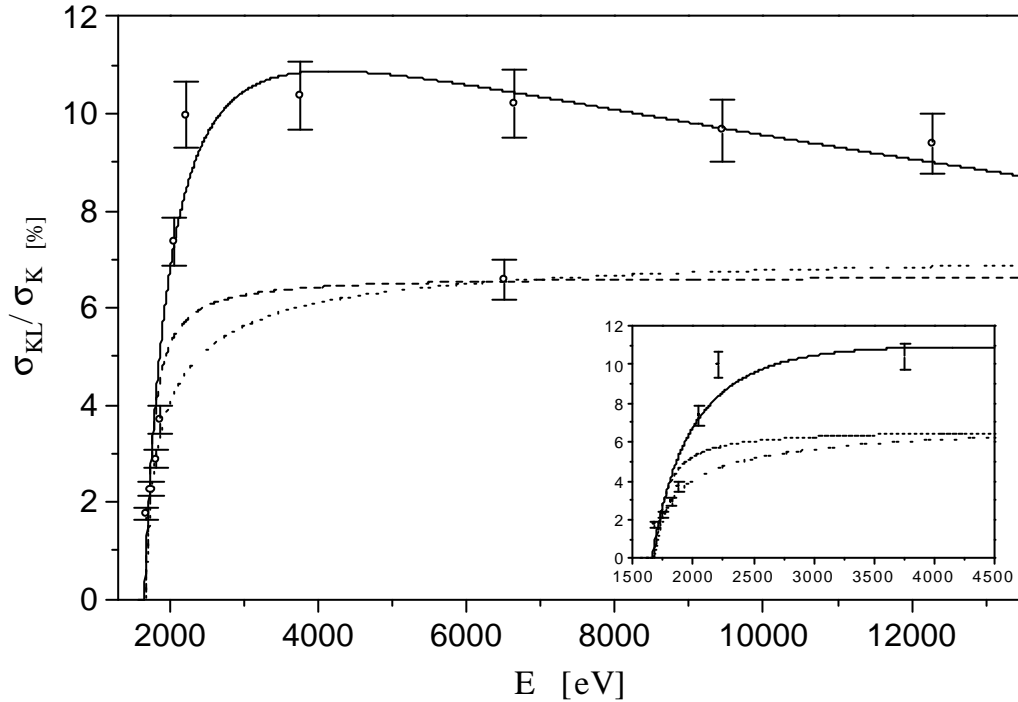


FIG 6: Al target. Comparison between the ratio of the electron-induced double-to-single ionization cross sections (solid line) and the probability for L-shell excitation following 1s photoionization. The energy dependence of the photoexcitation probability was calculated, using the model of Thomas [60] (dashed line) and the model of Roy [64] (dotted line). Both curves were anchored to the experimental point at 6500 eV which was obtained by irradiating the target with the bremsstrahlung of an x-ray tube.

sections σ_{TS2} obtained in the present study have to be considered cautiously and regarded only as rough estimations. The plots of the cross sections σ_{TS2} versus bombarding energy are depicted for the three targets in the right part of Fig. 5.

The obtained cross sections σ_{TS2} are found to be maximum at about the same energies as the cross sections σ_{KL} . This statement is based on the Al data for which the relative uncertainties on the cross sections are the smallest ($\sim 20\%$). For Ca and Co, it seems that the energies maximizing the cross sections σ_{TS2} are somewhat lower but this conclusion is dubious in view of the large errors characterizing the Ca and Co results. From the plots, one sees that the maximum values of the two-step-two cross sections are approximately 520 barns, 13 barns and 0.7 barn for Al, Ca, and Co, respectively. From these results the scaling law $\sigma_{TS2} \sim Z^{-9.0}$ is found for the investigated domain $13 \leq Z \leq 27$. Since for the cross sections σ_{KL} a $Z^{7.9}$ dependence was obtained, one can conclude that the contribution of the TS2 process to the double *KL* ionization, a contribution which is about 40% for Al, 25% for Ca, and 15% for Co, diminishes approximately as Z^1 . To our knowledge there are no experimental data nor theoretical predictions concerning the Z -dependence of the ratio σ_{TS2}/σ_{KL} in the literature. The variation $\sigma_{TS2}/\sigma_{KL} \sim Z^{-1}$ observed in the present work, which is somewhat intriguing and difficult to explain, requires thus further investigations in both experiment and theory to be clarified.

As shown in Fig. 5 or in Tables III-V, at near threshold excitation energies negative values are obtained for the cross sections σ_{TS2} . Despite their large uncertainties, the negative results are in several cases not consistent with zero. This anomaly arises

from the approximation (5) we used to derive the σ_{TS2} cross sections. The assumption that the shake probabilities are the same for the electron and photon impact is certainly correct. For the TS1 process, however, this assumption is a very crude approximation, because in photoionization the excess energy is entirely transferred to the photoelectron, whereas in the electron-induced ionization the excess energy is shared between the scattered and ejected electrons. As a consequence, for the same bombarding energy, that we suppose for our explanation to be equal to the threshold energy for double *KL* excitation, in the photoexcitation case the velocity of the photoelectron K is just sufficient to kick out an *L* shell electron, whereas, in the case of electron-induced excitation, neither a TS1 nor a TS2 process is energetically possible. Thus one does expect that the threshold lies a little bit higher in energy when the target is bombarded with electrons. Now, if the electron energy is sufficiently increased to permit a TS1 or TS2 process to occur, the double excitation probability would be bigger than the one measured with photons of the same energy, because the velocity of the ejected or scattered electrons is smaller than the one of the photoelectrons. In other words, the threshold of the electron-induced double excitation is slightly shifted towards higher energies with respect to that of photoexcitation but the increase with growing energies of the cross section σ_{KL} is faster for electron impact. This situation corresponds well to our observations and explains, in particular, the negative sign of the cross sections σ_{TS2} near the threshold. For these reasons, in the energy region where the double *KL* excitation is dominated by the TS1 process, the experimental method employed to determine σ_{TS2} is not reliable and the results obtained for the near threshold two-

step-two cross sections have thus to be considered cautiously. It is not easy to determine from which energy the TS1 process becomes negligible. An analogous problem was addressed by Feinberg [65] for the case of \mathbf{b} decay. The mechanism of \mathbf{b} decay is similar to that of K shell ionization since the \mathbf{b} electron emerges from the center of the atom, while the K photoelectron emerges nearly from the center. The result of Feinberg's study was that the TS1-to-shake probability ratio can be estimated in \mathbf{b} decay by the simple following relation:

$$\frac{P_K^{TS1}}{P_K^{shake}} \approx \frac{B_K}{E_b}, \quad (20)$$

where B_K represents the binding energy of the K shell and E_b the energy of the \mathbf{b} particle. Applying Feinberg's estimation to our case and assuming that half of the excess energy is given to the ejected K electron, one obtains:

$$\frac{P_L^{TS1}}{P_L^{shake}} \approx \frac{B_L}{0.5(E - B_K)}, \quad (21)$$

where B_L is the average binding energy of the L shell. Assuming furthermore that our method is adequate if $P_L^{TS1}/P_L^{shake} \leq 0.3$, one finds from Eq. (21) that the cross sections σ_{TS2} obtained for Al, Ca, and Co are reliable if the bombarding energies are higher than 2.05, 6.60, and 13.2 keV, respectively. Despite the very crude approximations made to estimate these energies, the obtained values look reasonable with respect to the results quoted in Tables III-V.

ACKNOWLEDGMENTS

The authors wish to thank Dr. M. Polasik (University of Torun, PL) for the MCDF calculations. This work was partly supported by the Swiss National Science Foundation.

-
- | | |
|---|--|
| <p>[1] X. Long, M. Liu, F. Ho, and X. Peng, <i>At. Data Nucl. Data Tables</i> 45, 353 (1990).</p> <p>[2] M. Liu, Z. An, C. Tang, Z. Luo, X. Peng, and X. Long, <i>At. Data Nucl. Data Tables</i> 73, 213 (2000), and references therein.</p> <p>[3] H. Deutsch, D. Margreiter, and T.D. Märk, <i>Z. Phys. D: At., Mol. Clusters</i> 29, 31 (1994).</p> <p>[4] C. Tuang, Z. Luo, Z. An, F. He, X. Peng, and X. Long, <i>Phys. Rev. A</i> 65, 052707 (2002).</p> <p>[5] T.A. Carlson and M.O. Krause, <i>Phys. Rev.</i> 140, A1057 (1965).</p> <p>[6] T. Åberg, <i>Phys. Rev.</i> 156, 35 (1967).</p> | <p>[7] T.A. Carlson and C.W. Nestor, Jr., <i>Phys. Rev. A</i> 8, 2887 (1973).</p> <p>[8] J.H. McGuire, <i>Phys. Rev. Lett.</i> 49, 1153 (1982).</p> <p>[9] J.H. McGuire, N.C. Deb, O.L. Weaver, T. Ishihara, L. Kocbach, and T. Mukoyama, <i>Nucl. Instrum. Methods Phys. Res. B</i> 40/41, 340 (1989).</p> <p>[10] Yu V. Popov, C. Dal Cappello, B. Joulakian, and N.M. Kuzmina, <i>J. Phys. B</i> 27, 1599 (1994).</p> <p>[11] B. El Marji, C. Schröter, A. Duguet, A. Lahmam-Bennani, M. Lecas, and L. Spielberger, <i>J. Phys. B</i> 30, 3677 (1997).</p> |
|---|--|

- [12] C. Dal Cappello, R. El Mkhater, and P.A. Hervieux, *Phys. Rev. A* **57**, R693 (1998).
- [13] A. Lahmam-Bennani, C. Dupré, and A. Duguët, *Phys. Rev. Lett.* **63**, 1582 (1989).
- [14] A. Duguët and A. Lahmam-Bennani, *Z. Phys. D: At., Mol. Clusters* **23**, 383 (1992).
- [15] M.J. Ford, B. El Marji, J.P. Doering, J.H. Moore, M.A. Coplan, and J.W. Cooper, *Phys. Rev. A* **57**, 325 (1998).
- [16] R.D. Deslattes, R.E. La Villa, P.L. Cowan, and A. Henins, *Phys. Rev. A* **27**, 923 (1983).
- [17] J.-Cl. Dousse and J. Hozowska, *Phys. Rev. A* **56**, 4517 (1997).
- [18] O. Mauron, J.-Cl. Dousse, J. Hozowska, J.P. Marques, F. Parente, and M. Polasik, *Phys. Rev. A* **62**, 62508 (2000).
- [19] V. Cindro, M. Budnar, M. Kregar, V. Ramsak, and Z. Smit, *J. Phys. B* **22**, 2161 (1989).
- [20] T. Ludziejewski, P. Rymuza, Z. Sujkowski, B. Boschung, J.-Cl. Dousse, B. Galley, Z. Halabuka, Ch. Herren, J. Hozowska, J. Kern, Ch. Rhême, and M. Polasik, *Phys. Rev. A* **52**, 2791 (1995).
- [21] M. Carlen, J.-Cl. Dousse, M. Gasser, J. Hozowska, J. Kern, Ch. Rhême, P. Rymuza, and Z. Sujkowski, *Z. Phys. D: At., Mol. Clusters* **23**, 71 (1992).
- [22] B. Boschung, J.-Cl. Dousse, B. Galley, Ch. Herren, J. Hozowska, J. Kern, Ch. Rhême, Z. Halabuka, T. Ludziejewski, P. Rymuza, Z. Sujkowski, and M. Polasik, *Phys. Rev. A* **51**, 3650 (1995).
- [23] Ch. Herren, B. Boschung, J.-Cl. Dousse, B. Galley, J. Hozowska, J. Kern, Ch. Rhême, M. Polasik, T. Ludziejewski, P. Rymuza, and Z. Sujkowski, *Phys. Rev. A* **57**, 235 (1998).
- [24] R.L. Watson, B.I. Sonobe, J.A. Demarest, and A. Langenberg, *Phys. Rev. A* **19**, 1529 (1979).
- [25] D.F. Anagnostopoulos, G.L. Borchert, and D. Gotta, *J. Phys. B* **25**, 2771 (1992).
- [26] M. Carlen, B. Boschung, J.-Cl. Dousse, Z. Halabuka, J. Hozowska, J. Kern, Ch. Rhême, M. Polasik, P. Rymuza, and Z. Sujkowski, *Phys. Rev. A* **49**, 2524 (1994).
- [27] M. Kavcic, M. Budnar, A. Mühleisen, P. Pelicon, Z. Smit, M. Zitnik, D. Castella, D. Corminboeuf, J.-Cl. Dousse, J. Hozowska, P.-A. Raboud, and K. Tökési, *Phys. Rev. A* **61**, 052711 (2000).
- [28] T. Ludziejewski, P. Rymuza, Z. Sujkowski, G. Borchert, J.-Cl. Dousse, Ch. Rhême, and M. Polasik, *Phys. Rev. A* **54**, 232 (1996).
- [29] M. Pajek, D. Banas, D. Castella, D. Corminboeuf, J.-Cl. Dousse, Y.-P. Maillard, O. Mauron, P.-A. Raboud, D. Chmielewska, I. Fijal, M. Jaskola, A. Korman, T. Ludziejewski, J. Rzakiewicz, Z. Sujkowski, J. Hozowska, M. Polasik, and T. Mukoyama, *Phys. Scr. T* **92**, 382 (2001).
- [30] D. Banas, M. Berset, D. Chmielewska, M. Czarnota, J.-Cl. Dousse, J. Hozowska, Y.-P. Maillard, O. Mauron, T. Mukoyama, M. Pajek, M. Polasik, P.A. Raboud, J. Rzakiewicz, and Z. Sujkowski, Abstracts of the XXII International Conference on Photonic, Electronic and Atomic Collisions ICPEAC 2001, Santa Fe, 2001 (unpublished).
- [31] M.O. Krause, T.A. Carlson, and R.D. Dismukes, *Phys. Rev.* **170**, 37 (1968).
- [32] G.B. Armen, T. Åberg, K.R. Karim, J.C. Levin, B. Crasemann, G.S. Brown, M.H. Chen, and G.E. Ice, *Phys. Rev. Lett.* **54**, 182 (1985).
- [33] P.-A. Raboud, M. Berset, J.-Cl. Dousse, Y.-P. Maillard, O. Mauron, J. Hozowska, M. Polasik, and J. Rzakiewicz, *Phys. Rev. A* **65**, 062503 (2002).
- [34] E. Storm and H.I. Israel, *Nucl. Data Tables* **7**, 565 (1970).
- [35] <http://physics.nist.gov/PhysRefData>.
- [36] M. Gryzinski, *Phys. Rev.* **138**, A336 (1965).
- [37] J. Hozowska, J.-Cl. Dousse, J. Kern, and Ch. Rhême, *Nucl. Instrum. Methods Phys. Res. A* **376**, 129 (1996).

- [38] A. Mühleisen, M. Budnar, J.-Cl. Dousse, J. Hoszowska, and Z.G. Zhao, *X-Ray Spectrom.* **27**, 337 (1998).
- [39] P.-A. Raboud, J.-Cl. Dousse, J. Hoszowska, and I. Savoy, *Phys. Rev. A* **61**, 12507 (2000).
- [40] J.A. Bearden, *Rev. Mod. Phys.* **39**, 78 (1967).
- [41] D.W. Fischer and W.L. Baun, *J. Appl. Phys.* **36**, 534 (1965).
- [42] M.O. Krause and J.G. Ferreira, *J. Phys. B* **8**, 2007 (1975).
- [43] F. James and M. Roos, *Comput. Phys. Commun.* **10**, 343 (1975).
- [44] Ch. Herren and J.-Cl. Dousse, *Phys. Rev. A* **56**, 2750 (1997), and references therein.
- [45] F.P. Larkins, *At. Data Nucl. Data Tables* **20**, 313 (1977).
- [46] E.J. McGuire, *Phys. Rev. A* **3**, 587 (1971).
- [47] J.L. Campbell and T. Papp, *At. Data Nucl. Data Tables* **77**, 1 (2001).
- [48] K. Tinschert, A. Müller, R.A. Phaneuf, G. Hofmann, and E. Salzborn, *J. Phys. B* **22**, 1241 (1989).
- [49] M. Zambra, D. Belic, P. Defrance, and D.J. Yu, *J. Phys. B* **27**, 2383 (1994).
- [50] M. Gryzinski and J.A. Kunc, *J. Phys. B* **32**, 5789 (1999).
- [51] G. Williams, <http://xray.uu.se/hypertext/EbindEnergies.html>.
- [52] G.H. Wannier, *Phys. Rev.* **100**, 1180 (1955).
- [53] P. Grujic, *J. Phys. B* **16**, 2567 (1983).
- [54] F. Bloch, *Phys. Rev.* **48**, 187 (1935).
- [55] L.G. Parrat, *Rev. Mod. Phys.* **31**, 616 (1959).
- [56] T. Mukoyama and K. Taniguchi, *Phys. Rev. A* **36**, 693 (1987).
- [57] V.P. Sachenko and V.F. Demekhin, *Zh. Eksp. Teor. Fiz.* **49**, 765 (1965) [*Sov. Phys. JETP* **22**, 532 (1966)].
- [58] T.A. Carlson, W.E. Moddemann, and M.O. Krause, *Phys. Rev. A* **1**, 1406 (1970).
- [59] M.O. Krause, *J. Phys. (Paris) Colloq. Suppl.* **10**, 32, C4-67 (1971).
- [60] T.D. Thomas, *Phys. Rev. Lett.* **52**, 417 (1984).
- [61] C. Sternemann, A. Kaprolat, M.H. Krisch, and W. Schülke, *Phys. Rev. A* **61**, 020501 (2000).
- [62] J.P. Desclaux, *At. Data Nucl. Data Tables* **12**, 312 (1973).
- [63] M. Polasik, *Phys. Rev. A* **52**, 227 (1995).
- [64] M. Roy, J.D. Lindsay, S. Louch, and S.J. Gurman, *J. Synchrotron Radiat.* **8**, 1103 (2001).
- [65] E.L. Feinberg, *Yad. Fiz.* **1**, 612 (1965) [*Sov. J. Nucl. Phys.* **1**, 438 (1965)].

Part III

Revisited L_3 and M_1 atomic-level widths of elements 54 $\leq Z \leq 77$

O. Mauron, J.-Cl. Dousse, S. Baechler, M. Berset, Y.P. Maillard, and P.A. Raboud
Department of Physics, University of Fribourg, Chemin du Musée 3, CH-1700 Fribourg, Switzerland

J. Hozowska
European Synchrotron Radiation Facility, 6 Jules Horowitz, F-38043 Grenoble, France

High-resolution measurements of the photoinduced L_3 - M_1 and L_3 - $M_{4,5}$ x-ray emission lines were performed with a reflection-type bent-crystal spectrometer for a variety of elements ranging from xenon ($Z=54$) to iridium ($Z=77$). The measurements were performed at the European Synchrotron Radiation Facility (ESRF) in Grenoble, France. From the observed linewidths of the L_3 - M_1 x-ray transitions, the widths of the M_1 levels were determined using the L_3 level widths extracted from the measured L_3 - M_5 transitions, and assuming for the M_5 levels the widths reported recently by Campbell and Papp [At. Data Nucl. Data Tables **77**, 1 (2001)]. In the rare-earth region a Z-dependent broadening of the M_1 level was observed.

PACS number(s): 32.70.Jz, 32.30.Rj, 32.80.Fb, 34.50.Fa

I. INTRODUCTION

M radiative yields are very small. As a consequence, the natural widths of the M -subshells are dominated by radiationless decay. For the M_1 level, the width is essentially governed by the Coster-Kronig (CK) process. Because the rate of CK processes depends strongly on small binding energy differences, calculations of the M_1 widths are extremely sensitive to details of the atomic potential. It has been widely observed that calculations performed within the independent-particle model (IPM) overestimate significantly the

CK yields so that theoretical IPM predictions for the $3s$ atomic-level widths are poorly reliable. Many-body theory (MBT) calculations of CK yields lead to an improved but not perfect agreement with experimental data. Unfortunately, such calculations which were performed only for a restricted subset of levels and restricted regions of atomic number do not exist for the M_1 -subshell.

Recently, Campbell and Papp assembled a large number of literature experimental data from a variety of spectroscopic methods from which they could derive a self-consistent set of widths of the

atomic levels $K-N_7$ for most elements across the periodic table [1,2]. The M_1 widths recommended by Campbell and Papp for elements below $Z=55$ are predominantly from x-ray photo-electron spectroscopy (XPS) [3-5] with a few re-calculated x-ray emission spectroscopy (XES) values that were derived from measured L_2-M_1 and L_3-M_1 x-ray transition widths [6]. A more recent result concerning Xe [7] was also considered. Above $Z=55$, where there is a serious dearth of modern experimental data, Campbell and Papp have used XES data points concerning the L_3-M_1 transitions of ^{69}Tm , ^{77}Ir , ^{79}Au , ^{82}Pb , ^{90}Th and ^{92}U [8-14], assuming their recommended values for the L_3 widths, to define a curve that connects smoothly to the data below $Z=55$.

As shown above, between Xe ($Z=54$) and Ir ($Z=77$) there is a single experimental result that concerns ^{69}Tm [8]. In addition this result has a rather large uncertainty of about 20%. Therefore, as pointed out by Campbell and Papp, modern XES data are required across that region of atomic number. This represented the principal aim of the present work. A further objective was to check if the M_1 widths determined by Campbell and Papp from the few XES data existing in the upper part of the periodic table are not overestimated, most of the measured L_3-M_1 x-ray transitions being indeed broadened by unresolved N -satellite structures that originate from L_1L_3N CK transitions. The third objective was to verify whether the M_1 -subshell of lanthanides is also affected by the splitting effect and resulting level broadening observed some years ago in 4s and 5s XPS measurements of rare-earth elements [15] and more recently in XES measurements of Sm and Ho $L_1-M_{4,5}$ transitions [16].

The main outcome of the present work is a new set of experimental M_1 level widths for ^{54}Xe , ^{56}Ba , ^{57}La , ^{59}Pr , ^{60}Nd , ^{62}Sm , ^{64}Gd , ^{65}Tb , ^{66}Dy , ^{67}Ho , ^{70}Yb , ^{74}W and ^{77}Ir . Spin-off results are reliable experimental data concerning the L_3 level widths and $L_3-M_{4,5}$ and L_3-M_1 x-ray transition energies for the thirteen investigated elements.

II. EXPERIMENT

A. Experimental method

As the width of an x-ray transition is given by the sum of the widths of the two atomic levels involved in the transition and because M_5 level widths reported by Campbell and Papp [2] for the studied elements have a precision better than 0.1 eV, the M_1 widths were determined from coupled measurements of the L_3-M_1 and L_3-M_5 photoinduced transitions. In other words, from the well known widths of the levels M_5 and the measured linewidths of the L_3-M_5 transitions, the level widths L_3 were first determined. Subtracting then the latter from the observed linewidths of the transitions L_3-M_1 precise and reliable results for the M_1 level widths could be obtained.

As mentioned in Sect. I, L_3N double vacancy states may be created in target atoms bombarded by photons as a result of L_1L_3N and L_2L_3N CK transitions or N -shell shake processes following the L_3 -subshell photoionization. Measured L_3 x-ray lines consist thus of overlapping transitions corresponding to the radiative decay of single L_3 and double L_3N vacancy states. Actually the N satellite x-ray lines that correspond to the radiative decay of the double L_3N vacancies cannot be resolved from the parent diagram lines because the energy shifts of

these satellites are smaller than the natural widths of the transitions. As a consequence, in most cases, fluorescence L_3 x-ray lines are broadened and their measured linewidths do not reflect exactly the L_3 level widths. The energy shifts of O - and P -satellites being markedly smaller, their influence on the widths of the parent diagram lines can be neglected. Furthermore, as L_1L_3M CK transitions are energetically forbidden for the elements investigated in the present study and because shake processes are about ten times less probable for the M -shell than for the N -shell, the influence of M -satellites can also be neglected. The line broadening and line asymmetry induced by the

unresolved N satellite structures have, however, to be considered. They make the data analysis more difficult and the obtained linewidths less reliable.

The difficulty caused by the unresolved N -satellites originating from $L_{1,2}L_3N$ CK transitions can be circumvented by irradiating the targets with monoenergetic photons whose energy is bigger than the L_3 edge but smaller than the $L_{1,2}$ edges. Similarly, N -shell shake processes can be biased by using bombarding energies that are below the threshold energy for double L_3+N excitation. Such experimental requirements can be fulfilled using energy tunable synchrotron radiation (SR). The line

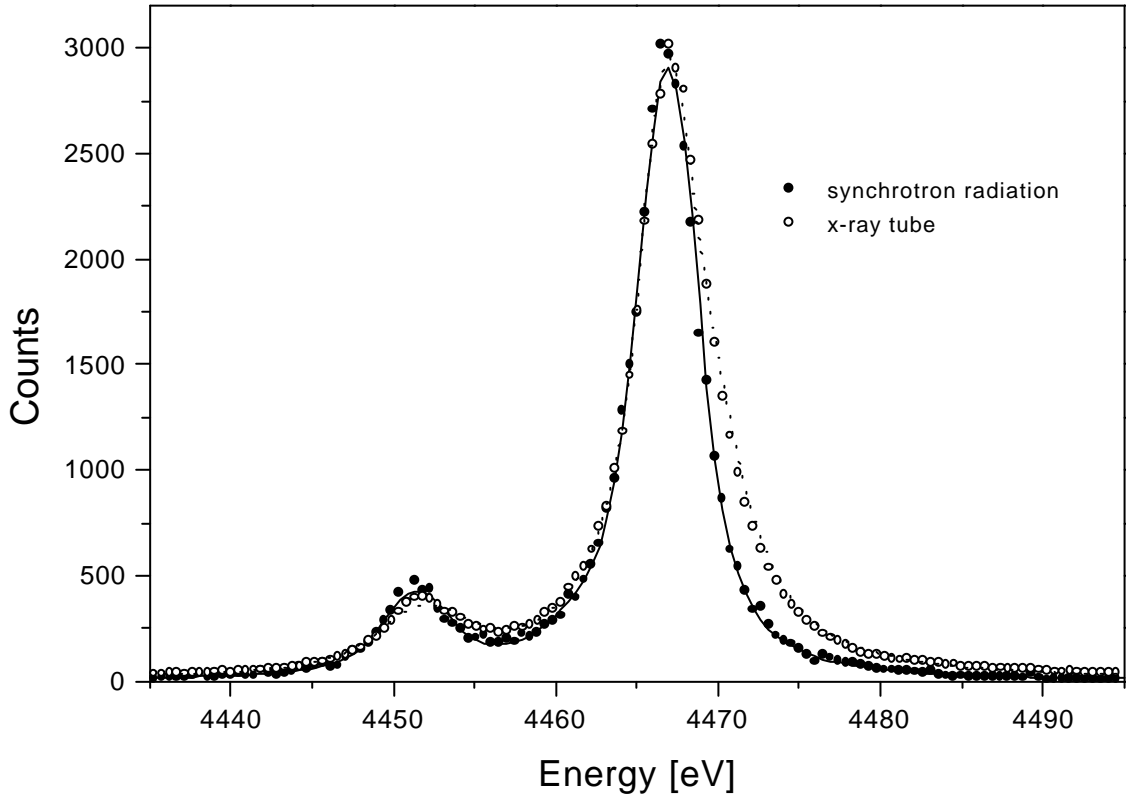


FIG. 1: High-resolution $La_{1,2}$ x-ray spectrum of barium induced by photoionization using an x-ray tube (20 kV) and 5300 eV synchrotron radiation. The line observed with the x-ray tube is broadened by unresolved N satellite structures resulting predominantly from L_1L_3N and L_2L_3N Coster-Kronig transitions.

shape dependence of photoinduced x-ray lines on the excitation energy is depicted for the L_3 - $M_{4,5}$ transitions of Ba in Fig. 1. In the spectrum corresponding to the irradiation of the target with the bremsstrahlung from an x-ray tube operated at 20 kV (i.e. far above the L_1 edge of Ba) the broadening effect of the unresolved N -satellites is clearly visible on the high-energy flank of the L_3 - M_5 transition whereas no similar effect is observed in the SR-induced transition. Furthermore, to get precise and reliable atomic-level widths, the use of an instrument with a resolution that is comparable or better than the linewidths of interest is mandatory. For these reasons, the L_3 - $M_{4,5}$ and L_3 - M_1 transitions were measured by means of a high-resolution Bragg-type von Hamos curved crystal spectrometer [17], using synchrotron radiation for the production of the target fluorescence.

B. Experimental set-up

The measurements were performed at the European Synchrotron Radiation Facility (ESRF), Grenoble, France. For elements below $Z=67$ the von Hamos spectrometer was installed at the x-ray microscopy beamline ID21. As synchrotron radiation above about 8 keV cannot be obtained at ID21, the measurements of elements with higher atomic number were performed at the x-ray optics beamline BM5.

A detailed description of the von Hamos spectrometer can be found in Ref. [17]. The Bragg angle domain covered by the spectrometer extends from 24.4° to 61.1° , so that two different crystals were needed for covering the ~ 6 -keV-wide energy range corresponding to the transitions studied in this work. For the observation of transitions below

5 keV, the spectrometer was equipped with a (200) LiF crystal ($2d = 4.0280 \text{ \AA}$). Above 5 keV, a ($2\bar{2}3$) quartz crystal ($2d=2.7500 \text{ \AA}$) was employed. Both crystals were 10-cm-high, 5-cm-wide, and 0.5-mm-thick. They were glued to Al blocks machined to a precise concave cylindrical surface with a bending radius of 25.4 cm. The spectrometer was operated in the so-called slit-geometry. In this geometry, the target is viewed by the crystal through a narrow vertical rectangular slit. The latter consists of two juxtaposed Ta pieces 0.3 mm thick and 10 mm high. The slit width can be adjusted continuously from 0.005 mm to 0.5 mm with a micrometer screw. As an increase of the slit width degrades the instrumental resolution but increases the spectrometer luminosity, a slit width of 0.2 mm was chosen, to satisfy at best the specific conditions of the present experiment. The x-rays were recorded with a CCD (charged-coupled device) position-sensitive detector 27.65 mm long and 6.9 mm high, having a depletion depth of 50 μm and consisting of 1024 columns and 256 rows with a pixel size of $27 \times 27 \mu\text{m}^2$.

The CCD detector was thermoelectrically cooled down to -60°C . Its position along the dispersion axis, which has to be known accurately for a precise determination of the energy of the measured transitions, was determined by means of an optical diffraction device with a precision of $\pm 3 \mu\text{m}$. The diffracted x-rays hitting the CCD build a two-dimensional pattern on the detector plane. The horizontal axis of the detector corresponds to the energy axis of the x-ray spectrum, while the vertical extension of the detector serves mainly to collect more intensity. The time of a single acquisition was chosen depending on the count rate, so that multiple hits on one pixel were minimized. Thanks to the

good energy resolution of the CCD detector, higher-order reflections and background events could be rejected by setting appropriate energy windows. The data were taken in a repetitive accumulation mode. Depending on the strength of the measured transition and SR intensity, the number of collected images varied between 300 and 3000 with 1-10 s exposure times per image. Each image corresponding to a separate acquisition was filtered. Then the different images were summed and the resulting two-dimensional frame was projected on the axis of dispersion to give the one-dimensional position spectrum.

At ID21 the spectrometer was installed downstream of the STXM microscope chamber to which it was connected through a ~ 180 -cm-long evacuated pipe (Fig. 2). On the spectrometer side the pipe was closed with a 25- μm -thick KaptonTM window in order to permit an access to the spectrometer chamber without degrading the high vacuum in the beamline. The x-ray beam was monochromatized by means of a fixed exit Si(111) double-crystal monochromator having a resolving power of 10^4 , i.e., an energy resolution better than 1 eV over the entire energy domain of interest (4050 eV-7720 eV). In order to minimize the above-mentioned satellite-induced broadening of the lines, an efficient rejection of upper harmonics was needed. The latter was realized using a Si-based Ni coated mirror for synchrotron radiation energies below 5.5 keV and a Si-based Rh coated mirror for higher energies. With these mirrors, tilted by 8.2 mrad with respect to the beam direction, an harmonic rejection better than 10^{-3} and a transmission bigger than 70% could be achieved. A beam size of about 2 mm in diameter was used in order to reach the 10^{11} - 10^{12} incident

photons/s needed on the targets to observe the weak L_3 - M_1 transitions with sufficient statistical quality in reasonably long acquisition times.

At BM5 the spectrometer was installed in the second experimental hutch at a distance of about 55 m from the radiation source. Due to a lack of space, the spectrometer chamber was rotated around the target vertical axis by 180 deg. (Fig. 2) with respect to the set-up employed at ID21. In this set-up the SR beam was thus entering the spectrometer chamber through a 25- μm -thick KaptonTM foil mounted on the window where the beam-stop is usually placed in standard-geometry experiments. Each metallic target foil was oriented so that the angle between the target plane and the SR beam was the same as the angle between the target plane and the target-crystal direction. As a consequence, at BM5, the angles between the target plane and the direction of observation of the target fluorescence x-rays were smaller (23-30 deg.) than in the standard set-up employed at ID21 (60-70 deg.). This resulted in an increased self-absorption of the fluorescence x-rays in the targets and to a bigger sensitivity of the measurements on the SR beam profile, the target area viewed through the slit by the crystal being larger. The photon energy was monochromatized by a Si(111) double-crystal fixed-exit monochromator. Due to the large distance between the latter and the samples as well as a bending magnet beam, the monochromator's second crystal was replaced by a sagittally focusing one. Thanks to this sagittal focusing device [18] the photon flux on the samples could be increased by two orders of magnitude. With this gain, a flux of 10^9 - 10^{10} photons/s/mm² with an energy resolution of ~ 1 eV was achieved. The beam spot size on the target was about 1-2 mm for the SR beam energies of interest. For the suppression of the



FIG. 2: Photographs of the von Hamos spectrometer as installed at the ESRF beamline ID21 (top) and BM5 (bottom). Due to the higher x-ray beam energies employed at BM5, no evacuated pipe was needed to connect the spectrometer chamber to the exit window of the beam-line (pipe emerging from the wall on the right). One sees that at BM5 the spectrometer chamber was rotated by 180 deg. around a vertical axis with respect to the set-up employed at ID21.

undesired upper-harmonics a Si mirror, tilted by 2.5 mrad with respect to the beam direction, was installed in front of the spectrometer. An harmonic rejection of the order of 10^{-3} was obtained. At BM5, SR beam energies between 7150 eV and 11150 eV were used. At these energies, the absorption of SR in atmospheric air along the 2 m long beam path between the beam-line exit window and the spectrometer entrance beam-port being acceptable, no additional vacuum pipes were installed (see Fig. 2). This made easier the insertion of the upper-harmonics rejection device.

The solid targets consisted of 25-mm-high \times 5-mm-wide \times 0.025-mm-thick metallic foils of

natural elements. The specified purity of the foils was better than 99.9% except for Ba which had a purity of 99.0%. The Xe target consisted of a cylindrical cell filled up with 99.999% pure xenon gas. The cell was 10 mm in diameter with a 3.6 mg/cm²-thick black KaptonTM wall. Black KaptonTM was chosen to protect the CCD detector from the visible light emitted by the irradiated Xe. The gas pressure was optimized to give the highest possible intensity for the measured L_3 x-ray lines. The best value was found to be 0.53 bar.

III. DATA ANALYSIS

In the von Hamos slit-geometry the target part viewed through the slit by the 14-mm wide crystal area (half of the CCD length) contributing to the x-ray reflection depends on the coordinate (in the dispersive direction) of the point where the reflection takes place. As a consequence, the shape of the measured spectra can be altered by the beam intensity profile if the latter is inhomogeneous. For this reason, the intensity profile of the synchrotron radiation at the target position was determined for each measurement and the spectra were corrected off-line to account for the measured inhomogeneities. The changes in the L_3 - $M_{4,5}$ and L_3 - M_1 transition widths resulting from these corrections, however, did not exceed 5%. The beam profiles were determined with the spectrometer itself by measuring an intense x-ray transition taken as reference at different positions of the target along an axis parallel to the SR radiation beam direction. As the slit-crystal direction remained unchanged in these measurements (crystal and CCD positions were kept fixed), the variation of the reference x-ray line intensity as a function of the target position reflected the horizontal distribution of the beam

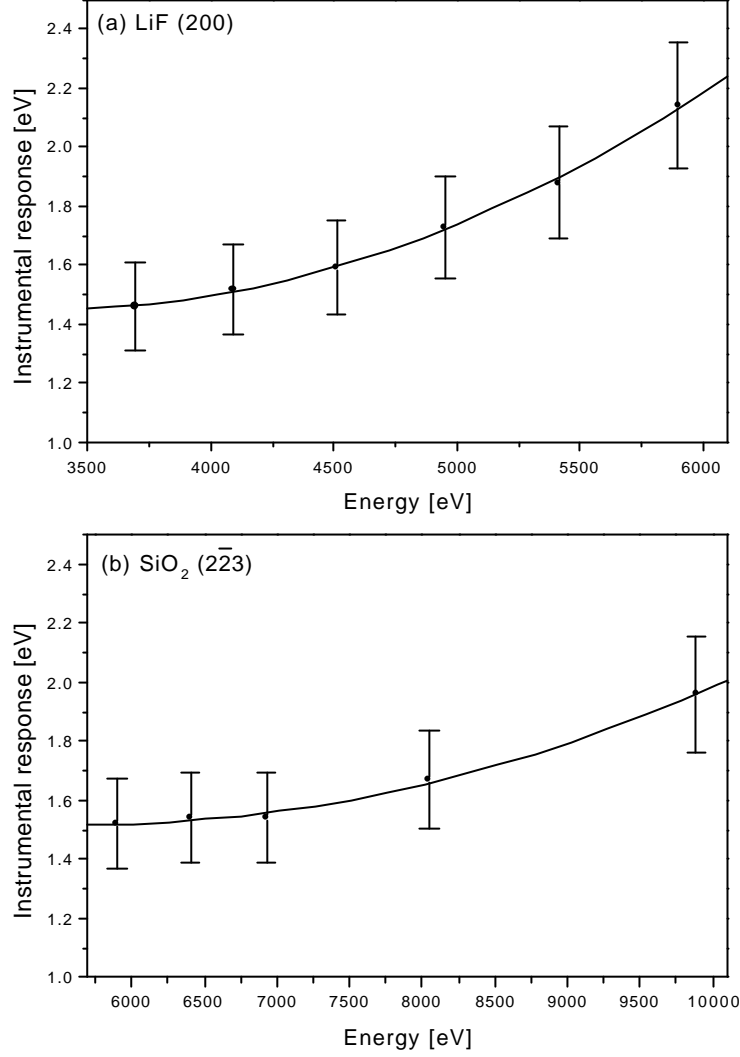


FIG 3: Energy dependence of the instrumental response of the von Hamos spectrometer equipped with the (a) LiF (200) crystal (b) SiO₂ ($\bar{2}2\bar{3}$) crystal.

intensity on the target. Most measured beam profiles could be well reproduced with single Gauss functions. However, some asymmetric profiles had to be fitted using up to 6th order polynomials.

The energy calibration of the spectrometer and the determination of the instrumental response were performed by measuring the $K\alpha_1$ x-ray lines of several 3d metals with $20 \leq Z \leq 32$. To avoid a broadening of the $K\alpha_1$ transitions by unresolved M satellite structures resulting from M -shell shake processes, the calibration targets were irradiated using SR photons with energies just above the K -

shell ionization thresholds. The natural linewidths and energies of the K transitions were taken from Refs.[2,19], respectively. It was found that for both crystals the instrumental response could be well reproduced by a Gaussian profile whose width (FWHM) varied as a function of the x-ray energy from 1.5 eV (at 3.7 keV) to 2.1 eV (at 5.9 keV) for the LiF crystal, and from 1.5 eV (at 5.9 keV) to 2.0 eV (at 9.9 keV) for the SiO₂ crystal (see Fig. 3). In order to account for the asymmetries observed in the low energy tails of the $K\alpha_1$ lines, a 10% uncertainty was assumed for the derived instrumental broadening. These asymmetries in the $K\alpha_1$ lines of 3d elements which have been already reported many

years ago [20-22] result from a splitting of the $2p$ electronic levels.

The observed K and L_3 x-ray transitions were analyzed by means of the least-squares-fitting computer program MINUIT [23], employing Voigt profiles to fit the observed x-ray lines. Voigtian functions were used because they correspond to the convolution of the Gaussian instrumental broadening with the Lorentzian representing the natural line shape of an x-ray transition. The natural widths of the x-ray lines of interest were extracted by keeping fixed in the fit the known Gaussian experimental broadening.

Except for Ir, the La_1 (L_3-M_5) and La_2 (L_3-M_4) transitions that are close in energy could be measured simultaneously, the two transitions being covered by a single CCD length. The intensities, energies and Lorentzian widths of the two transitions as well as the two parameters describing the linear background were let free in the fitting procedure whereas the instrumental broadenings were kept fixed at the values determined from the interpolation curves represented in Fig. 3. For illustration, the fitted $L_3-M_{4,5}$ spectra of Pr, Gd and Yb are presented in Fig. 4. The asymmetries occurring on the left sides of the Pr and Gd La_1 lines are certainly due to a multiplet splitting of the $3d_{5/2}$ levels as a result of the interaction between the $3d$ hole and the unfilled $4f$ level. This problem will be addressed in more details in Sect. 4.

Two examples of fitted L_3-M_1 transitions are presented in Fig. 5. As for the $L_3-M_{4,5}$ lines, all parameters were let free in the fits except the known instrumental resolutions. One sees from

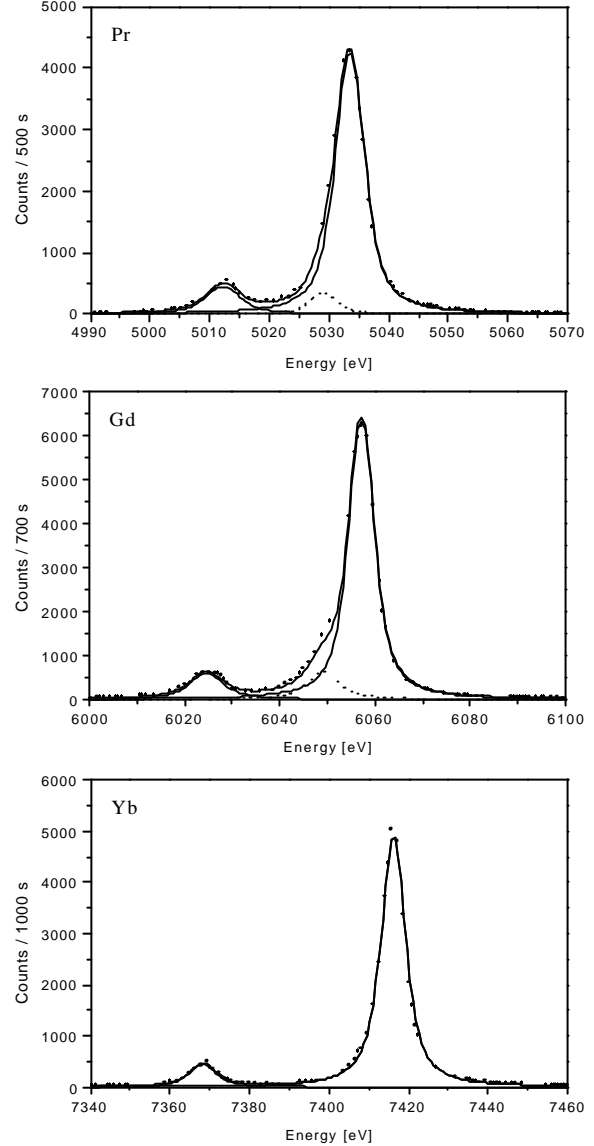


FIG 4: High-resolution $L_3-M_{4,5}$ x-ray emission spectra of Pr, Gd and Yb. Due to the multiplet splitting of the $3d_{5/2}$ levels, asymmetries are observed on the low-energy sides of the La_1 lines of Pr and Gd. These asymmetries were fitted using additional Lorentzians (dotted lines). For Yb that has a closed $4f$ subshell no asymmetry was observed.

Fig. 5 that both lines are symmetric and that they could be fitted with a single Voigt profile. It seems thus that the asymmetry observed in the La_1 line of Gd (see Fig. 4) does not affect the Ll line. Actually, as shown by MCDF calculations, the multiplet splitting effect is also present in Ll x-ray lines of lanthanides but the scatter of the components is less

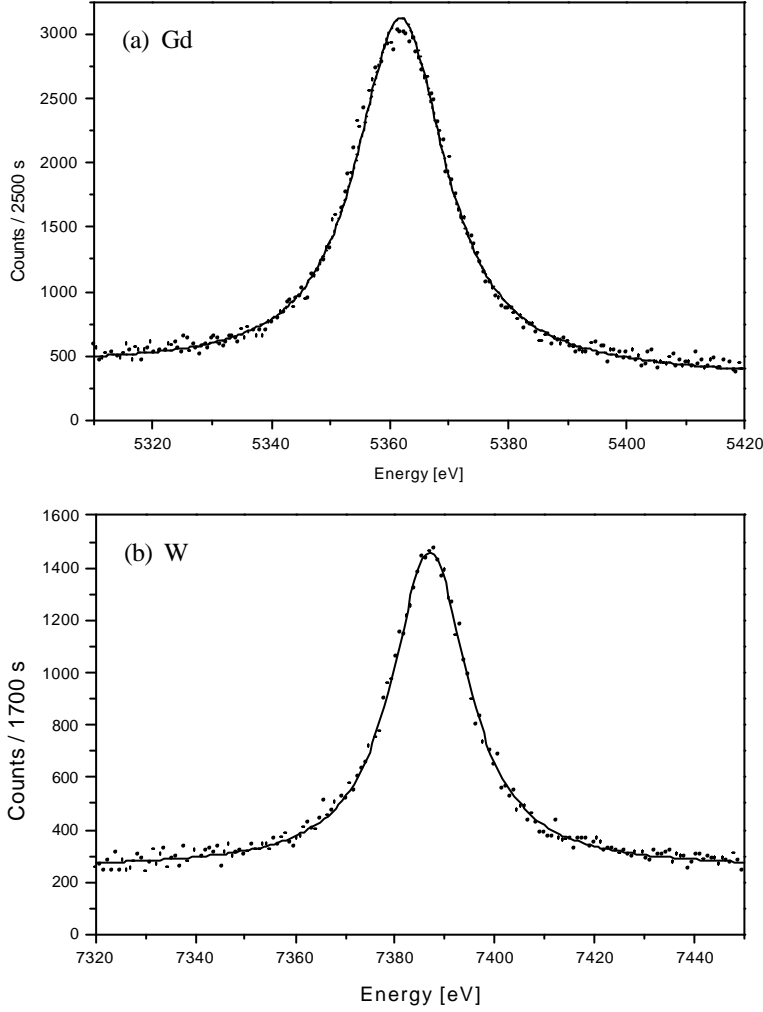


FIG. 5: High- resolution L_3-M_1 x-ray emission lines of Gd and W. The Gd spectrum was measured at the beamline ID21 with the LiF (200) crystal, the W spectrum at BM5 with the SiO_2 ($\bar{2}\bar{2}3$) crystal. The solid lines correspond to the fitted profiles. Both spectra were corrected beforehand to account for the inhomogeneities of the beam intensity distribution.

pronounced than for $L\alpha$ lines and partly smeared out by the bigger natural width of the transitions. This is confirmed by the fact that for some elements (mainly La and Nd) a small asymmetry was also observed in the L_3-M_1 transitions. The asymmetries were accounted for in the fits by using a second Voigtian. However, the Lorentzian widths of the main Voigtian in the one- and two-component fits were found to be consistent within the quoted uncertainties.

IV. RESULTS AND DISCUSSION

A. Transition energies

The energies of the measured L_3-M_1 , L_3-M_4 , and L_3-M_5 x-ray emission lines are given in Tables I, II and III, respectively. The calibration in energy of the von Hamos spectrometer was determined from measurements of the $K\alpha$ x-ray lines of Ca, Sc, Ti, V, Mn, Fe, Co, Cu and Ge whose energies were derived from the wavelengths listed in the table of Bearden [19]. Since the latter values are given in the \AA^* scale, they were corrected by the conversion factor $1.0000150 \text{ \AA}/\text{\AA}^*$ and then converted to

energies using the energy-wavelength product $V\lambda=12398.419 \text{ eV}\cdot\text{\AA}$. The two conversion factors were computed from the 1998 CODATA recommended values [24]. The uncertainties quoted by Bearden being probable errors (50% confidence limits), they were expanded by 1.48 to obtain standard deviation errors (67% confidence limits). The so-determined reference energies and associated errors are given as footnotes in Table I.

The numbers in parentheses are the uncertainties in the last digit(s) of the respective values. They correspond to 1- σ errors originating from the fits and energy calibration of the spectrometer. For any asymmetric line that was fitted with several Voigtian profiles, the quoted energy concerns the most intense component. In this case, the sensitivity of the main component energy on the number of Voigtians used to reproduce the asymmetry was

Table I: *Energies of the L_3 - M_1 transitions. Present results are compared to the transition energies reported by Bearden [19] and values derived from differences of the binding energies given by Bearden and Burr [25] and Storm and Israel [26]. Values from [19] were deduced from Bearden's transition wavelengths as indicated in the text. Probable errors quoted in [19] and [25] were multiplied by 1.48 to get 1- σ errors. The bigger uncertainties quoted for Xe, Gd and Tb originate principally from the energy calibration of the spectrometer, that of Yb from the beam intensity profile.*

| Z | Present | Ref. [19] | Ref. [25] | Ref. [26] |
|-----------------------------|-------------|-------------|-------------|-----------|
| $^{54}\text{Xe}^{\text{a}}$ | 3638.81(27) | | | 3639 |
| $^{56}\text{Ba}^{\text{a}}$ | 3955.65(17) | 3954.2(4) | 3954.4(7) | 3956 |
| $^{57}\text{La}^{\text{a}}$ | 4119.09(19) | 4124.5(6.1) | 4121.4(7) | 4121 |
| $^{59}\text{Pr}^{\text{a}}$ | 4458.51(15) | 4453.3(1.0) | 4453.3(1.3) | 4459 |
| $^{60}\text{Nd}^{\text{a}}$ | 4631.93(16) | 4633.2(1.0) | 4632.6(1.2) | 4633 |
| $^{62}\text{Sm}^{\text{a}}$ | 4990.64(16) | 4994.7(1.2) | 4993.4(1.4) | 4993 |
| $^{64}\text{Gd}^{\text{b}}$ | 5360.84(34) | 5362.1(7) | 5362.0(9) | 5362 |
| $^{65}\text{Tb}^{\text{b}}$ | 5552.35(29) | 5546.9(7) | 5546.0(1.1) | 5551 |
| $^{66}\text{Dy}^{\text{b}}$ | 5744.01(22) | 5743.2(3) | 5743.3(8) | 5744 |
| $^{67}\text{Ho}^{\text{b}}$ | 5939.60(18) | 5943.6(8) | 5942.8(1.1) | 5942 |
| $^{70}\text{Yb}^{\text{c}}$ | 6548.17(31) | 6545.6(3) | 6545.5(8) | 6545 |
| $^{74}\text{W}^{\text{c}}$ | 7386.60(12) | 7387.9(7) | 7387.2(7) | 7384 |
| $^{77}\text{Ir}^{\text{c}}$ | 8042.94(11) | 8045.9(2) | 8041.5(2.6) | 8042 |

^{a)} Measured at the beamline ID21 with the LiF (200) crystal using for the spectrometer calibration the following $K\alpha$ energies (adjusted Bearden's values): 3691.72(5) eV (Ca), 4090.61(20) eV (Sc), 4510.89(5) eV (Ti), 4952.24(6) eV (V), 5414.78(7) eV (Cr) and 5898.81(4) eV (Mn).

^{b)} Measured at the beamline ID21 with the SiO_2 ($2\bar{2}3$) crystal. $K\alpha$ energies employed for the spectrometer calibration: 5898.81(4) eV (Mn), 6403.91(4) eV (Fe) and 6930.39(5) eV (Co).

^{c)} Measured at the beamline BM5 with the SiO_2 ($2\bar{2}3$) crystal. $K\alpha$ energies employed for the spectrometer calibration: 5898.81(4) eV (Mn), 6403.91(4) eV (Fe), 8047.86(2) eV (Cu) and 9886.52(11) eV (Ge).

Table II: Same as Table I but for the L_3 - M_4 transitions. For Ir the transition was not measured.

| Z | Present | Ref. [19] | Ref. [25] | Ref. [26] |
|-----------------------------|-------------|-------------|-------------|-----------|
| $^{54}\text{Xe}^{\text{a}}$ | 4098.42(16) | | | 4096 |
| $^{56}\text{Ba}^{\text{a}}$ | 4451.37(14) | 4450.8(1) | 4450.9(6) | 4453 |
| $^{57}\text{La}^{\text{a}}$ | 4634.06(15) | 4634.3(1) | 4634.2(8) | 4636 |
| $^{59}\text{Pr}^{\text{a}}$ | 5012.59(16) | 5013.7(9) | 5013.2(1.1) | 5013 |
| $^{60}\text{Nd}^{\text{a}}$ | 5207.41(14) | 5207.8(1.0) | 5208.0(1.1) | 5207 |
| $^{62}\text{Sm}^{\text{a}}$ | 5607.15(14) | 5608.5(1) | 5610.2(1.4) | 5610 |
| $^{64}\text{Gd}^{\text{b}}$ | 6024.93(17) | 6025.0(9) | 6025.6(1.1) | 6026 |
| $^{65}\text{Tb}^{\text{b}}$ | 6238.81(14) | 6238.1(9) | 6239.0(1.1) | 6240 |
| $^{66}\text{Dy}^{\text{b}}$ | 6456.96(14) | 6457.8(2) | 6457.6(1.2) | 6458 |
| $^{67}\text{Ho}^{\text{b}}$ | 6678.79(23) | 6679.7(1.1) | 6679.6(1.2) | 6680 |
| $^{70}\text{Yb}^{\text{c}}$ | 7367.67(12) | 7367.5(3) | 7367.3(8) | 7366 |
| $^{74}\text{W}^{\text{c}}$ | 8334.33(20) | 8335.4(2) | 8335.2(6) | 8333 |

a),b),c) see Table I.

probed and the resulting additional uncertainty included in the reported error. The same holds for the corrections made to account for the inhomogeneities of the beam intensity profile. Further sources of uncertainties inherent to the von Hamos spectrometer are included in the energy calibration errors.

Present results were compared to the transition energies derived from Bearden's wavelengths [19], using the re-adjustment method described before, and from differences of the binding energies given by Bearden and Burr [25] and Storm and Israel [26]. As shown in Tables II and III, a satisfactory agreement with Bearden and Burr's values is generally found for the L_3 - $M_{4,5}$ transitions. The same holds for the comparison with the values derived from [26] if one assumes uncertainties of about 1.5 eV for Storm and Israel's results. In this case, however, a significant deviation of about 3 eV is observed for Sm. As this 3 eV-difference is found for the three L_3 - M_1 , L_3 - M_4 and L_3 - M_5 transitions, it can be concluded that the binding energy quoted by Storm and Israel for the L_3 -subshell of Sm is too big by approximately 3 eV. L_3 - M_4 and L_3 - M_5 transition energies from

Bearden's paper [19] are similar to those derived from Ref. [25] but due to their smaller uncertainties, about 50% of the values are not consistent with the results obtained in the present work. Actually, as our energies are based on $K\alpha_1$ x-ray wavelengths from the same reference, it seems that the K and L x-ray energies reported by Bearden are not self-consistent, probably because the quoted errors are too small.

For the L_3 - M_1 transitions that are weaker, a poorer agreement is found between our results and the three sets of values derived from Refs. [19], [25] and [26]. Deviations ranging from +5.4 eV (Tb) to -5.4 eV (La) are for instance observed with Bearden's energies [19] which are almost all inconsistent with our results. Similar deviations are found with values derived from Bearden and Burr's table, even if in this case the differences are in general somewhat less pronounced. Storm and Israel's data are closer to our results. About 70% of their values are indeed consistent with ours. The largest differences are observed for Sm (-2.5 eV), Ho (-2.4 eV), Yb (+3.2 eV) and W (+2.6 eV). As an agreement within a range of about 1 eV is found for the L_3 - $M_{4,5}$ transitions, the discrepancies observed in the case of the L_3 - M_1 transitions indicate that the M_1 -

Table III: Same as Table I but for the L_3 - M_5 transitions. The bigger uncertainties quoted for Dy and especially Ho are related to the asymmetric profiles of the transitions, that of Ir to the calibration.

| Z | Present | Ref. [19] | Ref. [25] | Ref. [26] |
|-----------------------------|-------------|-------------|-------------|-----------|
| $^{54}\text{Xe}^{\text{a}}$ | 4111.11(15) | 4110.0(4) | 4109.9(9) | 4110 |
| $^{56}\text{Ba}^{\text{a}}$ | 4466.80(13) | 4466.3(1) | 4466.3(6) | 4467 |
| $^{57}\text{La}^{\text{a}}$ | 4650.92(15) | 4651.1(1) | 4651.0(8) | 4652 |
| $^{59}\text{Pr}^{\text{a}}$ | 5033.82(15) | 5033.8(6) | 5033.3(1.1) | 5033 |
| $^{60}\text{Nd}^{\text{a}}$ | 5230.55(13) | 5230.5(7) | 5230.2(1.1) | 5230 |
| $^{62}\text{Sm}^{\text{a}}$ | 5635.22(12) | 5636.1(8) | 5636.0(1.2) | 5638 |
| $^{64}\text{Gd}^{\text{b}}$ | 6057.49(16) | 6057.4(9) | 6057.8(1.1) | 6058 |
| $^{65}\text{Tb}^{\text{b}}$ | 6274.51(12) | 6272.9(9) | 6272.8(1.2) | 6274 |
| $^{66}\text{Dy}^{\text{b}}$ | 6495.41(27) | 6495.3(2) | 6495.2(8) | 6495 |
| $^{67}\text{Ho}^{\text{b}}$ | 6721.90(37) | 6719.9(1.1) | 6719.7(1.3) | 6721 |
| $^{70}\text{Yb}^{\text{c}}$ | 7415.82(11) | 7415.8(3) | 7415.8(8) | 7415 |
| $^{74}\text{W}^{\text{c}}$ | 8397.18(10) | 8397.7(2) | 8397.6(6) | 8395 |
| $^{77}\text{Ir}^{\text{c}}$ | 9174.30(23) | 9175.2(3) | 9174.8(6) | 9175 |

^{a),b),c)} see Table I.

subshell binding energies quoted in [25] and, to a smaller extent, in [26] are probably incorrect. In several cases, they are also inconsistent. For instance for Pr and Tb, Bearden and Burr give 3s binding energies of 1511.0 ± 0.8 eV and 1967.5 ± 0.6 eV, respectively, which both do not agree with the values of 1505 eV and 1963 eV reported by Storm and Israel.

Because modern data concerning core-level energies for the elements investigated in the present study are scarce, we are not in a position to discuss in detail the observed deviations. However for Xe ($Z=54$), relatively recent XES data were published for the L_3 - M_1 and L_3 - M_5 transitions [7]. Energies of 3636.9 ± 0.3 and 4110.18 ± 0.04 eV, respectively, were obtained that differ by -1.7 eV and -0.8 eV from our results. As we do not have enough detailed information about the method employed in that experiment for the determination of the absolute energies (the latter were probably derived from the known crystal spacing constant and measured Bragg angles), it is hard to draw a definitive conclusion about these surprising deviations of about $4\text{-}\sigma$. In our experiment, the

gaseous Xe target was viewed by the crystal through the same slit as the metallic foils employed to calibrate the spectrometer and the slit position was kept fixed during the measurements. As a consequence, if the energies reported in [7] are correct, then the observed deviations of our results can only originate from errors of about +1.7 eV, respectively +0.8 eV, in the Ca, respectively Sc, $K\alpha_1$ transition energies of Bearden. In our opinion, however, this assumption is rather unlikely, many measurements having proven that Bearden's $K\alpha_1$ energies of 3d transition metals are reliable within ± 0.1 eV. In addition, the difference between the M_1 and M_5 binding energies of Xe as deduced from XPS measurements is 472.3 eV [27], a value which coincides with the energy difference between the L_3 - M_1 and L_3 - M_5 transitions found in the present work (472.3 ± 0.4 eV) but is not consistent with the difference (473.3 ± 0.3 eV) derived from the transition energies reported in [7]. Finally, the fact that the L_3 - M_1 and L_3 - M_5 energies given in [7] are smaller than ours is also intriguing since these data were obtained from measurements using an x-ray tube for the sample irradiation. As in XES measurements employing x-ray tubes for the target

Table IV: Lorentzian widths in eV of the photoinduced L_3-M_5 and L_3-M_1 x-ray emission lines.

| Z | $L_3-M_5 (La_1)$ | | | $L_3-M_1 (Ll)$ | | |
|------------------|-------------------|-------|-------|----------------|-------|-------|
| | Linewidth | Error | | Linewidth | Error | |
| | | Fit | Total | | Fit | Total |
| ^{54}Xe | 3.12 | 0.13 | 0.15 | 12.09 | 0.16 | 0.29 |
| ^{56}Ba | 3.02 | 0.18 | 0.22 | 12.13 | 0.19 | 0.36 |
| ^{57}La | 3.15 | 0.13 | 0.32 | 12.13 | 0.12 | 0.46 |
| ^{59}Pr | 3.84 | 0.16 | 0.31 | 15.22 | 0.19 | 0.25 |
| ^{60}Nd | 3.87 | 0.20 | 0.35 | 15.80 | 0.19 | 0.48 |
| ^{62}Sm | 4.57 | 0.22 | 0.34 | 17.20 | 0.24 | 0.51 |
| ^{64}Gd | 4.72 | 0.22 | 0.45 | 17.35 | 0.36 | 0.45 |
| ^{65}Tb | 5.17 | 0.20 | 0.47 | 17.17 | 0.26 | 0.65 |
| ^{66}Dy | 5.03 | 0.22 | 0.46 | 16.44 | 0.23 | 0.45 |
| ^{67}Ho | 3.83 ^a | - | 1.00 | 14.53 | 0.29 | 1.45 |
| ^{70}Yb | 5.59 | 0.18 | 0.20 | 16.72 | 0.27 | 1.67 |
| ^{74}W | 6.47 | 0.17 | 0.33 | 17.73 | 0.34 | 0.41 |
| ^{77}Ir | 7.86 | 0.31 | 0.37 | 18.39 | 0.29 | 0.38 |

^avalue extracted from HWHM (see text)

fluorescence production the centroids of L_3 x-ray lines are usually shifted toward higher energy as a result of unresolved N -satellite structures due to the CK decay of L_1 and L_2 vacancies, one would indeed expect the results quoted in [7] to be bigger than ours and not the contrary as observed. To clarify this point, x-ray tube based measurements of the L_3-M_1 and L_3-M_5 transitions of Xe (the lightest investigated element) and Ir (the heaviest one) were performed in Fribourg, using the same spectrometer as the one employed at ESRF and the same calibration sources. Energies of 3639.31(29) eV and 4111.61(15) eV were obtained for Xe that are both 0.50 eV bigger than the values found in the ESRF experiment. Similarly, for Ir, energies bigger by 1.13 eV (Ll transition) and 1.28 eV (La_1 transition) were found. Results from the two elements confirmed thus the expected positive energy shifts.

B. Transition widths

The natural linewidths of the L_3-M_5 and L_3-M_1 transitions obtained in the present work are listed in Table IV. The widths of the L_3-M_4 transitions are not reported because they were not employed to derive the M_1 level widths of interest. Although in most cases the fitted widths of the La_1 and La_2 transitions were found to be consistent within the combined experimental errors, we renounced to use the La_2 widths in view of their significantly larger uncertainties.

For the L_3-M_5 transitions, the principal contribution to the total uncertainty originates from the error matrix of the fitting procedure. For the instrumental broadening (see Fig. 3) an uncertainty of 10% was assumed. The latter as well as uncertainties related to the corrections for the inhomogeneities of the beam intensity profile are included in the total errors quoted in Table IV. Furthermore, as mentioned before, for several rare-earth elements asymmetries were observed on the

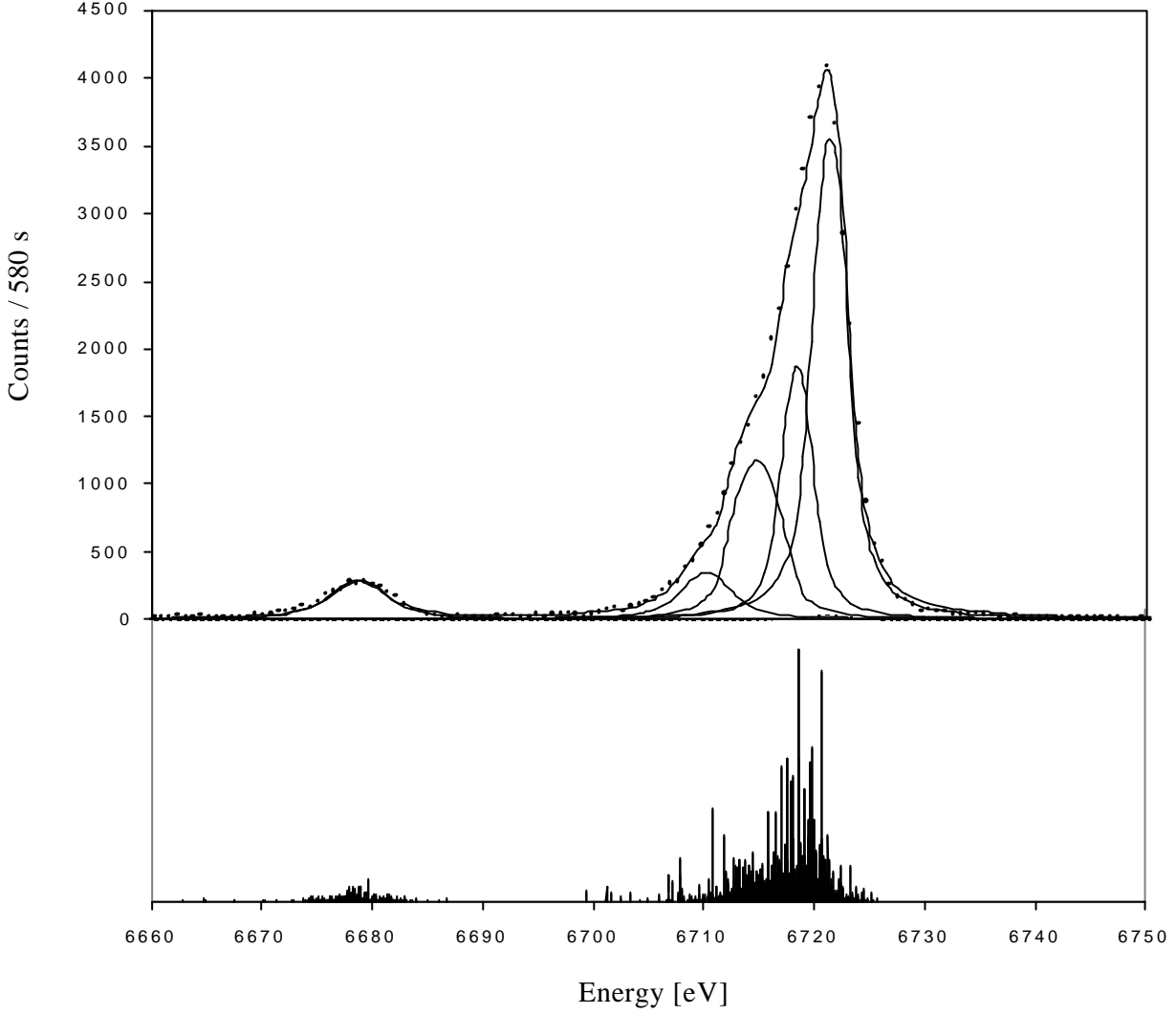


FIG 6: $L\alpha$ (L_3 - $M_{4,5}$) spectrum of Ho. In the $L\alpha_1$ transition, the thin solid lines correspond to the four Voigtians used in the fit to reproduce the strong asymmetry of the line. The asymmetry was explained by a multiplet splitting of the $3d_{5/2}$ level. The lower part of the figure shows the results of the MCDF calculations (stick spectra).

low-energy sides of the L_3 - M_5 transitions. In these cases, the transition widths were derived from the FWHM's of the Lorentzians corresponding to the main components. The sensitivity of these widths on the method employed to fit the asymmetries was probed. The deduced uncertainties are also included in the total errors of Table IV.

The asymmetric profiles observed in the L_3 - M_5 transitions of most investigated rare-earth elements are related to the partially filled $4f$ shell. The

exchange interaction between the $4f$ electrons and the $3d_{5/2}$ electrons splits the M_5 level. Actually, similar splitting effects have been observed in the $4d_{3/2}$ and $4d_{5/2}$ levels of rare-earth metals whose L_3 - $N_{4,5}$ and L_2 - N_4 transitions present analogous asymmetric profiles [28,29], in $2p$ levels of $3d$ elements for which the $K\alpha_{1,2}$ x-ray emission lines cannot be reproduced in general by single Lorentz functions [20-22], $4p$ levels of $4d$ elements [30] and $5p$ of $5f$ elements [14]. As in lanthanide metal crystals the two $6s$ electrons and one $4f$ electron are

involved in the atomic binding, the atomic core of these elements is trivalent, except for Yb and Eu which are generally assumed to be divalent [31]. In the La ($[\text{Xe}]5d6s^2$) crystal, the two $6s$ electrons and the $5d$ electron participate in the crystal bonding leaving the atom with a closed electronic shell configuration. Similarly, due to the delocalization of the two $6s$ electrons, the divalent atomic core of Yb is characterized by a closed electronic configuration ($[\text{Xe}]4f^{14}$). Thus, no asymmetry is expected for the L_3 - M_5 transitions of La and Yb. This was confirmed by our measurements and the La and Yb La_1 lines could be fitted with a single Voigtian each. The L_3 - M_5 transitions of the other investigated lanthanide elements (Pr, Nd, Sm, Gd, Tb, Dy and Ho) were fitted with two Voigt functions, one for the main component, another one for the low-energy asymmetry. The relative intensities of the Voigtians used to fit the asymmetries were found to increase as a function of atomic number up to $Z=67$. Similar variations with Z were observed by Salem and Scott [29] for the Lg (L_2 - N_4) and $Lb_{2,15}$ (L_3 - $N_{4,5}$) transitions of rare-earth elements, but in this case the maximum asymmetries were found at $Z=66$ and $Z=65$, respectively. In addition, the relative intensities of the Voigtians describing the asymmetries were found to be smaller in our work (L_3 - $M_{4,5}$ transitions) than in Salem and Scott's measurements (L_3 - $N_{4,5}$ and L_2 - N_4 transitions). This is, however, not surprising, the $4d$ - $4f$ exchange interaction being stronger than the $3d$ - $4f$ one [32].

This crude two-component splitting picture was found to be unsatisfactory for Ho for which the La_1 line shape could not be well reproduced by two juxtaposed Voigtians. Actually, as a result of the $3d$ - $4f$ interaction, the M_5 level may split into

many sublevels [33]. This multiplet splitting gives then rise to a complex structure for the L_3 - M_5 transition as the one observed for Ho. As shown in Fig. 6 four Voigtians were indeed needed to fit properly the La_1 line of Ho. In order to better understand the shape of this strongly asymmetric line, MCDF (multiconfiguration Dirac-Fock) calculations based on the MSAL (modified special average level) version [34] of the GRASP code [35] were performed [36]. Results of these calculations are given by the stick spectrum presented at the bottom of Fig. 6. As shown, the general trends of the experimental line shape are rather well predicted by the MCDF calculations. In particular, the low-energy asymmetry that was fitted with three Voigtians is in good agreement with the long tail of the MCDF distribution below 6720 eV. This four-component fit of the Ho La_1 line made extremely difficult the determination of the transition width. The method employed for the other rare-earth elements which consisted to identify the transition width with the FWHM value of the strongest component (which is only 2.25 eV for Ho) could not be applied to Ho. Similar difficulties were encountered by Fuggle *et al* [4] in photoelectron spectroscopy measurements. As the FWHM's of the observed peaks were found to be very sensitive to the asymmetries and precise form of the latter, Fuggle and coworkers used for the transition widths the half-widths-at-half-maximum (HWHM) associated to the low-binding-energy sides of the peaks. They found that these widths were not very sensitive to the degree of asymmetry but they simultaneously pointed out that this choice is questionable for lines having low lifetime broadenings as compared to the instrumental response. For the L_3 - M_5 transition of Ho a HWHM of 2.1 eV was found which gives a width of 4.2 eV

for the La_1 transition. Deconvoluting this value with the instrumental response (1.5 eV), a width of 3.8 eV was finally obtained for the Lorentz contribution. This result should, however, be considered with some reserve because the HWHM method, when applied to the La lines of the other measured lanthanide elements gives widths that exceed by 1-2 eV the values deduced from the FWHM of the strongest Voigtian. For this reason an increased uncertainty of 1 eV was assumed for the Ho L_3-M_5 transition width derived with the HWHM method.

As indicated in Table IV, errors for the L_3-M_1 transitions arising from the error matrix of the fitting procedure are in general not bigger than those obtained for the stronger L_3-M_5 transitions. This is due to the fact that the weaker transitions were measured with much longer acquisition times. The uncertainties related to the instrumental response and beam profile corrections are reflected in the differences between the fit errors and the total errors. The latter range between 2% and 4%. For Ho and Yb, however, for which no reliable beam profile corrections could be made because of instabilities in the synchrotron radiation beam, errors of 10% were assumed. For certain elements, additional uncertainties were considered that originate from the fit of the small structures observed on the high-energy sides of the Ll lines. As predicted by MCDF calculations [36], these structures are due to isolated transition components that have bigger energies than the majority of the components pertaining to the L_3-M_1 transition. Depending on the coupling between the $4f$ vacancies with the $2p$ hole in the initial state and with the $3s$ hole in the final state, several different

initial and final states do indeed exist which give rise to numerous transition components.

As mentioned in Sect. I, experimental data concerning the L_3-M_5 and especially L_3-M_1 transition widths are scarce for elements $54 \leq Z \leq 77$. To our knowledge, literature data are only available for Xe, W and Ir. For Xe, widths of 3.44 and 13.36 eV, respectively, were reported for the La and Ll transitions [7]. For Ir, values of 8.2 ± 0.2 and 18.0 ± 0.9 eV were obtained from PIXE measurements [8]. Except for the Xe L_3-M_1 transition, results from both sources are consistent with the values obtained in the present work. Further results were found for the L_3-M_5 transition of Ir. Whereas the value of 8.08 eV published by Williams [37] a long time ago is in fair agreement with our result, the more recent value of 7.22 ± 0.13 eV given by Amorin *et al.* [11] is not consistent with other existing data, ours included. For W, data are only available for the L_3-M_5 transitions. Values of 7.8 ± 0.4 eV [38], 7.0 ± 0.5 eV [39] and 6.6 ± 0.3 eV [40] were

TABLE V: Atomic-level widths in eV for the subshell L_3 . Our experimental results are compared with the recommended values of Campbell and Papp [2].

| Z | Present | Ref. [2] |
|------------------|-------------------|-----------------|
| $_{54}\text{Xe}$ | 2.52 ± 0.16 | 2.82 ± 0.28 |
| $_{56}\text{Ba}$ | 2.35 ± 0.23 | 3.02 ± 0.30 |
| $_{57}\text{La}$ | 2.45 ± 0.33 | 3.12 ± 0.31 |
| $_{59}\text{Pr}$ | 3.09 ± 0.32 | 3.27 ± 0.33 |
| $_{60}\text{Nd}$ | 3.09 ± 0.36 | 3.36 ± 0.34 |
| $_{62}\text{Sm}$ | 3.71 ± 0.35 | 3.53 ± 0.35 |
| $_{64}\text{Gd}$ | 3.77 ± 0.46 | 3.72 ± 0.37 |
| $_{65}\text{Tb}$ | 4.16 ± 0.48 | 3.80 ± 0.38 |
| $_{66}\text{Dy}$ | 3.97 ± 0.47 | 3.90 ± 0.39 |
| $_{67}\text{Ho}$ | 2.70 ± 1.01^a | 4.00 ± 0.40 |
| $_{70}\text{Yb}$ | 4.24 ± 0.24 | 4.00 ± 0.43 |
| $_{74}\text{W}$ | 4.77 ± 0.37 | 4.81 ± 0.48 |
| $_{77}\text{Ir}$ | 5.87 ± 0.42 | 5.24 ± 0.52 |

^avalue extracted from HWHM (see text).

obtained which are all bigger than our result but consistent within the combined uncertainties, except the first one.

C. Level widths

The L_3 atomic-level widths obtained in the present work are listed in Table V. They were determined from the differences between the linewidths of the L_3 - M_5 transitions given in Table IV and the recommended values of the M_5 level widths quoted by Campbell and Papp [2]. Our

results are also presented graphically in Fig. 7, which gives an overview of existing information about the level width of the subshell L_3 in the range $50 \leq Z \leq 80$. Except for Ho, a relatively good agreement is found between present results and the recommended values given in [2], the average deviation (0.29 eV) being similar to the average value of the quoted uncertainties (0.35 eV). The biggest deviations are found for Ba (-0.67 eV), La (-0.67 eV) and Ho (-1.30 eV). For Ba and La our results and those of Campbell and Papp [2] are not consistent within the combined errors. Because of

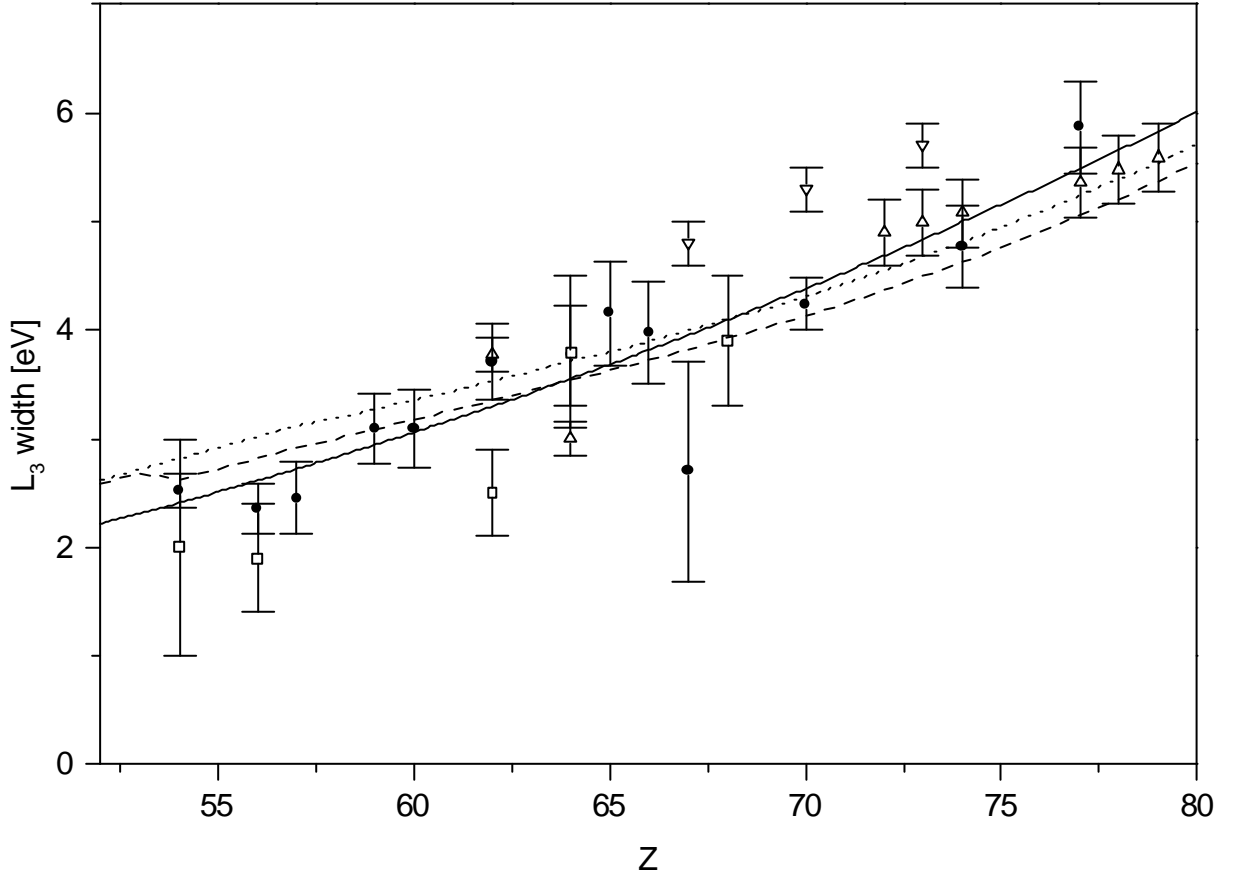


FIG. 7: Width L_3 versus atomic number Z . Black circles (\bullet) correspond to the results obtained in the present work. The solid line represents the least-squares fit to present results, the dotted line the recommended values of Campbell and Papp [2] and the dashed one results of independent-particle model calculations by Perkins et al [48]. Experimental data from different sources are also presented, using the following symbols: (∇) resonant Raman scattering results from Refs. [47,49], (\square) x-ray absorption edge values from Refs. [41-43], (\blacklozenge) results derived from Coster-Kronig transition probabilities from Refs. [44-46].

its uncertainty of about 40%, the width found for Ho (2.7 ± 1.0 eV) is consistent with the result quoted in [2] but markedly smaller than the latter. As mentioned in the preceding Sect., the Ho L_3 width depends strongly on the way the width of an asymmetric transition is defined. If we compare the value found for Ho with the L_3 widths of neighbor elements for which the asymmetry is less pronounced (see also Fig. 7), it seems that the HWHM method employed for Ho underestimates the real width.

L_3 widths deduced from x-ray absorption measurements [41-43] are consistent with our

TABLE VI: Atomic-level widths in eV for the subshell M_1 . Our experimental results are compared with the recommended values of Campbell and Papp [2].

| Z | Present | Ref. [2] |
|------------------|------------------|----------------|
| $_{54}\text{Xe}$ | 9.57 ± 0.33 | 10.6 ± 0.5 |
| $_{56}\text{Ba}$ | 9.78 ± 0.43 | 11.1 ± 2.0 |
| $_{57}\text{La}$ | 9.68 ± 0.56 | 11.4 ± 2.0 |
| $_{59}\text{Pr}$ | 12.13 ± 0.41 | 11.8 ± 2.0 |
| $_{60}\text{Nd}$ | 12.71 ± 0.60 | 12.0 ± 2.0 |
| $_{62}\text{Sm}$ | 13.49 ± 0.62 | 12.4 ± 2.0 |
| $_{64}\text{Gd}$ | 13.58 ± 0.64 | 12.8 ± 2.0 |
| $_{65}\text{Tb}$ | 13.01 ± 0.81 | 13.0 ± 2.0 |
| $_{66}\text{Dy}$ | 12.48 ± 0.65 | 13.2 ± 2.0 |
| $_{67}\text{Ho}$ | 11.83 ± 1.77 | 13.4 ± 2.0 |
| $_{70}\text{Yb}$ | 12.48 ± 1.78 | 13.9 ± 2.0 |
| $_{74}\text{W}$ | 12.96 ± 0.55 | 14.5 ± 2.0 |
| $_{77}\text{Ir}$ | 12.52 ± 0.51 | 14.8 ± 2.0 |

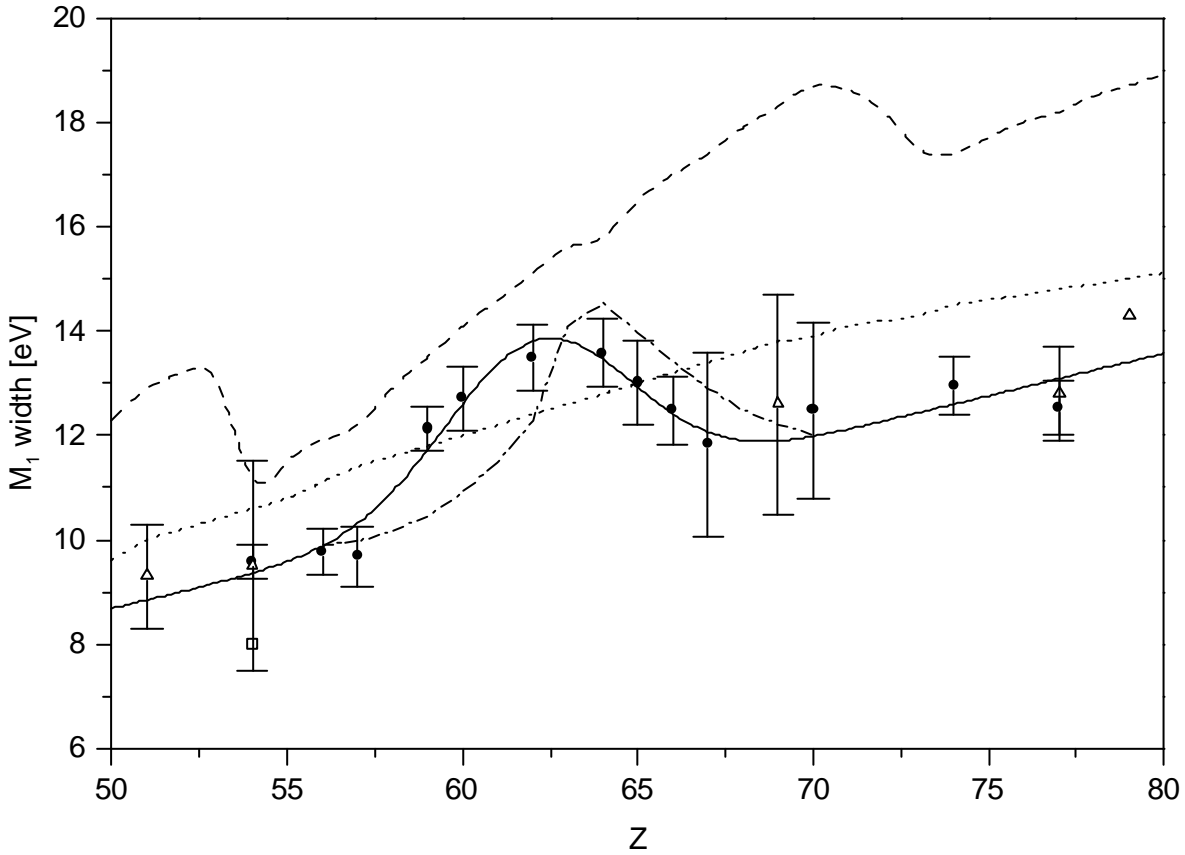


FIG 8: Width M_1 versus atomic number Z . Black circles (\bullet) correspond to the results obtained in the present work. The solid line represents the least-squares fit to present results, the dotted line the recommended values of Campbell and Papp [2], the dotted one results of independent-particle model calculations by Perkins et al [48], whereas the dashed-dotted line corresponds to the predictions computed within the splitting model described in the text. Several experimental data from different sources are also presented, using the following symbols: (\bullet) x-ray emission spectroscopy results from Refs. [6-9], (\square) value obtained from x-ray photoelectron spectroscopy data [50].

results, except for Sm for which a large discrepancy is observed with the result quoted in Ref. [42]. A good agreement is also found with results derived from Coster-Kronig transition probabilities [44,45], except for Gd for which a value of 3.0 ± 0.15 eV is reported [46]. In contrast to that, a poor agreement is found with values provided by the resonant Raman scattering technique, most of reported data being significantly bigger than our results. In particular, a large deviation is found for Yb between our result (4.24 eV) and the one given in [47] (5.3 eV).

The M_1 atomic-level widths are presented in Table VI together with the recommended values of Campbell and Papp [2]. They were determined from the differences between the linewidths of the L_3 - M_1 transitions listed in Table IV and the L_3 level widths determined in the present work (Table V). Obtained uncertainties vary between 3% and 6%, except for Ho and Yb for which the errors are about 13% (see second to last paragraph of Sect. IVB). Existing information about the M_1 widths is summarized graphically in Fig. 8. A least squares fit to the widths obtained in the present work (solid line) shows for lanthanides a resonant-like behavior, the values being in general bigger than the recommended ones of Campbell and Papp (dotted line). The deviation varies with Z , increasing first up to $Z \approx 64$, and then decreasing with growing Z . Outside this region, an opposite trend is observed, our results being significantly smaller than Campbell and Papp's values, but consistent with earlier x-ray emission spectroscopy data [6-9]. A similar behavior was found for the L_1 [16], N_1 and O_1 [15] level widths of rare-earth metals. The increased level widths observed in this region were explained by a multiplet splitting of

the $2s$, $4s$ and $5s$ levels which originates from the energy difference between the spin-up and spin-down final states of the ns electrons. We believe that the increased values observed for the M_1 widths in the lanthanide region arises from the same effect.

Assuming that the exchange interaction of the $3s$ hole in the initial state is larger or similar to the LS coupling energy of the $4f$ electrons and following the same approach as the one described in Refs [15,16], one can consider the transition L_3 - M_1 to consist of two components of equal width but slightly shifted in energy. If one neglects the moderate change of the wave functions with Z , the splitting energy dE can be written as follows:

$$dE(Z) = eS(Z)B_{M1}. \quad (1)$$

where S stands for the total spin of the $4f$ subshell, B_{M1} represents the binding energy of the $3s$ electrons and e is a scaling constant. In this picture, the intensity ratio of the two components is simply given by [15,16]:

$$\frac{I_1}{I_2} = \frac{S+1}{S} \quad (2)$$

where I_1 stands for the intensity of the higher-energy component.

To determine the splitting constant e , we refitted the L_3 - M_1 transitions of rare-earth elements with two components. The widths of the two Lorentzians were fixed at the same values. The latter were determined from the least squares-fit to our data outside the lanthanide resonance region (see Fig. 8). For each element, the intensity ratio between the two components was calculated with eq. (2) and then kept fixed at this value in the fitting procedure. For

illustration, the two-component fit of the L_3 - M_1 transition of Gd is depicted in Fig. 9. A comparison between Fig. 5 and Fig. 9 shows that both the one- and two-component fits reproduce well the experimental data. Actually, for most lanthanide elements, approximately equal chi squares were obtained for the one- and two-component fits.

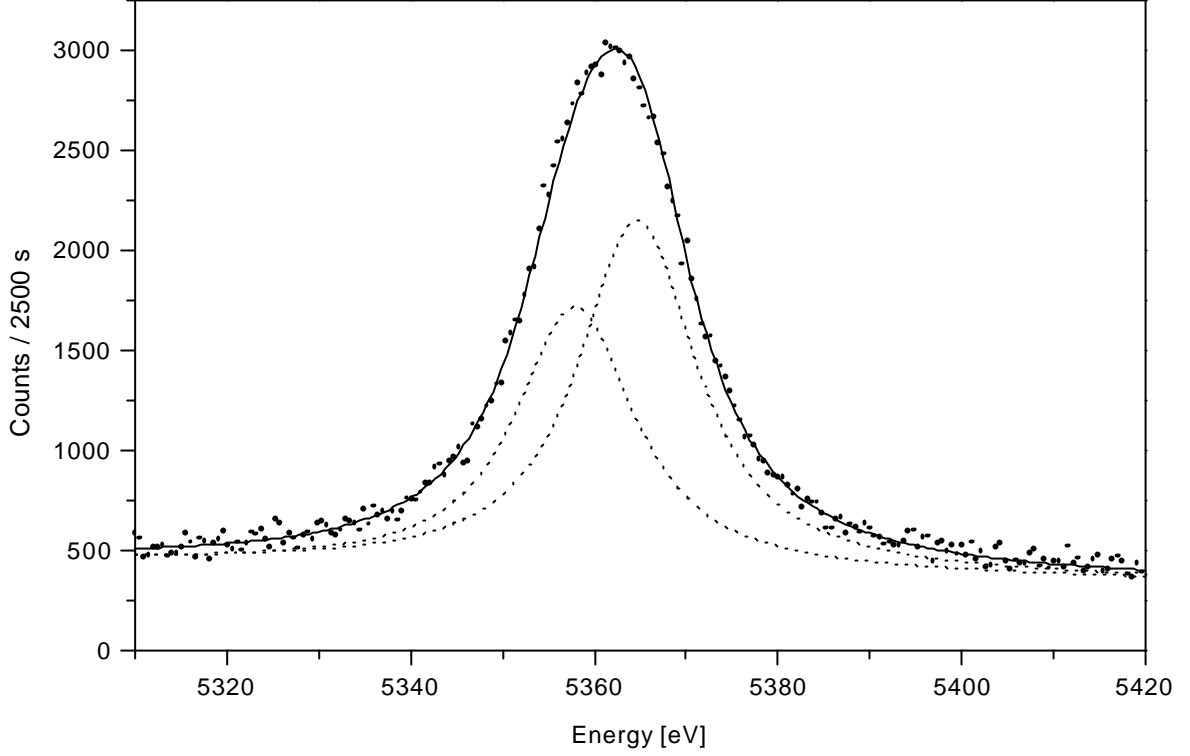
The variation of the splitting energy δE with Z was found to be similar to those observed in [15,16] for the $2s$, $4s$ and $5s$ levels. The splitting constant e was determined by means of a least-squares-fit method, using eq. (1), in which the binding energies B_{M_1} were taken from [51], and the energy shifts dE given by the two-component fits. A value $e=(9.4\pm3.9)\cdot10^{-4}$ was obtained. In order to probe the goodness of the splitting model, theoretical profiles of the L_3 - M_1 transitions were then constructed by summing two Lorentzians of equal widths (the same as the ones used in the two-component fits) whose relative intensities and energy differences were deduced from eqs. (1) and (2), using for e the above-mentioned value. Subtracting finally from the linewidths of the calculated theoretical profiles the L_3 widths determined in the present work (least-squares-fit values), we obtained the M_1 level widths represented by the dashed-dotted line of Fig. 8. As shown, the splitting model does not reproduce accurately the Z -dependent broadening of the M_1 level width in the lanthanide region. Significant deviations are indeed observed between the predictions of the splitting model and the experimental widths obtained in this study. In particular, one can see that the bump determined using the splitting picture is shifted towards higher- Z with respect to the experimental results as

if the assumed linear dependence of dE on S were too strong. This poor agreement between the splitting model and our data is also reflected in the large error ($\sim 40\%$) obtained for e . In our opinion, the observed discrepancies are related to the crude assumptions made in the model. In addition, it is interesting to point out that the two-component structure expected from the splitting picture is hardly seen in the MCDF stick spectra. The latter is probably smeared out by the numerous overlapping MCDF components which spread over the two sublevels.

V. CONCLUSION

High-resolution measurements of the L_3 - $M_{4,5}$ and L_3 - M_1 fluorescence x-ray lines of elements $54 \leq Z \leq 77$ were performed, using monochromatized synchrotron radiation for the irradiation of the targets. In order to avoid a line broadening by unresolved N -satellites, SR excitation energies just above the L_3 edges were chosen. Despite the difficulties encountered in the data analysis to fit the asymmetric profiles characterizing the La_i and Ll x-ray lines of some rare earth elements, precise transition energies and linewidths were obtained.

The experimental energies determined in the present work were compared to the transition energies quoted by Bearden and to the differences between the binding energies of atomic levels reported by Bearden and Burr and Storm and Israel. The comparison has shown that these old data which, despite their age, are currently employed as references have to be considered cautiously. Deviations of several eV were indeed observed, that are in many cases bigger than the quoted uncertainties. This remark applies particularly to the

FIG. 9: Two-component fit of the L_3 - M_1 transition of Gd.

L_3 - M_1 transitions for which deviations up to about 6 eV with Bearden's values were observed.

The L_3 level widths of the investigated elements were determined from the observed line widths of the L_3 - M_5 transitions, assuming for the M_5 level widths the values reported recently by Campbell and Papp. Except for Ho, results with a precision of 6%-13% were obtained that are in good agreement with Campbell and Papp's values and other existing experimental data. For Ho a markedly bigger uncertainty (30%) was found because of the strong asymmetry observed in the L_3 - M_5 transition of this rare-earth element.

The M_1 level widths represented the main objective of this study. They were determined from the observed line widths of the L_3 - M_1 transitions, using for the L_3 level widths the values obtained in the present work. A precision of 3%-6% could be

achieved except for Ho and Yb for which the total errors were estimated to be about 15% due to some uncontrolled instabilities of the SR beam during the measurements. Thus a significant improvement was obtained relative to Campbell and Papp's data whose precision ranges between 14% and 18%. Outside the lanthanide region, differences of about -2 eV were found between our results and the widths recommended by Campbell and Papp. In the lanthanide region, the M_1 level width followed a resonance curve, resulting in differences of up to 1 eV with values of Campbell and Papp. Actually, in this region the M_1 width was found to grow with the total spin of the open $4f$ subshell. Deviations up to 3 eV relative to the values one would have expected from the linear Z-dependence observed outside the rare-earth region were found for Sm and Gd. This broadening of the $3s$ level of lanthanides confirms similar observations made in previous measurements concerning the L_1 , N_1 and O_1 subshell widths of rare-

earth elements. In these former works, the observed width enhancements were explained by a splitting effect resulting from the coupling of the ns electron spin in the initial excited state with the total spin of the open $4f$ level. In the present work it was found that this crude splitting picture reproduces only qualitatively the observed broadenings. The experimental broadenings are indeed significantly underestimated by the model predictions for the lanthanide elements below Gd and somewhat overestimated above.

ACKNOWLEDGMENT

This work was supported by the Swiss National Science Foundation and the European Synchrotron Radiation Facility (ESRF). The authors would like to thank Dr. J. Susini and his collaborators of ID21 and Dr. A.K. Freund from the Optics Group for their support during the experiments. They wish also to thank Dr. M. Polasik from the University of Torun, Poland, for the MCDF calculations.

-
- [1] J.L. Campbell and T. Papp, X-Ray Spectrom. **24**, 307 (1995).
 - [2] J.L. Campbell and T. Papp, At. Data Nucl. Data Tables **77**, 1 (2001).
 - [3] M. Ohno, Phys. Rev. B **29**, 3127 (1984).
 - [4] J.C. Fuggle and S.F. Alvarado, Phys. Rev. A **22**, 1615 (1980).
 - [5] M. Ohno, J.-M. Mariot and C.F. Hague, J. Electron. Spectrosc. Relat. Phenom. **36**, 17 (1985).
 - [6] M. Ohno, P. Putila-Mantyla, and G. Graefe, J. Phys. B: At. Mol. Phys. **17**, 1747 (1984).
 - [7] M. Ohno and R.E. La Villa, Phys. Rev. A **45**, 4713 (1992).
 - [8] T. Papp, J.L. Campbell, J.A. Maxwell, J.X. Wang, and W.J. Teesdale, Phys. Rev. A **45**, 1711 (1992).
 - [9] F.K. Richtmeyer, S.W. Barnes, and E. Ramberg, Phys. Rev. **46**, 843 (1934).
 - [10] W. Meierkord, T. Blumke, M. Brussermann, J. Hofste, H. Menzebach, J.F. Pennings, Z. Stachura, W. Vollmer, J. Wigger, and B. Cleff, Z. Phys. D **18**, 75 (1991).
 - [11] P. Amorim, L. Salgueiro, F. Parente, and J.G. Ferreira, J. Phys. B: At. Mol. Opt. Phys. **21**, 3851 (1988).
 - [12] P.-A. Raboud, J.-Cl. Dousse, J. Hozowska and I. Savoy, Phys. Rev. A **61**, 012507 (2000).
 - [13] J. Merrill and J.W.M. DuMond, Annals Phys. **14**, 166 (1961).
 - [14] J. Hozowska, J.-Cl. Dousse and Ch. Rhême, Phys. Rev. A **50**, 123 (1994).
 - [15] R.L. Cohen, G.K. Werthein, A. Rosencwaig, and H.J. Guggenheim, Phys. Rev. B **5**, 1037 (1972).
 - [16] P.-A. Raboud, M. Berset, J.-Cl. Dousse, and Y.-P. Maillard, Phys. Rev. A **65**, 022512 (2002).
 - [17] J. Hozowska, J.-Cl. Dousse, J. Kern, and Ch. Rhême, Nucl. Instrum. Methods Phys. Res. A **376**, 129 (1996).

- [18] A.K. Freund, F. Comin, J.-L. Hazemann, R. Hustache, B. Jenninger, K. Lieb, and M. Pierre, Proc. SPIE Vol. **3448**, Crystal and Multilayer Optics, 144 (1998).
- [19] J.A. Bearden, Rev. Mod. Phys. **39**, 78 (1967).
- [20] J.A. Bearden and C.H. Shaw, Phys. Rev. **48**, 18 (1935).
- [21] L.G. Parratt, Phys. Rev. **50**, 1 (1936).
- [22] E.E. Wainstein, C.R. (Dokl.) Acad. Sci. URSS **40**, 102 (1943).
- [23] F. James and M. Roos, Comput. Phys. Commun. **10**, 343 (1975).
- [24] P.J. Mohr and B.N. Taylor, Rev. Mod. Phys. **72**, 351 (2000).
- [25] J.A. Bearden and A.F. Burr, Rev. Mod. Phys. **39**, 125 (1967).
- [26] E. Storm and H.I. Israel, Nucl. Data Tables **7**, 565 (1970).
- [27] *Photoemission in Solids I: General Principles*, edited by M. Cardona and L. Ley (Springer-Verlag, Berlin, 1978).
- [28] S.I. Salem, C.W. Schultz, B.A. Rabbani, and R.T. Tsusui, Phys. Rev. Lett. **27**, 477 (1971).
- [29] S.I. Salem and B.L. Scott, Phys. Rev. A **9**, 690 (1974).
- [30] J. Hoszowska and J.-Cl. Dousse, J. Phys. B: At. Mol. Opt. Phys. **29**, 1641 (1996).
- [31] J. Sugar, Phys. Rev. B **5**, 1785 (1972).
- [32] J.L. Dehmer, A.F. Starace, U. Fano, J. Sugar, and J.W. Cooper, Phys. Rev. Lett. **26**, 1521 (1971).
- [33] Ch. Gerth, K. Godehusen, M. Richter, P. Zimmermann, J. Schulz, Ph. Wernet, B. Sonntag, A.G. Kochur, and I.D. Petrov, Phys. Rev. A **61**, 022713 (2000).
- [34] M. Polasik, Phys. Rev. A **52**, 227 (1995).
- [35] K.G. Dyall, I.P. Grant, C.T. Johnson, F.A. Parpia, and E.P. Plummer, Comput. Phys. Commun. **55**, 425 (1989).
- [36] M. Polasik, private communication.
- [37] J.H. Williams, Phys. Rev. **45**, 71 (1934).
- [38] R. Diamant, S. Huotari, K. Hämäläinen, R. Sharon, C.C. Kao, and M. Deutsch, Phys. Rev. A **63**, 022508 (2001).
- [39] A.M. Vlaicu, T. Tochio, T. Ishizuka, D. Ohsawa, Y. Ito, T. Mukoyama, A. Nisawa, T. Shoji, and S. Yoshikado, Phys. Rev. A **58**, 3544 (1998).
- [40] B.G. Gokhale, S.N. Shukla, and N. Srivastava, Phys. Rev. A **28**, 858 (1983).
- [41] O. Keshki-Rahkonen, G. Materlik, B. Sonntag, and J. Tulkki, J. Phys. B: At. Mol. Phys., L121 (1984).
- [42] U. Arp, G. Materlik, M. Richter, and B. Sonntag, J. Phys. B: At. Mol. Phys. **23**, L811 (1990).
- [43] I. Arcon, A. Kodre, M. Stuhel, D. Glavic-Cindro, and W. Drube, Phys. Rev. A **51**, 147 (1995).
- [44] R. Stotzel, U. Werner, M. Sarkar, and W. Jitschin, J. Phys. B **25**, 2295 (1992).
- [45] U. Werner and W. Jitschin, Phys. Rev. A **38**, 4009 (1988).
- [46] T. Papp, J.L. Campbell, and S. Raman, Phys. Rev. A **58**, 3537 (1998).
- [47] K. Hamalainen, S. Manninen, S.P. Collins, and M.J. Cooper, J. Phys.: Cond. Matt. **2**, 5619 (1990).
- [48] S.T. Perkins, D.E. Cullen, M.H. Chen, J.H. Hubbell, J. Rathkopf, and J.H. Scofield, Tables and Graphs of Atomic Subshell Relaxation Data derived from the LLNL Evaluated Atomic Data Library, Lawrence Livermore National laboratory report UCRL-50400, Vol. **30** (1991).
- [49] K. Hamalainen, S. Manninen, P. Suortti, S.P. Collins, M.J. Cooper, and D. Laundy, J. Phys.: Cond. Matt. **1**, 5955 (1989).
- [50] S. Svensson, N. Martensson, E. Basilier, P.A. Malmqvist, U. Gelius, and K. Siegbahn, Phys. Scripta **14**, 141 (1976).
- [51] G. Williams, <http://xray.uu.se/hypertext/EbindEnergies.html>.

List of publications

Referred articles

L-shell shake processes resulting from 1s photoionization in elements 11 £Z£17.

O. Mauron, J.-Cl. Dousse, J. Hoszowska, J.P. Marques, F. Parente, and M. Polasik.

Published in Physical Review A **62**, 062508 (2000).

Double K+L shell ionization in Al, Ca, and Co targets bombarded by low-energy electrons.

O. Mauron and J.-Cl. Dousse.

Published in Physical Review A **66**, 042713 (2002).

Revisited L_3 and M_1 atomic-level widths of elements 54 £Z£77.

O. Mauron, J.-Cl. Dousse, S. Baechler, M. Berset, Y.-P. Maillard, P.-A. Raboud, and J. Hoszowska.

Accepted for publication in Physical Review A.

High-resolution measurements of Th and U L α -x-rays induced by O ions.

M. Pajek, D. Banas, D. Castella, D. Corminboeuf, J.-Cl. Dousse, Y-P. Maillard, O. Mauron, P.-A. Raboud, D. Chmielewska, I. Fijal, M. Jaskola, A. Korman, T. Ludziejewski, J. Rzakiewicz, Z. Sujkowski, M. Polasik, J. Hoszowska, and T. Mukoyama.

Published in Physica Scripta T **92**, 382 (2001).

Effect of L- and M- subshell ionization on the K x-ray diagram and hypersatellite lines of cadmium.

J. Rzakiewicz, D. Chmielewska, Z. Sujkowski, M. Berset, J.-Cl. Dousse, Y.-P. Maillard, O. Mauron, P.-A. Raboud, J. Hoszowska, M. Polasik, K. Slabkowska, and M. Pajek.

Published in Acta Physica Polonica B **33**, 415 (2002).

Energy-dependent KL double photoexcitation of argon.

P.-A. Raboud, M. Berset, J.-Cl. Dousse, Y.-P. Maillard, O. Mauron, J. Hoszowska, M. Polasik, and J. Rzakiewicz.

Published in Physical Review A **65**, 062503 (2002).

Study of Th M x-ray satellites and hypersatellites induced by energetic O and Ne ions.

M. Czarnota, M. Pajek, D. Banas, D. Chmielewska, J. Rzakiewicz, Z. Sujkowski, J.-Cl. Dousse, M. Berset, O. Maunon, Y.-P. Maillard, P.-A. Raboud, J. Hoszowska, M. Polasik, and K. Slabkowska.

Proc. of the 2nd Conference on Elementary Processes in Atomic Systems, Sept. 2002, Gdansk, Poland, Accepted for publication in Rad. Phys. Chem.

M-subshell ionization in near-central collisions of 20 MeV/amu carbon ions with molybdenum atoms.

J. Rzakiewicz, D. Chmielewska, Z. Sujkowski, M. Berset, J.-Cl. Dousse, Y.-P. Maillard, O. Maunon, P.-A. Raboud, M. Polasik, J. Hoszowska, M. Pajek.

Proc. of the 11th International Conference on the Physics of Highly Charged Ions, Sept. 2002, Caen, France, Accepted for publication in Nucl. Instrum. Meth. Phys. Res. B.

Observation of L x-ray satellites and hypersatellites in collisions of O and Ne ions with Mo and Pd.

M. Czarnota, M. Pajek, D. Banas, D. Chmielewska, J. Rzakiewicz, Z. Sujkowski, J.-Cl. Dousse, M. Berset, O. Maunon, Y.-P. Maillard, P.-A. Raboud, J. Hoszowska, M. Polasik, and K. Slabkowska.

Proc. of the 11th International Conference on the Physics of Highly Charged Ions, Sept. 2002, Caen, France, Accepted for publication in Nucl. Instrum. Meth. Phys. Res. B.

Conference abstracts

K+L double excitation in light elements bombarded by photons and low-energy electrons.

O. Maunon, J.-Cl. Dousse, J. Hoszowska, J.P. Marques, F. Parente, and M. Polasik.

Sixteenth International Conference on the Applications of Accelerators in Research & Industry (Denton, 2000), book of abstracts, p. 93.

L-shell shake processes resulting from 1s photoionization in elements 11 to 17.

J.-Cl. Dousse, J. Hoszowska, and O. Maunon.

18th International Conference on x-ray and Inner-Shell Processes, Chicago, Illinois, USA, 23-27 August 1999, book of abstracts p. B37.

High-resolution measurements of Th and U L-x-rays induced by O ions.

M. Pajek, D. Banas, D. Castella, D. Corminboeuf, J.-Cl. Dousse, Y.-P. Maillard, O. Maunon, P.-A. Raboud, D. Chmielewska, I. Fijal, M. Jaskola, A. Korman, T. Ludziejewski, J. Rzakiewicz, Z. Sujkowski, M. Polasik and J. Hoszowska.

Physics of Highly Charged Ions HCL 2000, Berkeley 2000, book of abstracts.

High-resolution study of thorium and uranium L x-ray spectra induced by impact with fast oxygen ions.

J.-Cl. Dousse, D. Banas, D. Castella, D. Chmielewska, D. Corminboeuf, I. Fijal, J. Hoszowska, M. Jaskola, A. Korman, T. Ludziejewski, Y.-P. Maillard, O. Mauron, M. Pajek, M. Polasik, P.-A. Raboud, J. Rzakiewicz, and Z. Sujkowski.

7th EPS Conf. on At. Mol. Phys. (Berlin, 2001), Europhys. Conf. Abs. **25** B, 47 (2001).

High-resolution study of L- and M-x-ray satellites excited in collisions of 360-MeV oxygen ions with heavy atoms.

D. Banas, M. Berset, D. Chmielewska, M. Czarnota, J.-Cl. Dousse, J. Hoszowska, Y.-P. Maillard, O. Mauron, T. Mukoyama, M. Pajek, M. Polasik, P.-A. Raboud, J. Rzakiewicz, and Z. Sujkowski.

XXII International Conference on Photonic, Electronic and Atomic Collisions ICPEAC 2001 (Santa Fe, 2001), book of abstracts.

Energy dependent KL double photoexcitation of argon.

P.-A. Raboud, M. Berset, J.-Cl. Dousse, J. Hoszowska, Y.-P. Maillard, O. Mauron, M. Polasik, J. Rzakiewicz.

12th ESRF Users Meeting (Grenoble, Feb. 13th, 2002).

High-resolution measurements of Zr, Mo and Pd L x-ray satellites excited by O and Ne ions.

M. Czarnota, M. Pajek, D. Banas, D. Chmielewska, J. Rzakiewicz, Z. Sujkowski, J.-Cl. Dousse, M. Berset, O. Mauron, Y.-P. Maillard, P.-A. Raboud, J. Hoszowska, M. Polasik, and K. Slabkowska.

34th Meeting of the European Group for Atomic Spectroscopy (EGAS), July 9-13 2002, Sofia, Bulgaria.

Energy dependent KL double photoexcitation of argon.

J.-Cl. Dousse, M. Berset, J. Hoszowska, O. Mauron, Y.-P. Maillard, P.-A. Raboud, M. Polasik, and J. Rzakiewicz.

International Workshop on Photoionization IWP2002 (Spring-8, Hyogo, Japan, Aug. 2002), book of abstracts p. SA04.

Observation of L x-ray (hyper)-satellites excited in collisions of O and Ne ions with mid-Z atoms.

M. Czarnota, M. Pajek, D. Banas, D. Chmielewska, J. Rzakiewicz, Z. Sujkowski, J.-Cl. Dousse, M. Berset, O. Mauron, Y.-P. Maillard, P.-A. Raboud, J. Hoszowska, M. Polasik, and K. Slabkowska.

11th International Conference on the Physics of Highly Charged Ions (HCI), Sept. 1-6, 2002, Caen, France.

M-subshell ionization in near-central collisions of 20 MeV/amu carbon ions with molybdenum atoms.

J. Rzakiewicz, D. Chmielewska, Z. Sujkowski, M. Berset, J.-Cl. Dousse, Y.-P. Maillard, O. Mauron, P.-A. Raboud, M. Polasik, J. Hoszowska, M. Pajek.

11th International Conference on the Physics of Highly Charged Ions (HCI), Sept. 1-6, 2002, Caen, France.

Study of Th M x-ray satellites and hypersatellites excited by energetic O and Ne ions.

M. Czarnota, M. Pajek, D. Banas, D. Chmielewska, J. Rzakiewicz, Z. Sujkowski, J.-Cl. Dousse, M. Berset, O. Maunon, Y.-P. Maillard, P.-A. Raboud, J. Hozowska, M. Polasik, and K. Slabkowska.

2nd Conference on Elementary Processes in Atomic systems, Sept. 2-6, 2002, Gdansk, Poland.

Near-threshold argon KL satellite structures studied by high-resolution x-ray spectroscopy.

J.-Cl. Dousse, M. Berset, O. Maunon, Y.-P. Maillard, P.-A. Raboud, J. Hozowska, M. Polasik, J. Rzakiewicz.

Seventeenth International Conference on the Applications of Accelerators in Research & Industry (Denton, USA, Nov. 12-16, 2002), book of abstr., p. 73.

Non-refereed papers and reports

M-(SUB) Shell Ionization in Collisions of Carbon Ions with Palladium.

J. Rzakiewicz, D. Chmielewska, T. Ludziejewski, Z. Sujkowski, D. Castella, J.-Cl. Dousse, O. Maunon, Y.-P. Maillard, P.-A. Raboud, J. Hozowska, M. Polasik, and M. Pajek.

The Andrzej Soltan Institute for Nuclear Studies, Swierk, PL, Annual Report 2000, p43.

High-resolution study of heavy-ion-induced Thorium and Uranium L_g x-ray spectra.

D. Banas, D. Castella, D. Chmielewska, D. Corminboeuf, J.-Cl. Dousse, I. Fijal, J. Hozowska, M. Jaskola, A. Korman, T. Ludziejewski, Y.-P. Maillard, O. Maunon, M. Pajek, M. Polasik, P.-A. Raboud, J. Rzakiewicz, and Z. Sujkowski.

PSI, Scientific Report 2000, Volume 1 : Particle and Matter, ISSN 1423-7296, March 2001, p.22.

High-resolution M₅-N₇ and M₄-N₆ satellite and hypersatellite x-ray spectra of metallic thorium bombarded by 24 MeV/amu oxygen ions.

J.-Cl. Dousse, D. Banas, M. Berset, D. Chmielewska, M. Czarnota, J. Hozowska, Y.-P. Maillard, O. Maunon, T. Mukoyama, M. Pajek, M. Polasik, P.-A. Raboud, J. Rzakiewicz, and Z. Sujkowski.

PSI, Scientific Report 2001, Volume 1 : Particle and Matter, ISSN 1423-7296, March 2002, p.24.

Curriculum vitae

| | |
|---------------------------|-------------------------------|
| Nom: | Mauron |
| Prénom: | Olivier |
| Date et lieu de naissance | 24 février 1973, Monthey (VS) |
| Nationalité | Suisse |
| Lieu d'origine | Ependes (FR) |
| Etat civil | célibataire |

Formation

| | |
|------------------------|--|
| 1979-1981 | Ecole primaire à Monthey (VS) |
| 1981-1985 | Ecole primaire à Corminboeuf (FR) |
| 1985-1986 1987-1989 | Ecole secondaire au Cycle d'Orientation du Belluard à Fribourg |
| 1986-1987 | Ecole secondaire à Santa Marinella (Italie) |
| 1989-1994 | Collège St-Michel à Fribourg, maturité type C |
| 1994-1999 | Université de Fribourg, diplôme en physique expérimentale |
| 1999-2002 | Université de Fribourg, assistant/doctorant en physique |

Maturité fédérale (type C)

Diplôme en physique expérimentale

Diplôme de maître de gymnase

Remerciements

Je voudrais remercier ici toutes les personnes qui m'ont aidé dans la réalisation de ce travail de thèse.

En tout premier lieu, je tiens à remercier mes parents qui m'ont soutenu à tout moment me permettant de mener à bien mes études.

Un grand merci au Prof. Jean-Claude Dousse, directeur de cette thèse, qui par son expérience, ses compétences et son enthousiasme a su me guider activement tout au long de ce travail.

Merci à tous les anciens membres du groupe PAN et de l'actuel groupe FRAP, tout particulièrement à Yves-Patrick Maillard, Pierre-Alexandre Raboud, Joanna Hoszowska, Sébastien Baechler, et Bernadette Piccand pour l'ambiance de travail agréable et pour leur aide dans mon travail.

Je tiens également à remercier Oswald Raetzo et Roger Vonlanthen de l'atelier mécanique ainsi que les ingénieurs Michel Berset et David Corminboeuf qui ont contribué à la réalisation de ce travail en garantissant en permanence un bon fonctionnement des instruments de mesure.